©[2008]

Hao Wang

ADSORBATE-INDUCED NANOSCALE FACETING

OF RHENIUM SURFACES

by

HAO WANG

A Dissertation submitted to the

Graduate School-New Brunswick

Rutgers, The State University of New Jersey

in partial fulfillment of the requirements
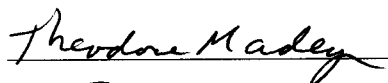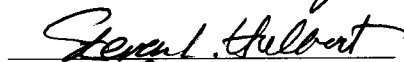
for the degree of

Doctor of Philosophy

Graduate Program in Physics & Astronomy
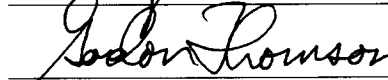
written under the direction of
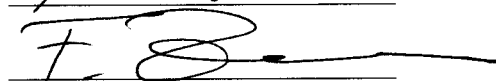
Professor Theodore E. Madey

and approved by

New Brunswick, New Jersey

October, 2008

ABSTRACT OF THE DISSERTATION

ADSORBATE-INDUCED NANOSCALE FACETING

OF RHENIUM SURFACES

By HAO WANG

Dissertation Director:

Professor Theodore E. Madey

In this dissertation, we report the first systematic study of adsorbate-induced faceting of hexagonal close-packed (hcp) metal surfaces. Focusing on two atomically rough rhenium surfaces: $Re(12\overline{3}1)$ and $Re(11\overline{2}1)$, we reveal the dependence of their surface morphology on adsorbate coverage and species by means of low energy electron diffraction (LEED), scanning tunneling microscopy (STM), Auger electron spectroscopy (AES), temperature programmed desorption (TPD) and high resolution soft X-ray photoemission spectroscopy (HRSXPS) based on synchrotron radiation.

$Re(12\overline{3}1)$ becomes completely faceted when oxygen coverage is greater than 0.7 monolayer (ML) and the surface is annealed at T > 700K. As oxygen coverage further increases, the surface morphology evolves from long ridges formed by $(01\overline{1}0)$ and $(11\overline{2}1)$ facets, to truncated ridges due to sequential emergence of $(10\overline{1}0)$ and $(01\overline{1}1)$, and eventually to complex structures formed by $(01\overline{1}0)$ $(10\overline{1}0)$ $(01\overline{1}1)$ and $(10\overline{1}1)$

ii

facets. All facets disappear when the surface is annealed at T > 1300K due to oxygen desorption and the surface reverts to planar.

Drastic differences have also been found between oxygen and nitrogen-induced faceting of $Re(11\bar{2}1)$. For $O/Re(11\bar{2}1)$, the morphology evolves as a function of oxygen coverage from a partially faceted surface with zigzag chains formed by $(01\bar{1}0)$ and $(10\bar{1}0)$ to a completely faceted surface with four-sided pyramids formed by $(01\bar{1}0)$ $(10\bar{1}0)$ $(01\bar{1}1)$ and $(10\bar{1}1)$. Two metastable facets, $(33\bar{6}4)$ and (2×1) reconstructed $(11\bar{2}2)$ are also observed in the evolution process. In contrast, for $N/Re(11\bar{2}1)$, a fully faceted surface shows ridges formed by $(13\bar{4}2)$ and $(31\bar{4}2)$ facets upon exposure to ammonia at 800-900K; ammonia dissociates on Re and only nitrogen remains on the surface at T > 600K. A (2×1) reconstructed $N/Re(11\bar{2}1)$ surface is also observed in LEED when the surface is annealed at 600-700K. Temperature-pressure phase diagrams from first principles calculations are consistent with the experimental results.

Our work has implications for Re-based catalysts that operate under oxygen or nitrogen-rich conditions because the structure of the catalysts often affects their performance. The results show great promise of tailoring the surface morphology at the nanometer scale by choosing appropriate adsorbate-substrate combinations, adsorbate coverages and annealing conditions.

Dedication

To my parents Wang Zhu-Cai and Zhan Chu-Zhi.

谨以此论文献给我敬爱的父亲和母亲：王柱才，詹楚芝。

Acknowledgements

First, I want to express my great gratitude toward Professor Theodore E. Madey, my dissertation advisor, for his tremendous support, guidance and patience during the years of my Ph. D. study at Rutgers. I am fortunate and honored to have the opportunity to study under one of the leading scientists in surface science. I cherish the time spent with him. His dedication to science will be a life-long inspiration for me.

I greatly appreciate that Professors Ronald Ransome, Gordon Thomson, Frank M. Zimmermann, Emil Yuzbashyan and Dr. Steve Hulbert agreed to serve on my dissertation committee. I am very grateful to Professor Robert A. Bartynski for reviewing my dissertation.

I am indebted to Dr. Wenhua Chen for her help and collaboration in the LEED and TPD study, Dr. Ally S. Y. Chan for the collaboration in the HRSXPS study, Dr. Timo Jacob and Payam Kaghazchi for their DFT calculations of faceting, and Dr. Qifei Wu for his friendship and for helping me familiarize with the STM instrument.

I am grateful to Dr. Boris Yakshinskiy and Dr. Alexei Ermakov for their valuable technique advice and help. I also thank my labmate, Dr. Elena Loguinova for her friendship and help. Many thanks go to other members in Ted's group: Leszek, Sergei, Nadir, Radek, Dani, Ivan, Xinyun, Robin, Govind, Meral and Robert.

I am grateful to Dr. Qing-Yi Dong and Gary Nintzel for their technical assistance in experiments performed on the U4A beamline at NSLS.

I would like to thank the LSM and Physics Department administrative staff, Kathy DiMeo, Debbie White, Grisel Ortiz-Ludovico, Nancy Pamula, Kimberly Bauer and Shirley Hinds, whose help made my study at Rutgers a pleasant experience.

I thank my fellow Chinese students in the physics department: Hua Yao, Shitao Lou and Jian Wei for their friendship.

I am greatly indebted to my parents and my wife Huiying for their love and support.

Hao Wang

Picataway, NJ

October, 2008

Table of Contents

List of figures

Lists of tables

List of acronyms and abbreviations

AES   Auger electron spectroscopy or Auger electron spectrum

bcc   body-centered cubic

DFT   density functional theory

ECS   equilibrium crystal shape

Ee   incident electron energy

fcc   face-centered cubic

hcp   hexagonal close-packed

HRSXPS high resolution soft X-ray photoelectron spectroscopy (or spectrum)

L   Langmuir ($1L=1\times10^{-6}$Torr·s$=1.33\times10^{-4}$Pa·s)

LEED   low energy electron diffraction

ML   monolayer

NSLS   National Synchrotron Light Source

QMS   quadrupole mass spectrometer

SEM   scanning electron microscopy or scanning electron microscope

STM   scanning tunneling microscopy or scanning tunneling microscope

TPD   temperature programmed desorption

UHV   ultrahigh vacuum

γ specific surface free energy

Chapter 1   Introduction

1.1 Motivation

One of the central goals for surface science studies is to understand the microscopic mechanism of heterogeneous catalysis where the catalyst is in a different phase to the reactants. In such a catalytic process, one or more of the reactants (usually in liquid or gaseous phases) adsorb onto the surface of the catalyst (usually in a solid phase), and the reaction occurs on the surface. After the reaction, the products desorb from the surface and diffuse away. A classic example of heterogeneous catalysis is the synthesis of ammonia through the Haber-Bosch process, in which N_2 reacts with H_2 on iron surfaces to form NH_3. To model heterogeneous catalysis, the approach taken by surface scientists is to study chemical reactions on simple single crystalline surfaces that act as model catalysts. This approach has lead to fundamental understanding of some important catalytic reactions such as ammonia synthesis and CO oxidation. Gerhard Ertl, a pioneering surface scientist, was awarded the 2007 Nobel prized in chemistry for his contribution in this research field.

However, a real catalyst is much more complex than just a single crystalline surface. To increase the reactive surface area, an industrial catalyst is usually in the form of small particles (1-100nm) dispersed over another support material, which is often an oxide such as silica or alumina (see Fig. 1.1 for an example [1]). The activity of the catalyst is affected by the shape, size and chemical composition of the particles as well as interactions between the particles and the support material. There is also strong evidence that the geometrical and electronic structure of the particles play a major role the selectivity of products [2, 3]. The complexity of real catalysts may be the reason that

except for few cases [4, 5] designing new catalysts is not based solely on surface science studies but on a trial and error method.
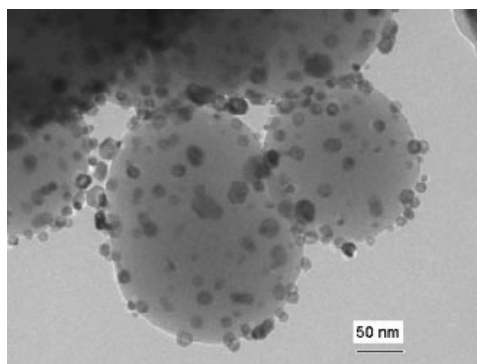
Fig. 1.1. SEM image of a 5 wt % Pd/SiO2 model catalyst after oxidation and reduction. Adapted from Ref. [1].

To help bridge this material gap between a simple single crystalline surface and a real catalyst, one approach is to add complexity to the surface in a controlled fashion by utilizing a nanoscale self-assembly process called faceting. Figure 1.2 shows a schematic of the faceting process. The initial planar surface is atomically rough with relatively high specific surface free energy. Upon adsorption of gases or metal monolayers (ML) followed by annealing, the planar surface becomes morphologically unstable and forms hill-and-valley structures at the nanometer scale with well defined facets. The facets are often more close-packed than the planar surface, thus have lower specific surface free energies. The overall surface free energy of the faceted surface is reduced although the total surface area may increase.

Faceted surfaces provide excellent model systems to study structure sensitivity in heterogeneous catalysis [6-8]. The facets with different crystalline structures can better model the complex surface structures of catalytic particles; the average size of the facets is typically at the nanometer scale, correlating well with the average size of the catalytic

Clean planar surface   Adsorbate-covered planar surface   A faceted surface
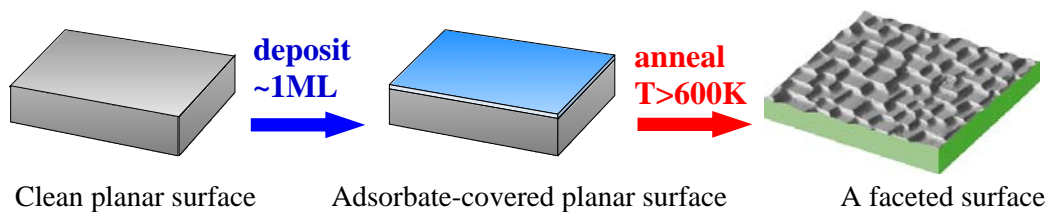
Figure 1.2. A schematic of the faceting process on a planar surface. Adapted from Ref [8].

particles. The narrow size distribution of the facets and the tunability of the average facet size can also be exploited to study size effects in catalytic reactions. Although the morphology of a faceted surface is more complex than a planar surface, the structure of each facet is still relatively simple and can be well characterized by surface science techniques. This controlled complexity makes complementary theoretical studies possible, which in turn may help gain insights into the experimental findings.

Faceted surfaces can also be used as support materials and templates to grow metal clusters for model studies of supported catalysts. The facets can guide nucleation of catalyst particles at specific surface sites of the support material with a narrow size distribution. The regular spacings between these nucleation sites can also help prevent sintering of the catalyst particles, which is a problem often observed in direct deposition of metal particles on planar surfaces.

Previous studies of faceting of atomically rough metal surfaces mainly focused on body-centered cubic (bcc) or face-centered cubic (fcc) surfaces; examples include W(111) [6, 9, 10], Mo(111) [10-12], Ni(210), Fe(111) [13] and Ir(210) [14-16]. A large uncharted area of surface faceting is hexagonal close-packed (hcp) metal surfaces although they are intrinsically more complicated than bcc or fcc surfaces due to the fact that each unit cell in a hcp metal contains two instead of one atom [17]. This dissertation is the first systematic study to understand the faceting phenomenon on hcp metal surfaces. The

reasons of choosing rhenium (Re) surfaces are two-fold: 1) Re is a hcp metal; 2) Re is a component of many catalysts [18-21]; the study of Re faceting can be of relevance to Re-based catalytic reactions.

1.2 General aspects of faceting

Faceting is believed to be driven by thermodynamics due to the fact that the surface free energy of a crystal is anisotropic, depending on the crystallographic orientation of the surface. The shape of a crystal at energy minimum, the so-called equilibrium crystal shape (ECS), can be determined by the Wulff construction method. Figure 1.3 shows a schematic polar plot of the specific surface free energy γ of an arbitrary material as a function of surface orientation; surfaces with small energies

——— Polar plot of surface free energy
--- Samples of planes normal to radius vectors of this plot
— — Equilibrium polyhedron
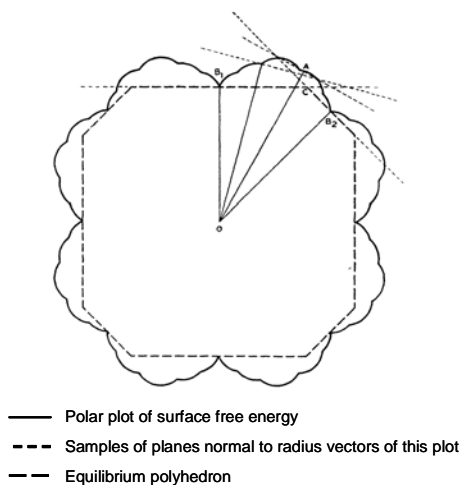
Fig.1.3. Typical polar plot of surface free energy for a crystal and the Wulff construction based on it. Adapted from Ref. [26].

correspond to cusps in the plot. The Wulff construction states that the ECS of the material is given by the smallest enclosed volume of the planes drawn at each point of the γ plot and perpendicular to the corresponding polar direction; the surfaces that appear in the ECS all have small γ.

The ECS of a crystal can be realized experimentally for small crystallites for their small kinetic limitations involved in the process [22-25]. Herring expands the ECS concept into extended surfaces and proves that a surface that is stable against faceting must be present in the ECS [26, 27]. If faceting occurs on a surface with specific surface free energy γ_0 and surface area A_0, the total surface free energy of the faceted surface must be smaller than that of the original planar surface, i.e.

$$\sum_i \gamma_i A_i < \gamma_0 A_0 , \tag{1.1}$$

where γ_i and A_i are the specific surface free energy and surface area of the ith facet, respectively.

If we denote the tilt angle between the ith facet and the planar surface as θ_i, and the projected area of the ith facet on the planar surface as A_i^p, Eq. (1.1) can be rewritten

as
$$\sum_i \frac{\gamma_i}{\cos\theta_i} \lambda_i < \gamma_0 , \tag{1.2}$$

Where $\lambda_i = \dfrac{A_i^p}{A_0}$ is the partial contribution of the ith facet to the total projected surface

area; $\sum_i \lambda_i = 1$.

Obviously in Eq. (1.2), the energy contributions of edges and corners are neglected since the average facet size observed experimentally is often in the order of ~100Å or higher.

For clean metal surfaces, because the anisotropy of γ is often too small to fulfill Eq. (1.2), some atomically rough surfaces, such as W(111), Ir(210), Re($11\overline{2}1$) and Re($12\overline{3}1$) can be stable when they are clean. However, the anisotropy of γ can be greatly

enhanced when the surfaces are covered by adsorbates due to different energy release in the adsorbate-substrate bonding process occurring on different surfaces; the adsorbate may lead to reconstruction of certain surfaces that also contributes to the change of surface energy anisotropy. For this reason, adsorbate-induced faceting on a surface is more commonly observed experimentally than faceting of a clean surface.

Driven by thermodynamics, the faceting process is also affected by kinetic factors such as nucleation and diffusion. Even when favored at room temperature, faceting often occurs when the surface is heated at elevated temperatures in order to overcome kinetic barriers to diffusion and nucleation; the average facet sizes grow with increasing annealing temperature and time to minimize the edge energy. In the case of adsorbate-induced faceting, the adsorption/desorption kinetics of the adsorbates also affects the faceting process. At high temperatures, the faceted surface reverts to planar because the anisotropy of surface free energy is reduced due to its temperature dependence or/and desorption of adsorbates.

There are two geometric constraints of surface faceting: 1) the faceted surface must retain the macroscopic orientation of the original planar surface; 2) the overall symmetry of the original planar surface/substrate must be preserved by the faceted surface. For example, three-sided pyramids are both observed in faceting of W(111) and Ir(210). However, since W(111) and Ir(210) have C_{3v} and C_{1h} symmetry, respectively, the three sides of the W pyramids have {211} orientations [28] while the Ir pyramids are elongated with one (110) and two {311} facets [14]. These two constraints can simplify identification of facet orientations when the surface morphology is complicated.

1.3 Previous studies on faceting

1.3.1 Experimental studies

Most of the experimental studies on faceting are conducted under ultrahigh vacuum (UHV) conditions; the systems studied include semiconductor, metal and oxide surfaces (see a recent review [8]). The morphology, structure and formation kinetics of faceted surfaces are characterized by techniques such as low energy electron diffraction (LEED), scanning tunneling microscopy (STM), atomic force microscopy (AFM), low energy electron microscopy (LEEM) [16, 29] and scanning electron microscopy (SEM), among which LEED is especially powerful for quick identification of whether faceting occurs on a surface.[1] The electronic structures and facet size distributions are studied by synchrotron radiation based techniques such as high resolution soft X-ray photoemission spectroscopy (HRSXPS) [30-32], scanning photoelectron microscopy (SPEM) [33], grazing incidence X-ray diffraction (GIXD) and grazing incidence small angle X-ray scattering (GISAS) [34].

Due to the existence of dangling bonds, the surface energy anisotropy of clean semiconductor surfaces is often sufficient to cause certain atomically rough surfaces to form facets even without the presence of adsorbates. Through systematic studies Gai *et al*. have identified 13 and 14 major stable surfaces for Si and Ge, respectively [35, 36]; all other surfaces are unstable and form facets of one or more of the major stable surfaces upon annealing to sufficiently high temperatures. Using both statistical mechanical models and experimental techniques, Williams and Bartelt [37] investigated faceting on clean vicinal Si surfaces and found that steps play an important role in determining the

---

[1] See section 2.3 for details.

surface free energy. T. Suzuki *et al*. [38] reported faceting of GaAs($\bar{1}\,\bar{1}2$)B surface at Ga-rich condition; the surface is rough but not faceted at As-rich condition.

There is extensive literature that describes adsorbate-induced faceting of semiconductor surfaces. Examples include Au on vicinal Si(001) [39-41], Au on vicinal Si(111) [41, 42], O/Si(5 5 12) [43], Sb/Si(5 5 12) [44], Ga/Ge(113) [45], and In/Ge(001) [46].

There are relatively few reports of faceting on clean metal surfaces because the anisotropy of γ is generally small; examples include faceting of W(210) [47], Ir(110) [48] and vicinal Au(111) [49]. However, adsorbate-induced faceting of metal surfaces focusing on bcc and fcc metals is widely observed. Among all the studies of adsorbate-induced faceting, oxygen seems to be the universal agent to cause faceting. Some of the earliest studies on faceting were conducted on oxygen-covered W(111) [50-52]; more recent examples include oxygen-covered vicinal Cu surfaces [53-55], O/Mo(111) [11, 56], O/Ir(210) [14-16, 57], O/Pt(210) [58], O/Rh(210) [59, 60], O/Rh(533) [61], oxidation of Pd(553) [62], and O/NiAl(111) [33]. Other non-metallic adsorbates that can induce faceting of metal surfaces include N/Fe(111) [13], N/Cu(210) and N/Ni(210) [63, 64], Te/Pd(100) [65], and organic molecules on vicinal Cu surfaces [66-68]. Faceting of metal surfaces induced by metallic adsorbates is less reported in the literature; some recent examples include Pd/Ta(111) [69], and Ag/vicinal Cu(111) [70]. Our research group has conducted a series of studies on faceting in bimetallic systems, focusing on W(111) and Mo(111) [6, 9, 10]. These studies conclude that a single monolayer of certain metals (Au, Ir, Pd, Rh or Ru) can induce faceting of W(111) and Mo(111) upon annealing at T >700K.

The facets observed in most cases have {211} orientations; they are covered by a single monolayer of adsorbate metal without significant alloy formation.

Faceting can also occur on clean oxide surfaces. Weichel and Moller [71] reported faceting of CoO(100) toward (110) upon annealing in UHV to 1100K. Facet formation on polar (111) surfaces of MgO and NiO were also studied by electron microscopy [72, 73]. More strikingly, people have found that faceting can be induced on vicinal Al_2O_3(0001) surfaces [74, 75], Al_2O_3($10\bar{1}0$) [75-77] and vicinal MgO(100) surfaces [78] simply by annealing in air for a couple of hours, which may expand the application area of faceted surfaces since a UHV environment is not needed in the process.

1.3.2 Theoretical studies

Faceting is believed to be driven by the anisotropy of surface free energy [26, 27]. However, for a given adsorbate/substrate system, it is difficult for a theorist to predict whether faceting occurs based on thermodynamical considerations. Theoretic studies are often impeded by difficulties in computing the anisotropy of surface free energy. Nevertheless, with improved computing power from technological advances, progress has been made in theoretical studies of faceting.

Chen [79] studied adsorption of Pd, Pt and Au on W(111) and Mo(111) using the embedded atom method; his results support the idea that the surface energy anisotropy is the driving force for faceting on these two surfaces. Oleky [80] performed Monte Carlo simulations of metal-induced faceting of different bcc(111) surfaces with a simple solid-

on-solid model; the results predict a hysteresis effect on the faceting-defaceting phase transition temperature with respect to an alternating heat treatment.

First principles electronic structure calculations based on density functional theory (DFT) have also been used to gain insights into adsorbate-induced faceting phenomena. Strumpf [81] studied H-induced faceting of Al surfaces and concluded that the faceting is caused by the preferential binding of H atoms at surface tetrahedral sites. Che *et al*. [82] studied various metal overlayers on Mo(111); their results not only confirm that metal-induced faceting is driven by the anisotropy of surface free energy, but also suggest that faceting may be hindered for certain adsorbates by a formation barrier to nucleation even when it is favored thermodynamically. Recently, Jacob and coworkers have carried out extensive studies of faceting of O/Ir(210) [83], O/Re(11$\overline{2}$1) [84], and N/Re(11$\overline{2}$1) [8]; the calculated (T, P) phase diagrams agree well with the experimental results (see details in Chapters 5 and 6). Due to calculation difficulties, in all the above DFT studies, the energy contributions from edges and kinks are ignored, which limits the application of the calculation results to systems having high surface energy anisotropy but small edge and kink energies.

1.4 Applications of faceted surfaces

1.4.1 Model systems for heterogeneous catalysis

Faceted surfaces provide a great playground for studying structure sensitivity and size effects in surface reactions, which is of close relevance to heterogeneous catalysis. The following are two major advantages of using faceted surfaces as model systems for heterogeneous catalysis: 1) different surface morphologies can be obtained on one

crystalline sample, and the results from planar and faceted surfaces can be compared in situ; 2) the facets have a narrow size distribution and the average facet sizes can be easily adjusted by changing annealing temperature and time.

Extensive studies of surface reactions on planar and faceted surfaces have been carried out in our research group [7, 8]. Evidence of structure sensitivity has been seen in n-butane hydrogenolysis on Pt/W(111) [85], acetylene reactions on Pd/W(111) [86], methanol oxidation on O/Re($12\overline{3}1$) [30], CO oxidation on O/Ir(210) [87], decomposition of acetylene on Ir(210) [88] and decomposition of H_2 and NH_3 on Ir(210) [89]. As an example, Fig. 1.4 shows TPD spectra of H_2 and N_2 as decomposition products of NH_3 on clean planar and faceted Ir(210) with different facet sizes [89]. The changes of spectra profiles on different surfaces not only show structure sensitivity in decomposition of NH_3, but also demonstrate size effects for the first time in surface chemistry on an unsupported monometallic catalyst surface.
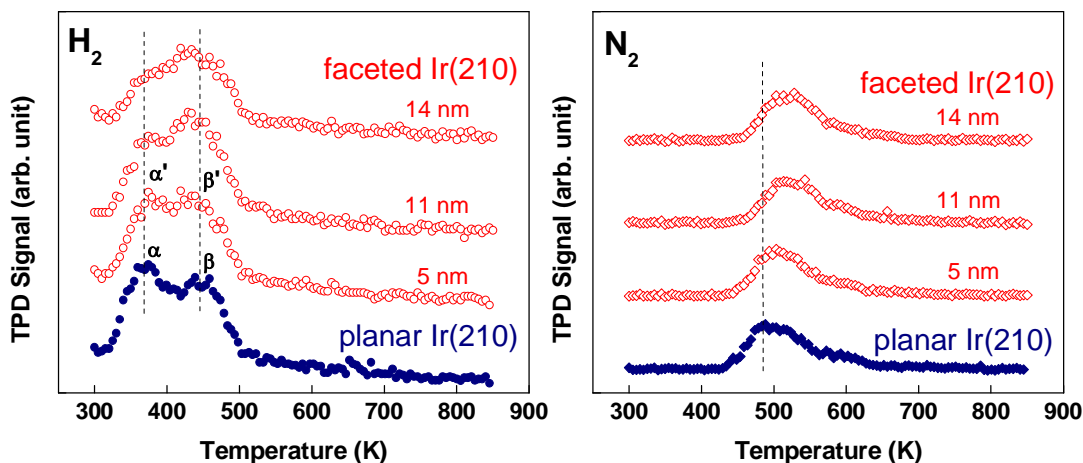
Fig. 1.4. TPD spectra of H_2 and N_2 following adsorption at 300K of 5L NH_3 on clean planar Ir(210) and clean faceted Ir(210) with different average facet sizes at 300K. The sample heating rate is ~2.5K/s. Adapted from Ref. [89]

1.4.2 Templates for nanostructure growth; nanoimprint lithography

Faceted surfaces with a narrow size distribution are attractive templates to grow nanostructures; the ordered edges and kinks on faceted surfaces provide preferential nucleation sites. Ohmori *et al*. [90] reported growth of Ge nanowires using a faceted Si(173 100 373) surface as a template. Self-organized arrays of yttria-stablized zirconia were successfully grown on a faceted vicinal Al_2O_3 (0001) surface [74]. Highly ordered Fe and Nb stripe arrays were grown by molecular beam epitaxy (MBE) techniques on a faceted Al_2O_3 (10 $\bar{1}$ 0) surface [77].

In our group, we also achieved growth of self-organized Co particles using a faceted O/Re($12\bar{3}1$) surface as a template [91]. As shown in Fig. 1.5, the faceted O/Re($12\bar{3}1$) surface shows long 2-sided ridges under certain conditions[2]; Co nano-particles nucleate preferentially inside the grooves and the average particle size correlates well with the average ridge width. This approach can be extended to grow supported catalysts with a narrow size distribution.

Gabi and coworkers [75] developed another interesting application of faceted surfaces by using a faceted Al_2O_3 (10 $\bar{1}$ 0) surface as a template to make polydimethylsioxane (PDMS) stamps. The elastomeric PDMS stamps can then be used to print ordered arrays of self-assembled alkanethiol or chlorosilane monolayers on Au-coated or bare Si wafers, respectively. Further chemical etching of the printed surfaces leads to formation of ordered Au or Si nanostructures [75].

---

[2] See Chapter 3 for details.
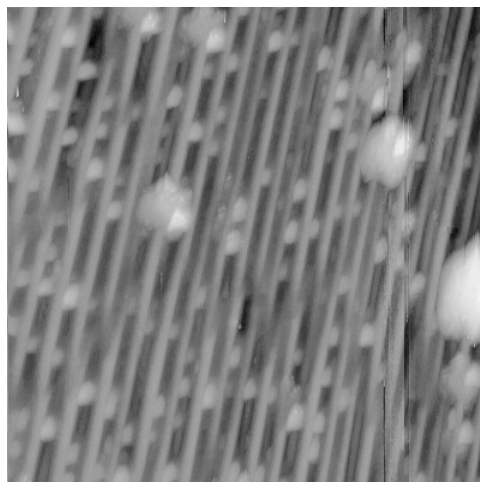
Figure 1.5. STM image (350nm × 350nm) showing 1-D arrays of Co clusters on a faceted O/Re($12\bar{3}1$) surface. The surface is prepared by depositing 2ML Co on a oxygen-saturated faceted Re($12\bar{3}1$) surface at 300K followed by annealing at 800K.

1.5 Overview of dissertation

This dissertation explores for the first time the morphological instability of atomically rough hcp metal surfaces. Focusing on two rhenium surfaces: Re($12\bar{3}1$) and Re($11\bar{2}1$), we investigate how their surface morphology can be modified in the process of adsorbate-induced faceting. The richness of the observed facet structures shows great promise that atomically rough hcp metal surfaces can be tailored to desired morphologies by choosing proper substrate/adsorbate species and annealing conditions; the faceted surfaces then provide excellent model systems for studying structure sensitivity in heterogeneous catalysis as well as templates for growth of well dispersed nanostructures.

Several complementary surface science techniques have been employed to study the structural, electronic and chemical properties of both planar and faceted surfaces. The techniques include: low energy electron diffraction (LEED), scanning tunneling microscopy (STM), Auger electron spectroscopy (AES), temperature programmed desorption (TPD) and high resolution soft X-ray photoemission spectroscopy (HRSXPS)

based on synchrotron radiation. We also collaborate with theorists to gain insights into the thermodynamical driving force of faceting process by density functional theory (DFT) calculations.

The coverage dependence of surface morphology is demonstrated in O-induced faceting of $Re(12\overline{3}1)$. Depending on oxygen coverage, a series of facet structures are observed ranging from two-sided ridges to complicated structures exposing five facets. This complexity is in sharp contrast with the simple structures reported in faceting of W(111), Mo(111) and Ir(210).

We reveal the sensitivity of surface morphology on adsorbate species by comparing the facets observed in O-induced and N-induced faceting of $Re(11\overline{2}1)$. The structural connections between the metastable facets in O-induced faceting of $Re(11\overline{2}1)$ are also investigated.

Along with the experimental findings, we have also developed methods of fast identifying facet orientations by LEED; they include: 1) using the LEED pattern from a planar surface as an in-situ reference frame to locate the positions of specular beams from facets; 2) using crystallographic zone analysis to reduce the search pool of facet candidates on the basis of the collective motion behavior of diffraction beams from two facets.

The dissertation is organized as follows: Chapter 2 contains brief descriptions of all experimental techniques used in the study; Chapter 3 deals with O-induced morphological evolution of faceted $Re(12\overline{3}1)$ surfaces; In Chapter 4, we discuss the stability of facets observed in O-induced faceting of $Re(12\overline{3}1)$, focusing on the $(11\overline{2}1)$

facet. Chapter 5 and 6 describe O-induced and N-induced faceting of Re($11\overline{2}1$),

respectively. Conclusions and future directions are given in Chapter 7.

1.6 References

[1]   A. K. Datye, Top. Catal. **13** (2000) 131.
[2]   G. A. Somorjai, *Introduction to Surface Chemistry and Catalysis*, Wiley, New York, (1994).
[3]   G. A. Somorjai and Y. G. Borodko, Catal. Lett. **76** (2001) 1.
[4]   F. Besenbacher, I. Chorkendorff, B. S. Clausen, B. Hammer, A. M. Molenbroek, J. K. Norskov and I. Stensgaard, Science **279** (1998) 1913.
[5]   J. H. Larsen and I. Chorkendorff, Surf. Sci. Rep. **35** (1999) 163.
[6]   T. E. Madey, C.-H. Nien, K. Pelhos, J. J. Kolodziej, I. M. Abdelrehim and H.-S. Tao, Surf. Sci. **438** (1999) 191.
[7]   T. E. Madey, K. Pelhos, Q. Wu, R. Barnes, I. Ermanoski, W. Chen, J. J. Kolodziej and J. E. Rowe, Proc. Natl. Acad. Sci. U.S.A. **99** (2002) 6503.
[8]   T. E. Madey, W.Chen, H. Wang, P. Kaghazchi and T. Jacob, Chem. Soc. Rev. **37** (2008) 2310.
[9]   T. E. Madey, J. Guan, C.-Z. Dong and S. M. Shivaprasad, Surf. Sci. **287/288** (1993) 826.
[10]   T. E. Madey, J. Guan, C.-H. Nien, C.-Z. Dong, H.-S. Tao and R. A. Campbell, Surf. Rev. Lett. **3** (1996) 1315.
[11]   K.-J. Song, J. C. Lin, M. Y. Lai and Y. L. Wang, Surf. Sci. **327** (1995) 17.
[12]   K.-J. Song, W.-R. Chen, V. Yeh, Y.-W. Liao, P. T. Tsao and M.-T. Lin, Surf. Sci. **478** (2001) 145.
[13]   D. R. Strongin and G. A. Somorjai, J. Catal. **118** (1989) 99.
[14]   I. Ermanoski, C. Kim, S. Kelty and T. E. Madey, Surf. Sci. **596** (2005) 89.
[15]   I. Ermanoski, K. Pelhos, W. Chen, J. S. Quinton and T. E. Madey, Surf. Sci. **549** (2004) 1.
[16]   I. Ermanoski, W. Swiech and T. E. Madey, Surf. Sci. **592** (2005) L299.
[17]   S. J. Jenkins and S. J. Pratt, Surf. Sci. Rep. **62** (2007) 373.
[18]   Y. Yuan, H. Liu, H. Imoto, T. Shido and Y. Iwasawa, J. Catal. **195** (2000) 51.
[19]   L. S. Wang, R. Ohnishi and M. Ichikawa, J. Catal. **190** (2000) 276.
[20]   F. Solymosi, P. Tolmacsov and T. S. Zakar, J. Catal. **233** (2005) 51.
[21]   K. Liu, S. C. Fung, T. C. Ho and D. S. Rumschitzki, J. Catal. **206** (2002) 188.
[22]   C. R. Henry, Surf. Sci. Rep **31** (1998) 231.
[23]   A. K. Datye and D. J. Smith, Catal. Rev. Sci. Eng. **34** (1992) 129.
[24]   T. Ohno, K. Sarukawa and M. Matsumura, New J. Chem. **26** (2002) 1167.
[25]   M. Ramamoorthy, D. Vanderbilt and R. D. King-Smith, Phys. Rev. B **49** (1994) 16721.
[26]   C. Herring, Phys. Rev. **82** (1951) 87.
[27]   C. Herring, in *Structure and Properties of Solid Surfaces*, ed. R. Gomer and C. S. Smith., University of Chicago Press, Chicago, (1953).
[28]   C.-H. Nien and T. E. Madey, Surf. Sci. **380** (1997) L527.

[29]   K. Pelhos, J. B. Hannon, G. L. Kellogg and T. E. Madey, Surf. Sci. **432** (1999) 115.

[30]   A. S. Y. Chan, W. Chen, H. Wang, J. E. Rowe and T. E. Madey, J. Phys. Chem. B **108** (2004) 14643.

[31]   M. J. Gladys, I. Ermanoski, G. Jackson, J. S. Quinton, J. E. Rowe and T. E. Madey, J. Electron Spectrosc. Relat. Phenom. **135** (2004) 105.

[32]   J. J. Kolodziej, T. E. Madey, J. W. Keister and J. E. Rowe, Phys. Rev. B **65** (2002) 75413.

[33]   E. Loginova, *Ph.D. Thesis*, Rutgers University, (2008).

[34]   C. Revenant, F. Leroy, G. Renaud, R. Lazzari, A. Létoublon and T. Madey, Surf. Sci. **601** (2007) 3431.

[35]   Z. Gai, W. S. Yang, R. G. Zhao and T. Sakurai, Phys. Rev. B **59** (1999) 15230.

[36]   Z. Gai, R. G. Zhao, W. Li, Y. Fujikawa, T. Sakurai and W. S. Yang, Phys. Rev. B **64** (2001) 125201.

[37]   E. D. Williams and N. C. Bartelt, Science **251** (1991) 393.

[38]   T. Suzuki, Y. Temko, M.C. Xu and K. Jacobi, Surf. Sci. **573** (2004) 457.

[39]   F. Zu Heringdorf, D. Kahler, M. Horn-Von Hoegen, T. Schmidt, E. Bauer, M. Copel and H. Minoda, Surf. Rev. Lett. **5** (1998).

[40]   H. Minoda, K. Yagi, F. Heringdorf, A. Meier, D. Kahler and M. von Hoegen, Phys. Rev. B **59** (1999) 2363.

[41]   K. Yagi, H. Minoda and M. Degawa, Surf. Sci. Rep **43** (2001) 45.

[42]   L. Seehofer, S. Huhs, G. Falkenberg and R. L. Johnson, Surf. Sci. **329** (1995) 157.

[43]   S. S. Lee, H. J. Song and J. W. Chung, Surf. Sci. **531** (2003) L357.

[44]   M. Kumar, Govind, V. K. Paliwal, A. G. Vedeshwar and S. M. Shivaprasad, Surf. Sci. **600** (2006) 2745.

[45]   Z. Gai, R. G. Zhao, B. Gao, H. Ji and W. S. Yang, Surf. Sci. **383** (1997) 1.

[46]   Z. Gai, H. Ji, Y. He, C. Hu, R. G. Zhao and W. S. Yang, Surf. Sci. **338** (1995) L851.

[47]   S. Kiriukhin, L. Sutcu and E. H. Conrad, Phys. Rev. B **59** (1999) 6736.

[48]   R. Koch, M. Borbonus, O. Haase and K. H. Rieder, Phys. Rev. Lett. **67** (1991) 3416.

[49]   F. Pourmir, S. Rousset, S. Gauthier, M. Sotto, J. Klein, J. Lecoeur and J. P. Bellier, Surf. Sci. **324** (1995) L337.

[50]   N. J. Taylor, Surf. Sci. **2** (1964) 544.

[51]   J. C. Tracy and J. M. Blakely, Surf. Sci. **13** (1969) 313.

[52]   H. Niehus, Surf. Sci. **87** (1979) 561.

[53]   P. J. Knight, S. M. Driver and D. P. Woodruff, Surf. Sci. **376** (1997) 374.

[54]   S. Reiter and E. Taglauer, Surf. Sci. **367** (1996) 33.

[55]   E. Taglauer, S. Reiter, A. Liegl and S. Schömann, Nucl. Instr. Meth. B **118** (1996) 456.

[56]   C. Zhang, M. A. vanHove and G. A. Somorjai, Surf. Sci. **149** (1985) 326.

[57]   I. Ermanoski, *Ph.D. Thesis*, Rutgers University, (2005).

[58]   M. Sander, R. Imbihl, R. Schuster, J. V. Barth and G. Ertl, Surf. Sci. **271** (1992) 159.

[59]   C. W. Tucker, Acta Metal. **15** (1967) 1465.

[60]   Govind, W. Chen, H. Wang and T. E. Madey, in preparation.

[61]   J. Gustafson, A. Resta, A. Mikkelsen, R. Westerström, J. N. Andersen, E. Lundgren, J. Weissenrieder, M. Schmid, P. Varga, N. Kasper, X. Torrelles, S. Ferrer, F. Mittendorfer and G. Kresse, Phys. Rev. B **74** (2006) 035401.

[62]   R. Westerström, J. Gustafson, A. Resta, A. Mikkelsen, J. N. Andersen, E. Lundgren, N. Seriani, F. Mittendorfer, M. Schmid, J. Klikovits, P. Varga, M. D. Ackermann, J. W. M. Frenken, N. Kasper and A. Stierle, Phys. Rev. B **76** (2007) 155410.

[63]   R. E. Kirby, C. S. McKee and M. W. Roberts, Surf. Sci. **55** (1976) 725.

[64]   R. E. Kirby, C. S. McKee and L. V. Renny, Surf. Sci. **97** (1980) 457.

[65]   D. Kolthoff, T. Dullweber and H. Pfnur, Surf. Sci. **447** (2000) 259.

[66]   M. Fanetti, L. Gavioli and M. Sancrotti, Adv. Mater. **18** (2006) 2863.

[67]   Q. Chen and N. V. Richardson, Prog. Surf. Sci. **73** (2003) 59.

[68]   X. Y. Zhao, H. Wang, R. G. Zhao and W. S. Yang, Mat. Sci. Eng. C-Bio. S. **16** (2001) 41.

[69]   R. Szukiewicz and J. Kolaczkiewicz, Surf. Sci. **547** (2003) L837.

[70]   A. R. Bachmann, S. Speller, A. Mugarza and J. E. Ortega, Surf. Sci. **526** (2003) L143.

[71]   S. Weichel and P. J. Moller, Surf. Sci. **399** (1998) 219.

[72]   M. Gajdardziska-Josifovska, R. Plass, M. A. Schofield, D. R. Giese and R. Sharma, J. Electron Microsc. **51** (2002) S13.

[73]   R. Plass, J. Feller and M. Gajdardziska-Josifovska, Surf. Sci. **414** (1998) 26.

[74]   R. Bachelet, S. Cottrino, G. Nahélou, V. Coudert, A. Boulle, B. Soulestin, F. Rossignol, R. Guinebretière and A. Dauger, Nanotechnology **18** (2007) 015301.

[75]   R. Gabai, A. Ismach and E. Joselevich, Adv. Mater. **19** (2007) 1325.

[76]   J. R. Heffelfinger and C. B. Carter, Surf. Sci. **389** (1997) 188.

[77]   M. Huth, K. A. Ritley, J. Oster, H. Dosch and H. Adrian, Adv. Funct. Mater. **12** (2002) 333 .

[78]   S. Benedetti, P. Torelli, P. Luches, E. Gualtieri, A. Rotaa and S. Valeri, Surf. Sci. **601** (2007) 2636.

[79]   S. P. Chen, Surf. Sci. **274** (1992) L619.

[80]   C. Oleksy, Surf. Sci. **549** (2004) 246.

[81]   R. Stumpf, Phys. Rev. Lett. **78** (1997) 4454.

[82]   J. G. Che, C. T. Chan, C. H. Kuo and T. C. Leung, Phys. Rev. Lett. **79** (1997) 4230 .

[83]   P. Kaghazchi, I. Ermanoski, W. Chen, T. E. Madey and T. Jacob, ACS Nano **2** (2008) 1280.

[84]   P. Kaghazchi, T. Jacob, H. Wang, W.Chen and T. E. Madey, in preparation.

[85]   R. A. Campbell, J. Guan and T. E. Madey, Catal. Lett. **27** (1994) 273.

[86]   R. Barnes, I. M. Abdelrehim and T. E. Madey, Top. Catal. **14** (2001) 53.

[87]   W. Chen, I. Ermanoski, T. Jacob and T. E. Madey, Langmuir **22** (2006) 3166.

[88]   W. Chen, I. Ermanoski, Q. Wu, T. E. Madey, H. H. Hwu and J. G. Chen, J. Phys. Chem. B **107** (2003) 5231.

[89]   W. Chen, I. Ermanoski and T. E. Madey, J. Am. Chem. Soc. **127** (2005) 5014.

[90]   K. Ohmori, Y. L. Foo, S. Hong, J. G. Wen, J. E. Greene and I. Petrov, Nano Lett. **5** (2005) 369 .

[91]   M. Reyhan, H. Wang and T. E. Madey, Catal. Lett. in press.

Chapter 2   Experimental facilities

2.1 Ultrahigh vacuum (UHV) environment

The experiments are conducted in ultrahigh vacuum (UHV) chambers made of stainless steel with background pressures less than 1×10^{-10} Torr; this UHV environment is essential to ensure the cleanliness of a surface in the time period of experiments. For simplicity, let us assume the background gas with pressure p and temperature T contains only one molecule species and obeys the ideal gas law, the number of gas molecules hitting on a unit surface area per second, according to the kinetic theory [1], is

$$n = \frac{p}{\sqrt{2\pi m k_B T}},$$ (2.1)

where k_B is the Boltzmann constant, and m is the mass of the gas molecule.

For $p = 1 \times 10^{-6}$ Torr and $T = 300$K, n is in the range of 0.3-1.4 $\times 10^{15}$ cm^{-2}·s^{-1} for the most common background gas molecules in a UHV chamber such as H_2, H_2O, CO and CO_2 [1]. Since the atomic density for a clean surface is about 1×10^{15} cm^{-2}, the whole surface (typical sample area ~1cm^2) will be covered by 1 monolayer of gas molecules in less than 30 seconds even with a underestimated sticking coefficient about 0.1. Therefore, to get a reasonable time period for various experimental measurements with a clean surface, a UHV environment is a must.

A UHV environment is achieved by multistage pumps working in series and/or parallel; the pumps include mechanical pumps, turbomolecular pumps, ion pumps and titanium sublimation pumps. The base pressure of a chamber is determined by the balance between the pumping speed and the outgassing rate of the materials in the chamber. One major source of the outgassing is the slow desorption of water and/or

hydrocarbon molecules adsorbed on the inner walls of the chamber [1]. To accelerate this desorption process so that a UHV environment can be achieved in a short time period, the chamber is usually baked at ~150°C for 24-48 hours during pumping. As an example, one of the UHV chambers used in the study is shown in Fig. 2.1 with the instruments labeled.
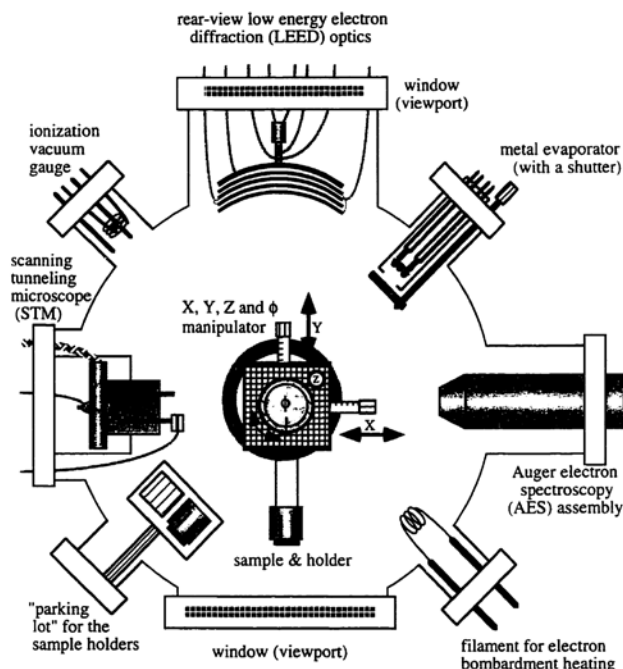
Fig. 2.1. A schematic top view of a UHV chamber used in the study (adapted from Ref. [2]).

2.2 Auger electron spectroscopy (AES)

Auger electron spectroscopy is a common technique to analyze the chemical composition of a surface by detecting electrons emitted from the surface in a so called Auger process. As shown in Fig. 2.2(a), the Auger process involves electron transitions in an excited atom with a core hole in an energy level A. The core hole can be generated by photons or high energy electrons (3-5keV) as used in a typical AES instrument. Since the

atom is in an excited state, an electron in a higher energy level B may fall into the
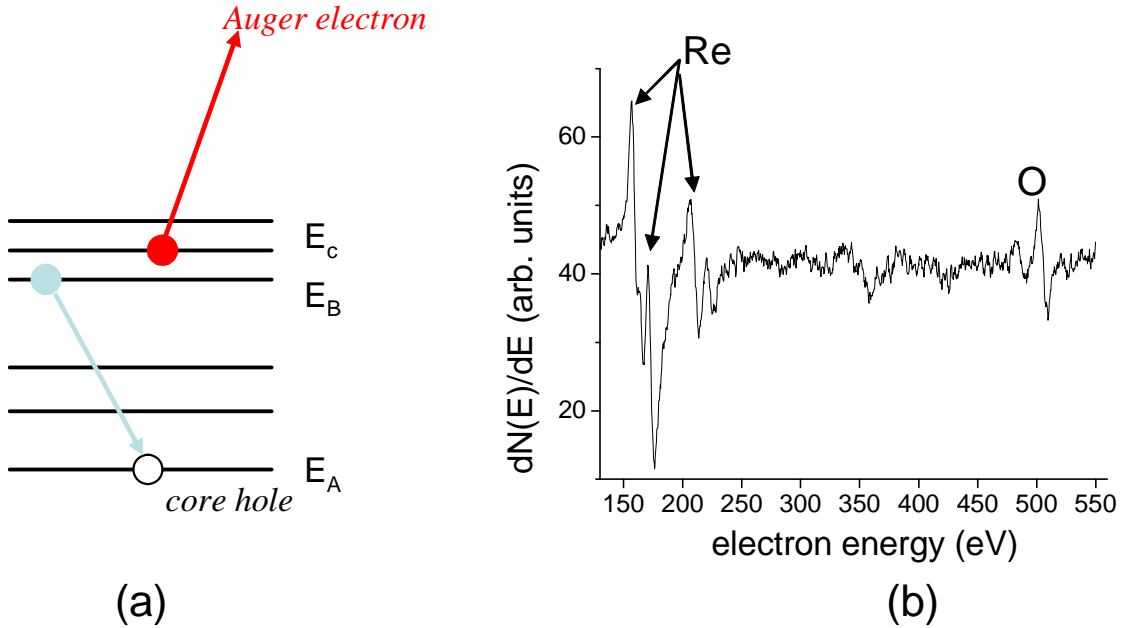
Fig. 2.2. (a) A schematic Auger process; (b) A typical Auger spectrum taken after dosing 0.3L O2 on a Re($12\overline{3}1$) surface.

energy level A to fill the core hole; the energy released from this transition may excite

another electron in another energy level C to escape into vacuum and to be detected. If

we ignore relaxation or final state effects, the kinetic energy of the emitted electron E_{KE} is

$$E_{KE} = E_A - E_B - E_C, \qquad\qquad\qquad (2.2)$$

where E_A, E_B and E_c are binding energies of an electron in energy levels A, B, and C,

respectively. Since the values of E_A, E_B and E_c are elementally sensitive, analyzing the

energy spectrum of the Auger electrons provides chemical identification of the atoms on

the surface; the surface sensitivity of AES comes from the fact that most of the AES

electrons have a mean free path of 5-10 Å [3]. An Auger spectrum is often presented in

the form of differentiated electron signal $dN(E)/dE$ as a function of electron energy E

because the Auger electrons only generate small peaks on a strong background due to

other back-scattered electrons. As an example, Fig. 2.2(b) shows a typical Auger

spectrum taken from an oxygen covered $Re(12\overline{3}1)$ surface, in which both Re and O

peaks can be identified by comparing with archived standard spectra. In the current study,

AES is mainly used for two purposes: 1) to check the cleanliness of a surface before any

further experimental procedure is performed; 2) to monitor the coverage of an adsorbate

by monitoring its Auger signal intensity.

2.3 Low energy electron diffraction (LEED)

LEED is a widely used technique to study surface structures based on the wav-

particle duality of electrons. For an electron with energy E_e, its de Broglie wavelength λ

can be written as

$$\lambda = \frac{h}{\sqrt{2m_e E_e}} = \frac{12.3}{\sqrt{E_e(eV)}} (\text{Å}) , \qquad (2.3)$$

where h is the Planck constant and m_e is the electron mass. According to Eq. (2.3), for E_e

between 20-200 eV, λ is between 2.8-0.9 Å, comparable with the lattice constant of a

typical crystal, therefore, a diffraction pattern should be expected when an electron beam

in such an energy range hits on a crystalline surface.

Figure 2.3 shows a schematic view of a typical LEED apparatus. An electron gun

produces an energy-adjustable monochromatic electron beam incident on a single crystal

surface, usually normal to the beam direction. The elastically back-scattered electron can

then pass through several energy filtering grids and hit a fluorescent screen to generate a

pattern. The shape, symmetry and periodicity of the surface structure can be identified by

just analyzing the pattern on the basis of a simple kinematic theory considering only a

single-scattering process [4]. To determine the positions of surface atoms, the diffraction

beam intensity as a function of incident electron energy must be analyzed using a more complicated dynamical theory that involves multiple-scattering processes [4]. The surface sensitivity of LEED comes from the following reason: the mean free path of 20-200 eV electrons in a crystal is less than 10 Å [3], so the elastically back-scattered electrons that can reach the screen must come from the near surface region of the crystal. In the current study, we care more about identifications of facet orientations based on the shape, symmetry and periodicity of surface structures, so the kinematic theory is enough for this purpose. Below is a brief description of the kinematic theory for LEED [4].
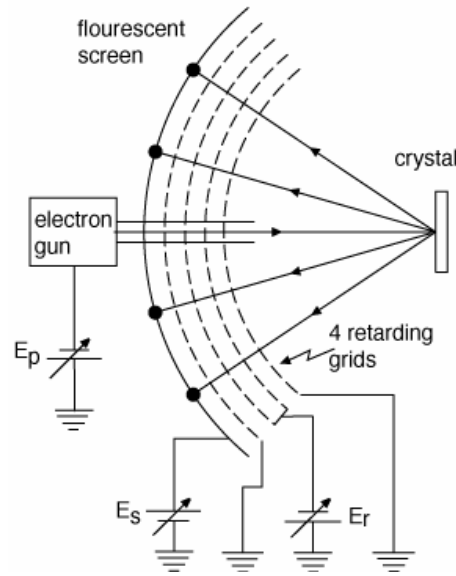
Fig. 2.3. A schematic view of a LEED apparatus.

Let us denote the unit vectors of a surface lattice as $\vec{a}_1$ and $\vec{a}_2$, and the surface normal vector as $\vec{n}$. A corresponding reciprocal space can be defined with its unit vectors $\vec{b}_1$ and $\vec{b}_2$ given below:

$$
\begin{cases}
\vec{b}_1 = 2\pi \dfrac{\vec{a}_2 \times \vec{n}}{(\vec{a}_1 \times \vec{a}_2) \cdot \vec{n}} \\[4mm]
\vec{b}_2 = 2\pi \dfrac{\vec{n} \times \vec{a}_1}{(\vec{a}_1 \times \vec{a}_2) \cdot \vec{n}}
\end{cases}
. \tag{2.4}
$$

The incident electron beam can be represented by a plane wave with a wave vector $\vec{k}_i$; similarly, the diffraction beam is also represented by a plane wave with a wave vector $\vec{k}_s$. The Bragg conditions for diffraction in 2-D require that the momentum transfer parallel to the surface $\vec{k}_{s//} - \vec{k}_{i//}$ be equal to a reciprocal lattice vector $\vec{g} = m_1 \vec{b}_1 + m_2 \vec{b}_2$, where m_1 and m_2 are integers. The elastic scattering condition requires $\left| \vec{k}_s \right| = \left| \vec{k}_i \right| = \dfrac{2\pi \sqrt{2 m_e E_e}}{h}$, which gives the constraint of the momentum transfer perpendicular to the surface. Another easy way to represent the above two conditions and to visualize the spatial relationship between the incident and the diffracted beams is through the so-called Ewald sphere construction [1].

As shown in Figure 2.4, the Ewald sphere is constructed by putting the head of the incident wave vector $\vec{k}_i$ at the origin of the Cartesian coordinate system of a 3-D reciprocal space and using the tail of $\vec{k}_i$ as the center to draw a sphere whose radius equals the length of $\vec{k}_i$. The 2-D reciprocal lattice of the surface is represented in the 3-D reciprocal space by a set of rods perpendicular to the surface; the projection of the rods on the surface retain the 2-D reciprocal lattice defined by unit vectors $\vec{b}_1$ and $\vec{b}_2$. A diffraction wave vector $\vec{k}_s$ is then determined by connecting the sphere center to any of the intersection point between a reciprocal rod and the upper hemisphere.
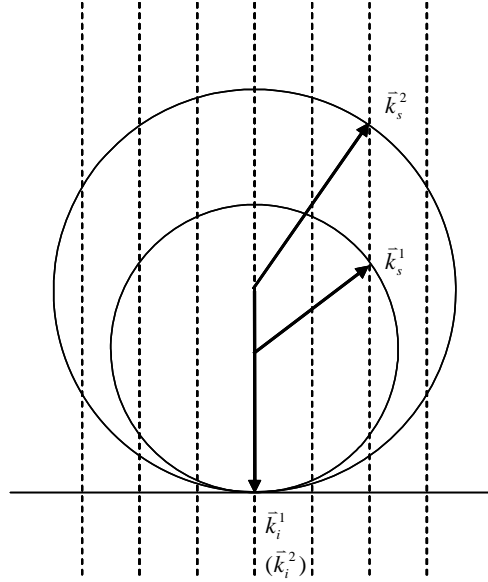
Fig. 2.4 Ewald sphere construction for two different electron energies when the incident electron beam is normal to the surface; See text for the labels.

In the current study, LEED measurements provide a simple way to quickly check whether faceting occurs on the surface, which is based on how the diffraction beams move when the incident electron energy E_e changes. The crystal sample is usually mounted in a way that the incident electron beam is normal to the macroscopic surface. For a planar surface, as the case in Fig. 2.4, the zero order diffraction beam (specular beam) would hit the center of the screen if the electron gun did not block the way. When E_e increases, the specular beam position remains in the center of the screen. However, all other diffraction beams converge to the center of the screen due to position changes of the intersection points between an enlarged Ewald sphere with the reciprocal rods (see Fig. 2.4). The situation is completely different for a faceted surface. As shown in Fig. 2.5, when the incident electron beam is not perpendicular to a facet surface, the specular beam is now away from the center of the screen. When E_e increases, the new specular beam position does not change while all other diffraction beams from the same facet converge

to this off-centered point; the total number of the off-centered specular beam positions indicates how many facets exist on the surface. Even when a specular beam lies outside of the screen, we can still identify the occurrence of faceting by monitoring the motion pattern of the diffraction beams with varying E_e.
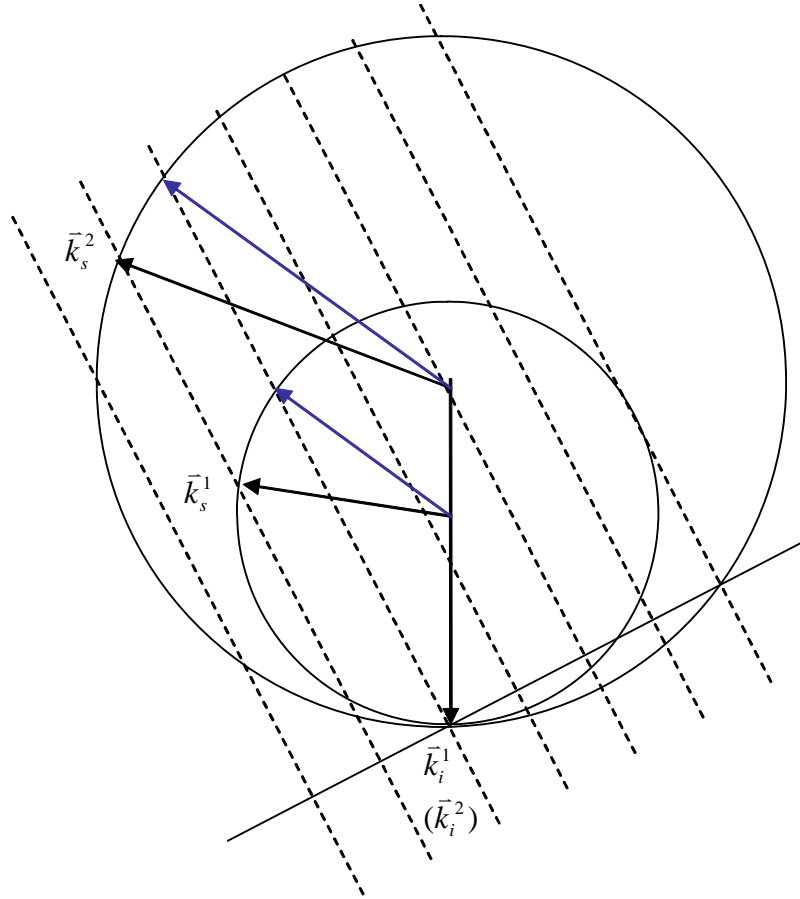
Fig. 2.5 Ewald sphere construction for two different electron energies when the incident electron beam is not normal to a facet; the blue arrows indicate the specular beam. See text for the labels.

2.4 Scanning tunneling microscopy (STM)

Scanning tunneling microscopy, a technique that can probe a surface with atomic resolution, is the first among many now widely used scanning probe microscopy techniques; its advent in the early 1980s [5-7] brings enduring impact on surface phenomena in physics, chemistry, materials science and biology [8-10]. For their

invention of the STM, G. Binnig and H. Rohrer were awarded the Nobel Prize in physics in 1986.
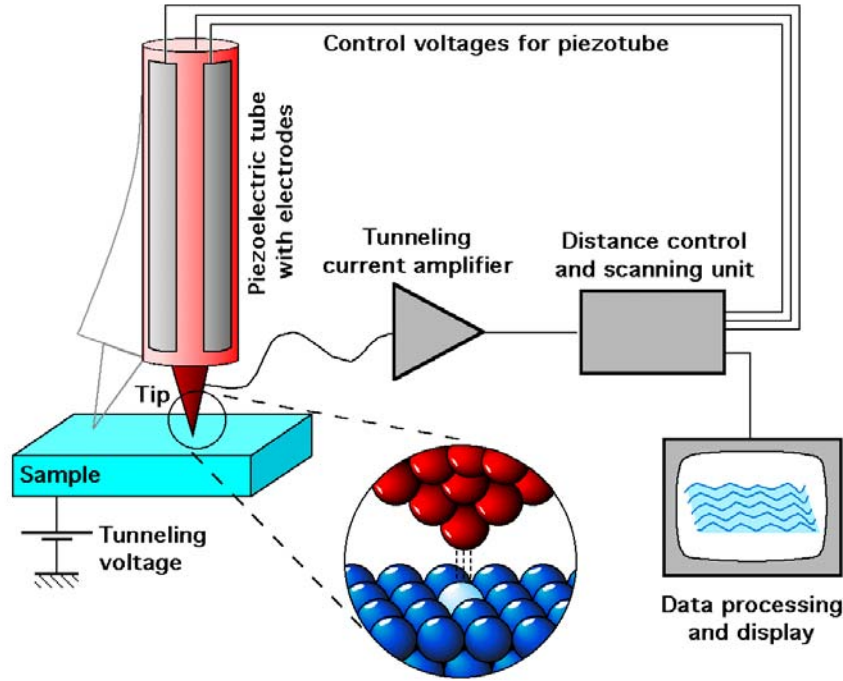
Fig. 2.6. A schematic view of a STM apparatus (adapted from Michael Schmid, TU Wien).

Figure 2.6 shows a schematic view of a typical STM design [11]. The essential part of a STM instrument is an atomically sharp W(or Pt, Ir) tip made by chemical etching or mechanical cutting. The tip is brought so close to a metal or semiconductor surface that a tunneling current can be detected once a bias voltage is applied between the tip and the surface. This tunneling current I is very sensitive to the distance between the tip and the surface. In a simple 1-D model of tunneling through a barrier without considering details of the tip and the surface [1], we have

$$I \propto \exp(\frac{-2\sqrt{2m_e\phi}}{\hbar}d) = \exp(-1.025\sqrt{\phi(eV)}d(\text{Å})), \qquad (2.5)$$

where d is the distance between the tip and the surface, $\hbar$ is the reduced Planck constant and ϕ is the average barrier height related to the work functions of the tip and the surface. For a typical value of $\phi \sim 4eV$, Eq. (2.5) shows that a change of d by 1Å will lead to an order of magnitude change of I. In Fig. 2.6, the tip is mounted on a piezoelectric ceramic tube; by applying proper voltages on the tube, it deforms to let the tip scan the surface. If a feedback loop is used in the scanning process to maintain a constant tunneling current, the moving contour of the tip records the topography of the surface. This straightforward view of a STM image as a surface topographic map is not always right especially when one tries to correlate the atomic scale features in the STM image with real atom positions on the surface; for example, the protrusions observed on a GaAs(110) surface cannot always be explained as Ga atoms for different bias voltages [12]. The detected tunneling current depends on the spatial distributions of the electronic states of both the tip and the surface. Theoretical studies show that when the tip electronic state is modeled by an s-wave, for small bias voltage the STM image can be interpreted as a contour of constant local density of states (LDOS) of the surface at the Fermi level [13, 14]. Although this widely-accepted view captures the essence that a STM image is not a simple replica of the surface topography, it does not fully explain the atomic resolution achieved experimentally. The atomic resolution requires that the tip has localized p_z or d_{z^2} states, [15] which may be realized by a single W atom migrating to the apex of the W tip under the strong electric field between the tip and the surface.

In the current study, STM is used mainly for two purposes: 1) to confirm the LEED results by providing complementary information in real space; 2) to investigate surface properties that are difficult for LEED to probe such as the size distribution of the

facets and subtle morphological evolution of faceted structures. Since the facet size is often larger than tens of angstroms, the STM image obtained does reflect the surface topography.

2.5 Other techniques

Besides the experimental techniques mentioned above, temperature programmed desorption (TPD) and high resolution soft X-ray photoemission spectroscopy (HRSXPS) based on synchrotron radiation are also used in part of the dissertation study. Below are brief descriptions of these two techniques.

A. Temperature programmed desorption (TPD)

To obtain a TPD spectrum, a surface is heated with a linear heating rate and the flux of a targeted mass species that desorbs from the surface is recorded simultaneously as a function of surface temperature by a mass spectrometer; by changing the mass spectrometer settings, a series of TPD spectra for different masses can be obtained. From the TPD spectra one can gain insights into the desorption kinetics of adsorbates, the adsorbate-surface binding energies, and surface reactions [16]. In the study of ammonia-induced faceting on Re(11$\bar{2}$1), TPD is used to identify the actual chemical species that is responsible for inducing faceting.

B. High resolution soft X-ray photoemission spectroscopy (HRSXPS) based on synchrotron radiation

X-ray photoemission spectroscopy (XPS) is a technique based on the electron photoemission process as shown schematically in Fig. 2.7. When a photon with energy $h\nu$ enters a solid, its energy can be absorbed by an electron in an energy level E_A; the then

excited electron may escape from the solid and be detected. The kinetic energy of the escaped electron E_{KE} is

$$E_{KE} = h\nu - E_A + E_r,$$ (2.6)

where E_r comes from energy release of the relaxation of other electrons to screen the core-hole generated.

photoelectron

Vacuum

incident photon

$h\nu$

E_A
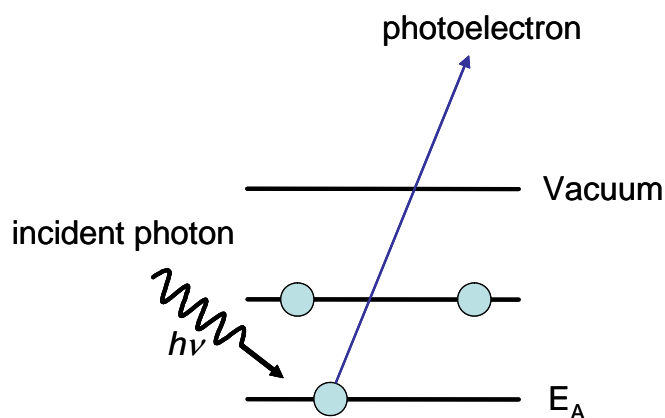
Fig. 2.7. A schematic photoemission process.

If the photon energy is high enough that even electrons at the core levels of an atom can be excited to escape from the solid, the energy spectrum of the emitted electrons can be used to identify the atom species because now E_A is elementally sensitive. Different chemical states of the atom can also be revealed in a core-level spectrum because the differences in local chemical and electronic environment affect both E_A and E_r.

Our HRSXPS study is conducted on beamline U4A of the National Synchrotron Light Source (NSLS) at Brookhaven National Laboratory. A synchrotron light source has a great advantage over a traditional X-ray source: the tunability of photon energy in a wide range. This energy tunability can be used to increase the surface sensitivity and to

improve the resolution of the spectrum. We choose the photon energy close to the threshold of photoelectron emission from a targeted core level so that the kinetic energy of emitted electrons is about 20-100eV. The surface sensitivity is increased because electrons in this energy range have a small attenuation length [3]. The high resolution comes from the fact that an electron energy analyzer can achieve better resolution at smaller electron energy. As an example, Fig. 2.8 shows typical HRSXPS spectra taken from a clean Re($12\overline{3}1$) surface.
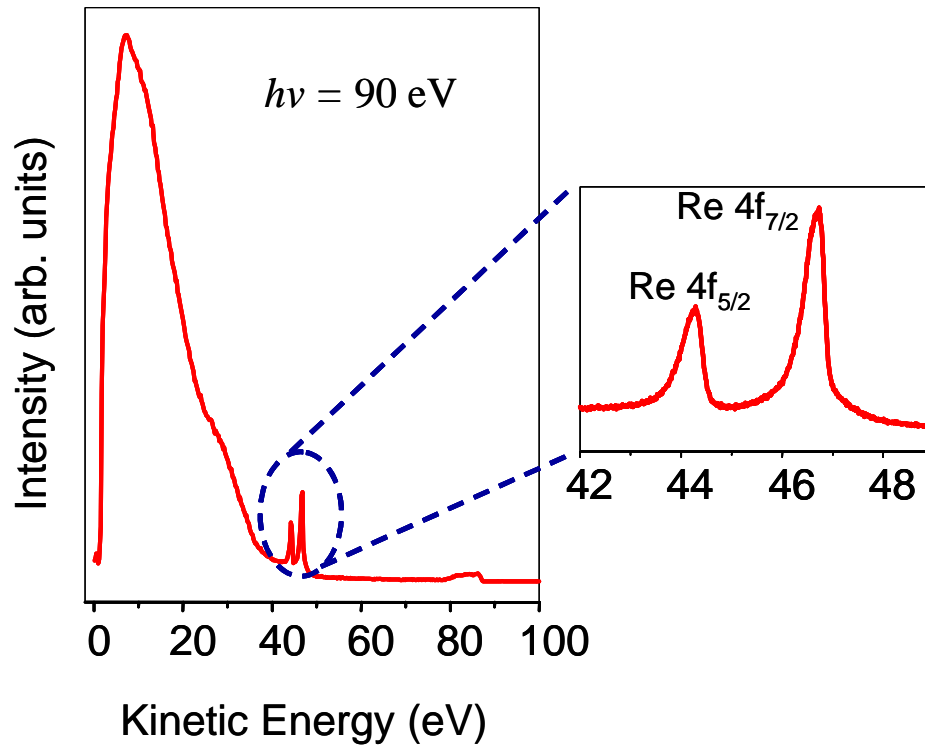
Fig. 2.8. Typical HRSXPS spectra of a clean Re surface.

2.6 Characterization of sample orientation

Two Re($12\overline{3}1$) and one Re($11\overline{2}1$) single crystals (99.99% pure) are used in the study; they are small discs, 1-2 mm thick and 8-10mm in diameter. The crystals are polished on one side and aligned within 0.5° of desired orientations. The crystallographic orientations of the Re crystals are confirmed by X-ray diffraction (Laue pattern) before

any faceting experiments. Figure 2.9(a) shows the X-ray diffraction pattern of a Re($12\bar{3}1$)

single crystal; the sharpness of the diffraction spots indicate the sample is of good quality.

Since Re($12\bar{3}1$) only has C_1 symmetry, no rotational axis or reflection plane is present in

the diffraction pattern. The simulated diffraction pattern based on the ideal crystalline

structure of Re($12\bar{3}1$) is shown in Fig. 2.9(b); the resemblance between Fig. 2.9(a) and

(a)   (b)
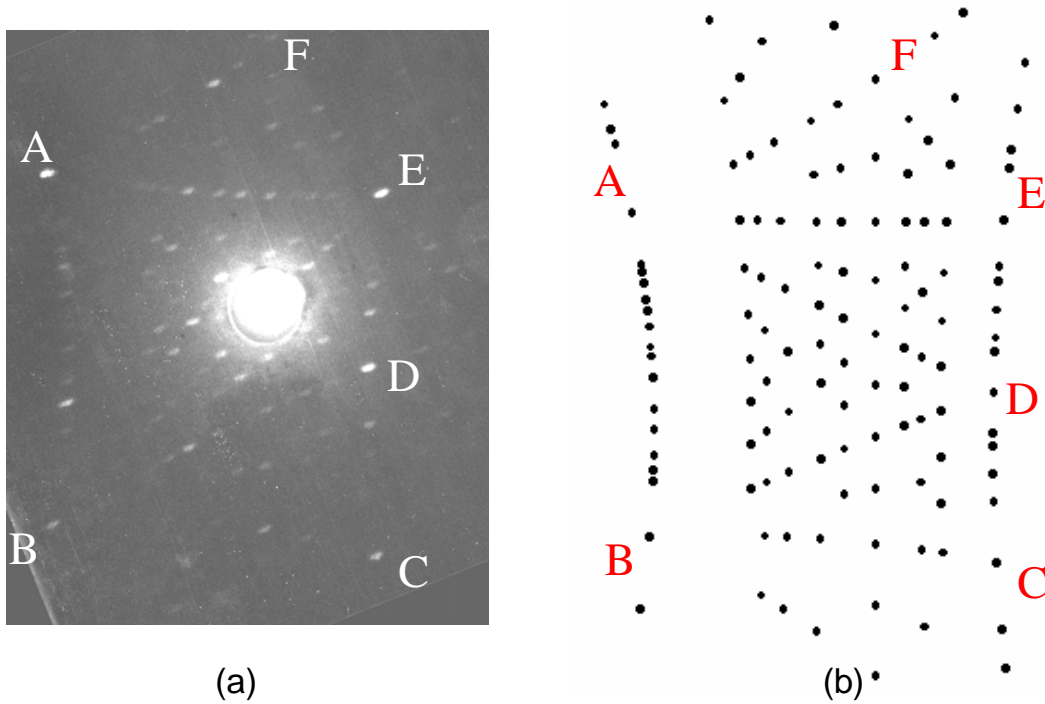
Fig. 2.9. Experimental X-ray diffraction pattern (a) and simulated pattern (b) of Re($12\bar{3}1$). Points labeled as A-E in (a) and (b) are for comparison of the two patterns.

(b) confirms that the crystal indeed has a ($12\bar{3}1$) orientation. A similar check is

performed on a Re($11\bar{2}1$) single crystal, and the experimental diffraction pattern and the

simulated pattern are shown in Fig. 2.10(a) and (b), respectively. For Re($11\bar{2}1$), its

Bravais lattice has a mirror symmetry, so a reflection mirror plane can be identified in

both Fig. 2.10(a) and (b).

(a)   (b)
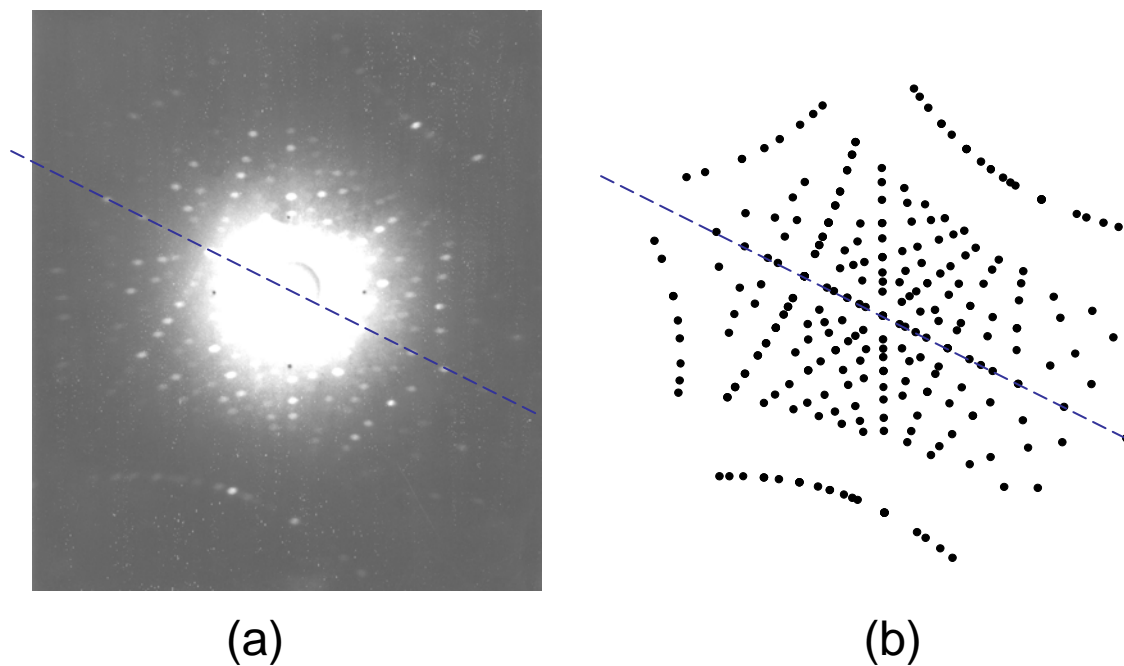
Fig. 2.10. Experimental X-ray diffraction pattern (a) and simulated pattern (b) of Re(11$\bar{2}$1). Dashed lines in (a) and (b) represent the mirror plane of reflection.

2.7 References

[1]   D. P. Woodruff and T. A. Delchar, *Modern Techniques of Surface Science*, 2nd ed., Cambridge University Press, Cambridge, (1994).
[2]   C.-H. Nien, *Ph. D. Thesis*, Rutgers University, (1999).
[3]   M. P. Seah and W. A. Dench, Surf. and Interface Anal. **1** (1979) 2.
[4]   M. A. Van Hove, W. H. Weinberg and C.-M. Chan, *Low-energy electron diffraction: experiment, theory and surface structure determination*, Springer-Verlag, Berlin; New York, (1986).
[5]   G. Binnig, H. Rohrer, C. Gerber and E. Weibel, Appl. Phys. Lett. **40** (1982) 178.
[6]   G. Binnig, H. Rohrer, C. Gerber and E. Weibel, Phys. Rev. Lett. **49** (1982) 57.
[7]   G. Binnig, H. Rohrer, C. Gerber and E. Weibel, Physica B+C **109/110B** (1982) 2075.
[8]   R. Wiesendanger and H.-J. Güntherodt, *Scanning Tunneling Microscopy I: General Principles and Applications to Clean and Adsorbate-Covered Surfaces*, 2nd ed., Springer-Verlag, Berlin; New York, (1994).
[9]   R. Wiesendanger and H.-J. Güntherodt, *Scanning Tunneling Microscopy II : Further Applications and Related Scanning Techniques*, 2nd ed., Springer-Verlag, Berlin; New York, (1995).
[10]   R. Wiesendanger and H.-J. Güntherodt, *Scanning Tunneling Microscopy III: Theory of STM and Related Scanning Probe Methods*, Springer-Verlag, Berlin; New York, (1997).
[11]   G. Binnig and D. P. E. Smith, Rev. Sci. Instrumen. **57** (1986) 1688.
[12]   R. M. Feenstra, J. A. Stroscio, J. Tersoff and A. P. Fein, Phys. Rev. Lett. **58** (1987) 1192.
[13]   J. Tersoff and D. R. Hamann, Phys. Rev. Lett. **50** (1983) 1998.
[14]   J. Tersoff and D. R. Hamann, Phys. Rev. B **31** (1985) 805.
[15]   C. J. Chen, Phys. Rev. Lett. **65** (1990) 448.
[16]   P. A. Redhead, Vacuum **12** (1962) 203.

Chapter 3 Morphological evolution in oxygen-induced faceting of Re $(12\overline{3}1)$

3.1 Introduction

It is well known that the interactions between adsorbates and substrates can enhance the anisotropy of surface free energy. As a result, a clean surface that is originally planar, when covered by adsorbates and annealed, may undergo faceting to reduce the total surface free energy [1]. The thermodynamically-driven faceting process involves mass transport of a relatively large amount of atoms, and is affected by kinetic factors such as nucleation rate and diffusion rate. Atomically rough metal surfaces are major subjects for faceting studies because they generally have higher surface free energies than close-packed surfaces and are less stable against adsorbate-induced faceting. Previous studies on adsorbate-induced faceting of atomically rough surfaces focus on bcc metals, such as W(111), Mo(111), or fcc metals, such as Cu(210), Ir(210), Ni(210) and Pt(210) [2-9]; of all these surfaces, W(111) has been most thoroughly studied [10, 11]. So far, there are no simple rules to predict whether faceting will occur in an arbitrary adsorbate-substrate system, but oxygen is observed to cause faceting in a majority of cases. The morphological changes upon faceting often bring changes in surface electronic properties and surface reactivity. For example, evidence for structure sensitivity in butane hydrogenolysis [12] and acetylene surface chemistry [13] has been found on planar and faceted Pt/W(111) and Pd/W(111) surfaces, respectively. On faceted Ir(210) surfaces, recent studies have also revealed structure sensitivity in chemical reactions such as decomposition of acetylene and ammonia, and CO oxidation [14-16].

In this chapter we extend the scope of our faceting studies from bcc and fcc metal surfaces to a hcp metal surface, Re($12\bar{3}1$), and report considerable richness in the morphology of oxygen-induced faceting: annealing Re($12\bar{3}1$) with different oxygen coverages reveals a morphological evolution from long sawtooth ridges, to complex structures exposing four different facets. Since Re is an important component in many catalysts [17-20], the faceted Re surfaces are attractive model systems to study structure sensitivity in Re-based catalytic reactions. A preliminary study has been carried out on methanol oxidation on oxygen-covered planar and faceted Re surfaces, showing differences in the reactivity of these two surfaces [21]. The electronic properties of the planar and faceted Re surfaces were also investigated by high resolution soft X-ray photoemission spectroscopy (HRSXPS) using synchrotron radiation at NSLS and reported elsewhere [22].

The orientation ($12\bar{3}1$) is chosen for two reasons. First, Re($12\bar{3}1$) is an atomically rough surface, and is expected to have high surface free energy relative to more close-packed Re surfaces, so there is a high probability that faceting may be induced on this surface. Re has a hcp structure with unit cell parameters a=2.761Å and c=4.458Å [23]; as shown in Fig. 3.1(a), the unreconstructed Re($12\bar{3}1$) surface has six layers of atoms exposed and the top-layer atoms show a quasi-hexagonal arrangement with only C_1 symmetry. Since for a hcp lattice there are two atoms in each primitive unit cell, the second stacking sequence of Re($12\bar{3}1$) is shown in Fig. 3.1(b), which has different local arrangements for the top layer atoms but the same unit cell and periodicity. Second, as shown in the sterographic projection in Fig. 3.1(c), the ($12\bar{3}1$) surface is near to several

more close-packed surfaces that could be potential facets, such as $(11\overline{2}0)$, $(01\overline{1}0)$,

$(01\overline{1}1)$ and $(11\overline{2}2)$.

(a)

(b)

(c)
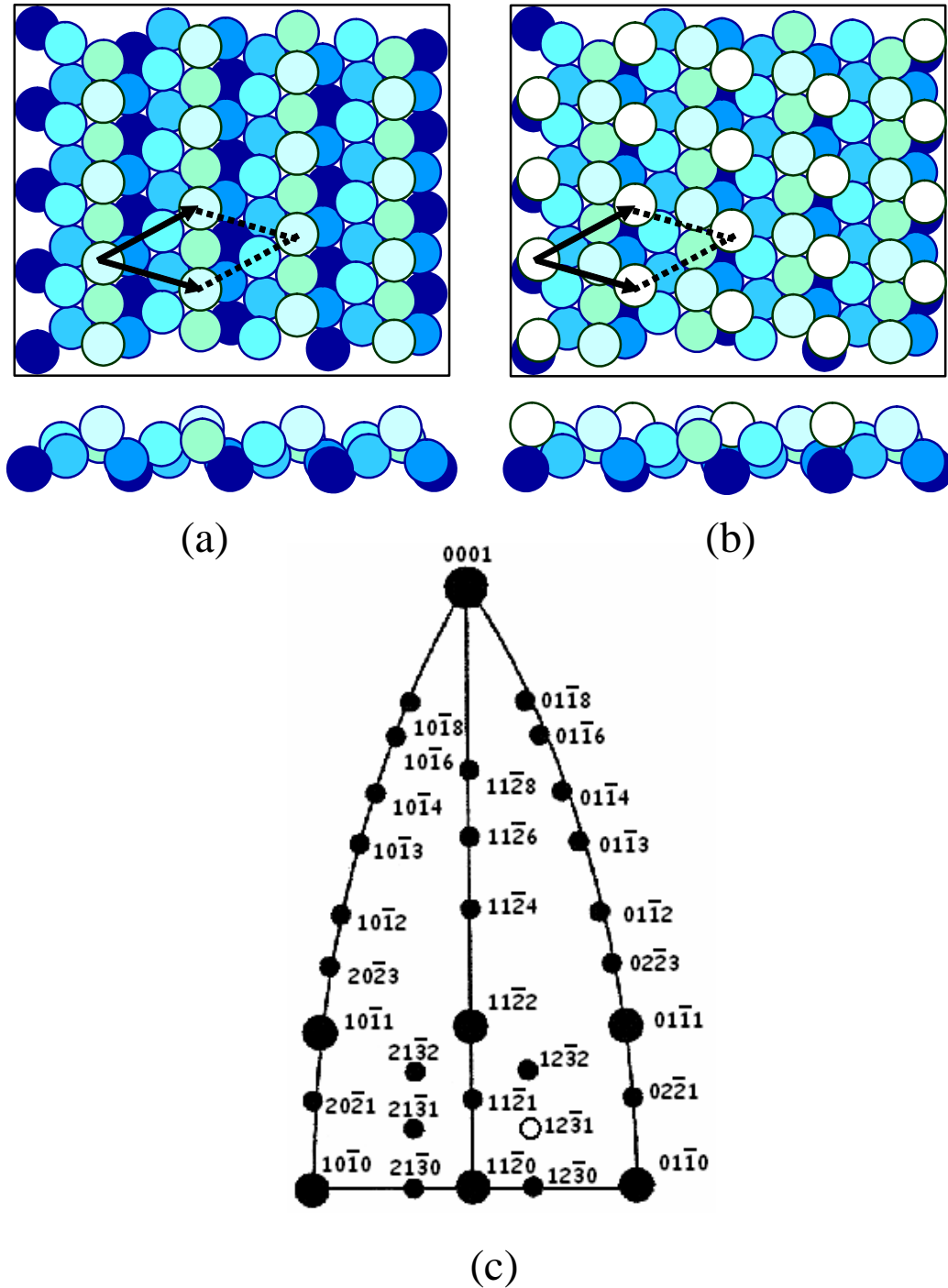
Fig. 3.1. (a) A hard-sphere model of the bulk-truncated $(12\overline{3}1)$ surface with a unit cell marked. (b) The other stacking sequence of the $(12\overline{3}1)$ surface with one more layer of atoms added on top of the surface in (a). The unit cell marked is the same as (a). (c) The stereographic projection of the hcp lattice on the plane of $(11\overline{2}0)$. The $(12\overline{3}1)$ surface is labeled by a hollow circle.

3.2 Experimental

All experiments are performed in two ultra high vacuum (UHV) chambers with base pressures about 1×10^{-10} Torr. One chamber contains AES, LEED instrumentation and a quadrupole mass spectrometer (QMS), and the other chamber contains LEED, AES, QMS and a McAllister scanning tunneling microscope. Two $Re(12\bar{3}1)$ single crystals with a purity of 99.99% are used in the study; they are ~10mm in diameter, ~1.5mm thick and aligned within 0.5° of the $(12\bar{3}1)$ orientation. The Re crystals are cleaned by cycles of e-beam heating in oxygen (1×10^{-7} Torr) followed by flashing in vacuum to above 2000K, and the cleanliness of the Re surfaces is checked by the AES in both chambers. The residual contaminant species such as carbon and oxygen are below 1-2 percent of a monolayer of atoms. Oxygen is dosed on the Re surfaces at room temperature by backfilling the chamber and pressures are measured using an uncalibrated Bayard-Alpert ionization gauge. The sample temperatures are measured either by a C-type (W-5 at.% Re/W-26 at.% Re) thermocouple spotwelded to the back of the Re crystal or by an infrared pyrometer. All STM measurements are made at room temperature with a typical sample bias between 0.5 to 1.2V and a tunneling current between 0.6 and 1nA. The X and Y dimensions of the STM scan range are calibrated using atomically resolved STM images of the S(4×4)/W(111) reconstruction [24] and the Z dimension is calibrated based on tilt angle measurements between (211) and (111) planes in faceted O/W(111) [25].

3.3 Results

3.3.1 Morphological evolution of the facets

A. AES and LEED study

The relative oxygen coverage θ is determined from measurements of the O/Re Auger peak height ratio as a function of oxygen dose at room temperature; the oxygen dose is expressed in units of Langmuir (L, $1L=1\times10^{-6}Torr\cdot s=1.33\times10^{-4}Pa\cdot s$). As shown in Fig. 3.2, the O/Re Auger ratio increases with oxygen dose and reaches saturation when the oxygen dose is between 5 and 7L, which is comparable with an early AES study of oxygen adsorption on a vicinal Re(0001) surface, where the saturation is reached after an exposure between 7 and 8L [26]. In a previous XPS study of oxygen adsorbed on
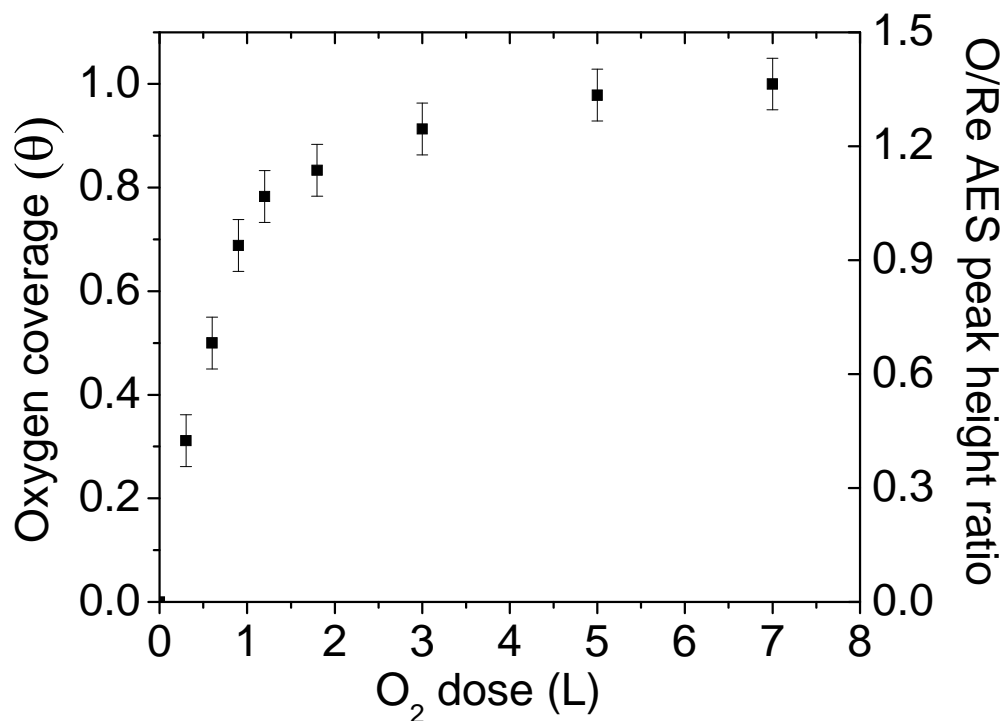
Fig. 3.2. The oxygen uptake curve on Re($12\overline{3}1$) at room temperature measured by AES. Both the O/Re Auger peak height ratio and the average O coverage (θ, in monolayers) are plotted vs. O_2 dose in Langmuirs.

polycrystalline Re surface, the saturation coverage is also found to be reached at an oxygen exposure about 5L [27]. If we define the coverage corresponding to the saturation O/Re Auger ratio as one monolayer (ML), i.e. $\theta = 1$ML, the relative oxygen coverage for a given oxygen dose can be determined by normalizing the measured O/Re Auger ratio to the saturation value. This definition of saturation coverage is used here only for low oxygen doses ($<10^2$L) because with high oxygen doses the O/Re Auger peak height ratio may exceed the above saturation value as a consequence of surface oxidation or oxygen diffusion to the subsurface.
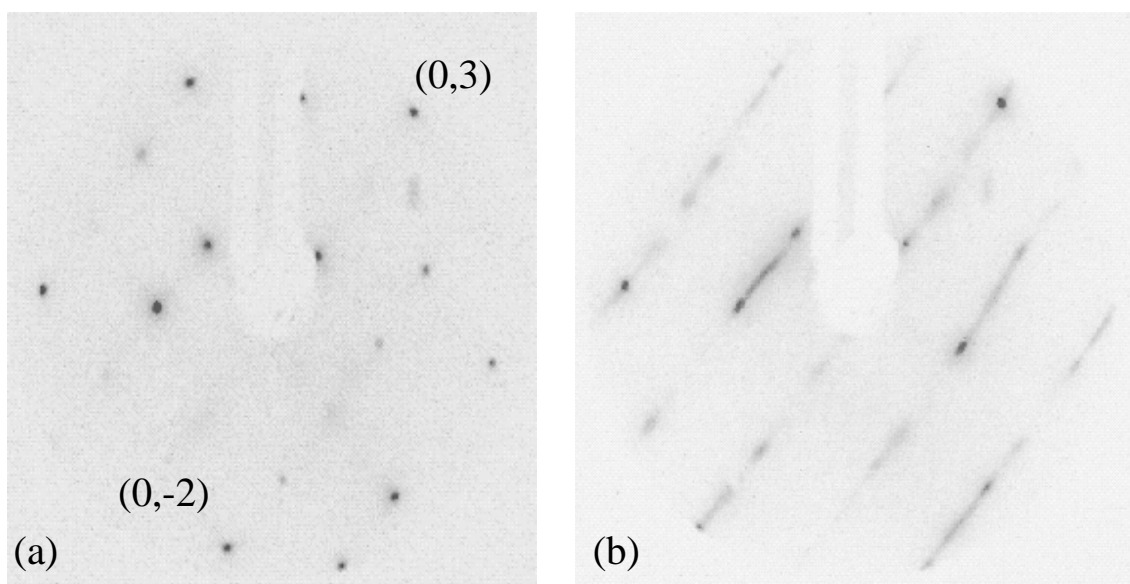
Fig. 3.3. (a) A LEED pattern from a clean surface with the (0,3) and (0,-2) diffraction spots labeled; E_e=70eV. (b) A LEED pattern from a O/Re($12\overline{3}1$) surface prepared by dosing 0.5L O_2 ($\theta = 0.5$ML) at 300K followed by annealing at 900K; E_e=70eV.

Fig. 3.3(a) shows a typical LEED pattern from a clean Re ($12\overline{3}1$) surface; all beams are characteristic of the (1×1) structure. There are no other LEED features found after annealing the surface at temperatures up to 2000K. When the incident electron energy (E_e) increases, all the diffraction spots converge to the center of the LEED screen, indicating that the surface is macroscopically planar although it is atomically rough. No new

features appear in the LEED pattern when the surface is exposed to O_2 up to 300L at room temperature except for a slight increase of the background intensity, which can be attributed to random adsorption of oxygen atoms.

Annealing the oxygen-covered surface may cause various new features in the LEED pattern depending on oxygen exposure (coverage). When the oxygen dose is less than 0.5L ($\theta < 0.5$ML), the surface remains planar and retains the (1×1) structure after annealing at temperatures up to 2000K. In contrast, when the oxygen dose is between 0.5L and 1L (0.5ML $\leq \theta < 0.7$ML), streaks along one direction emerge around the (1×1) spots after annealing at ≥700K (see Fig. 3.3(b)). These streaks do not converge to the screen center as E_e increases, indicating the formation of tiny facets that coexist with the ($12\bar{3}1$) surface. For an oxygen dose between 1L and 3L (0.7ML $\leq \theta < 0.9$ML) and after annealing at ≥700K, the (1×1) LEED spots totally disappear and the streaks in Fig. 3.3(b) evolve into sharp spots (see Fig. 3.4 (a)). Just like the streaks, these new diffraction spots do not converge to the screen center but move toward either of two fixed spots marked by two circles A and B in Fig. 3.4(a) when E_e increases. The two fixed spots are specular beams of the facets and this phenomenon can be better illustrated in a LEED pattern taken with variable E_e shown in Fig. 3.4(b), in which each short line represents the moving trace of a LEED spot as E_e is changed from 40 to 146 eV. It is clear that these lines point to the same two positions away from the center of the screen, also marked by two circles A and B, which indicates that the surface is no longer planar but completely faceted with a sawtooth ridge-like morphology.

The orientations of the two facets are determined by comparing the specular beam positions with the LEED spots from a planar Re($12\bar{3}1$) surface. When E_e is 70±5eV, the
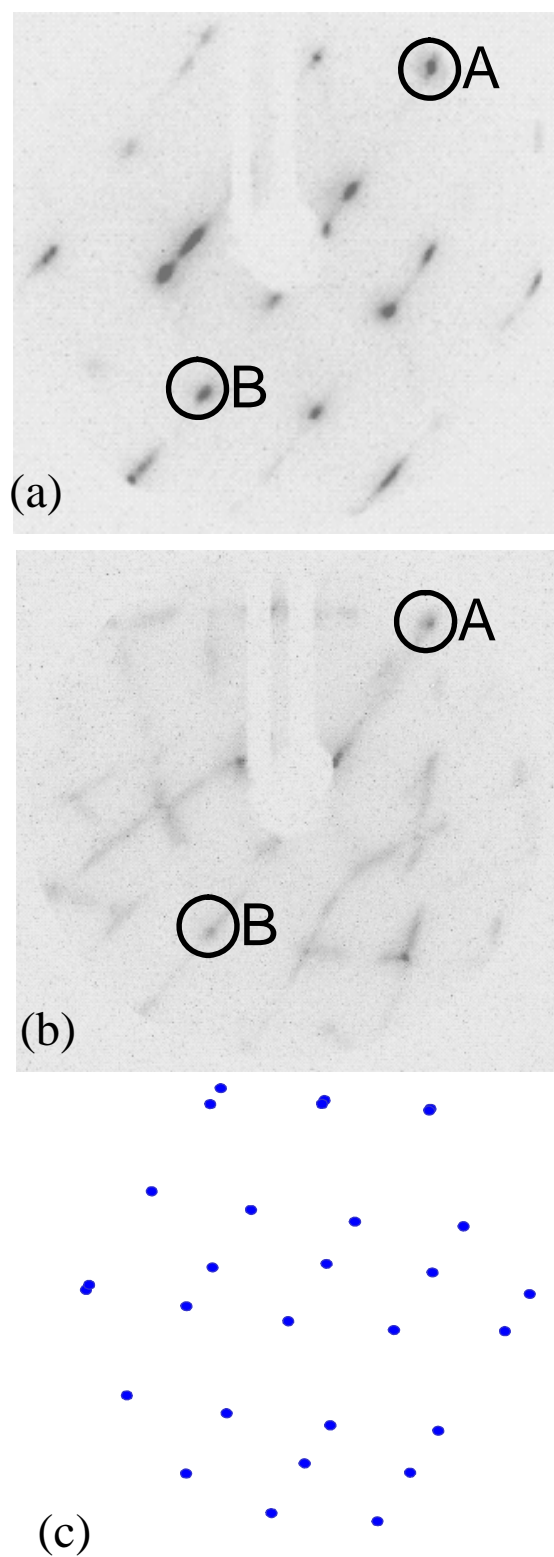
Fig. 3.4. LEED patterns of a faceted O/Re($12\overline{3}1$) surface formed by dosing 3L O_2 ($\theta = 0.9$ML) at 300K followed by annealing at 900K. (a) E_e=70eV. (b) E_e varies from 40 to 146 eV. The circles A and B indicate specular beams from the facets. (c) is the kinematical simulation of (a).

(0,3) diffraction spot from the planar Re($12\bar{3}1$) surface (see Fig. 3.3(a)) is located almost in the same position on the LEED screen as specular beam A in Fig. 3.4(a) from one of the two facets; the estimated error range of E_e is due to the uncertainty of determining a perfect match and the inner potential of the Re sample. The spatial orientations of the (0,3) beam can be determined simply from the structure of the reciprocal rods of Re($12\bar{3}1$) and the Ewald sphere construction [28], from which the tilt angle between the (0,3) beam and the normal direction of ($12\bar{3}1$) is calculated as 44±2°; therefore the tilt angle of the facet relative to ($12\bar{3}1$) is 22±1°. Similarly, a good match is found between the (0,-2) spot from the planar Re($12\bar{3}1$) and specular beam B in Fig. 3.4(a) for E_e=85±5eV, and the tilt angle between this facet and ($12\bar{3}1$) is then calculated as 12.5±0.5°. Based on these measurements, the Miller indices of the facets are identified as ($01\bar{1}0$) and ($11\bar{2}1$), and the ridge direction is identified as [$\bar{2}113$]. The tilt angles between ($01\bar{1}0$), ($11\bar{2}1$) and the substrate are 22.2° and 12.0°, respectively, agreeing well with the experimental values. Fig. 3.4(c) shows a kinematical simulation of the faceted LEED pattern in Fig. 3.4(a) for E_e=70 eV, based on the bulk-truncated structures of ($01\bar{1}0$) and ($11\bar{2}1$). The similarity between the simulation and the experimental pattern not only confirms the orientations of the facets but also suggests that there is no reconstruction on either facet, which retain their (1×1) structures.

When the oxygen dose at room temperature exceeds 3L ($\theta \geq 0.9$ML), the morphology of the faceted surface formed upon annealing becomes more complex with the emergence of new spots in LEED. Fig. 3.5(a) is a typical LEED pattern from a O/Re($12\bar{3}1$) surface prepared by dosing 10L O$_2$ ($\theta = 1$ML) followed by annealing at 1000K. In addition to all
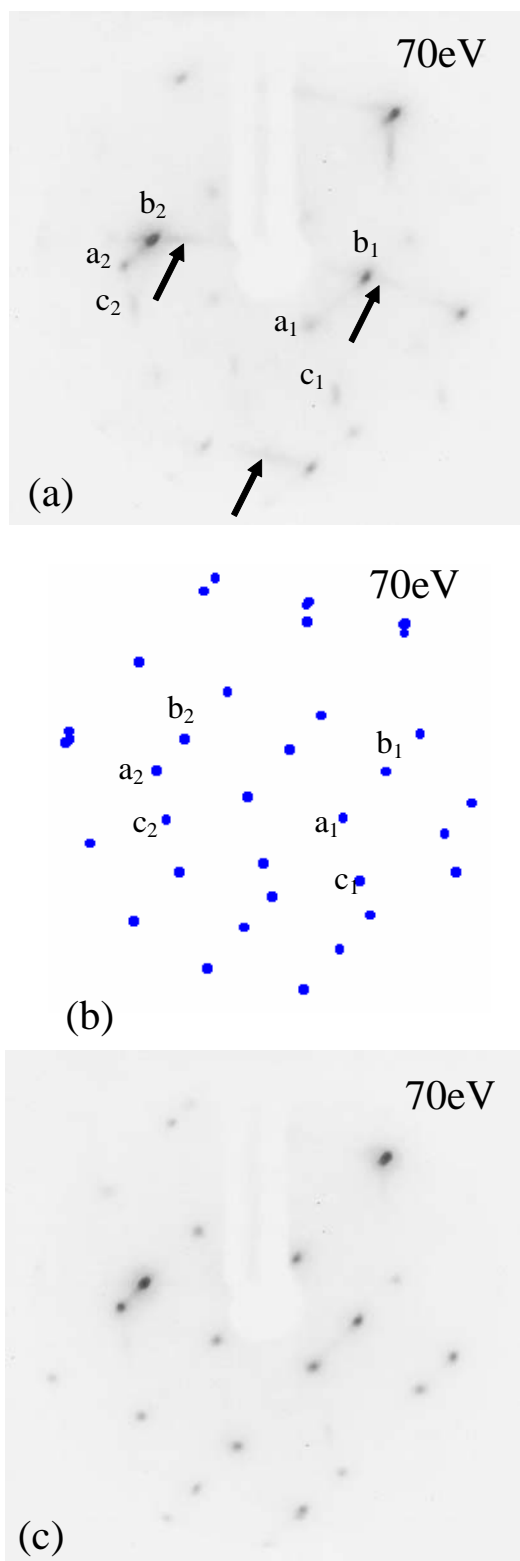
Fig. 3.5. LEED patterns of faceted O/Re($12\overline{3}1$) surfaces formed by dosing 10L O_2 ($\theta = 1$ML) at 300K followed by annealing at different temperatures. (a) 1000K, E_e=70eV. (c) 1200K, E_e=70eV. (b) is the kinematical simulation of (a). See text for the labels in (a) and (b).

the LEED spots from the original two facets, new faint spots (e.g. spots marked by c_1 and c_2 in Fig. 3.5(a)) can be seen. When E_e increases, these extra spots move toward a third direction rather than converging to either of the two original specular beam positions, indicating the formation of a third set of facets that truncate the original ridges. Since the specular beam from the third facet lies outside the LEED screen, it is difficult to determine the facet orientation directly. However, an analysis of the spatial relationship between the spots from the third facet and those from the two original facets can provide a clue. In Fig. 3.5(a), a_1 and b_1 mark representative spots from $(11\bar{2}1)$ and $(01\bar{1}0)$, respectively, and they form a quasi-isosceles triangle with spot c_1, in which the distance a_1b_1 is approximately equal to a_1c_1. When E_e changes, b_1 and c_1 move almost symmetrically relative to a_1 to retain the configuration of the quasi-isosceles triangle. The same behavior is also observed for spots a_2, b_2 and c_2, where a_2 and b_2 are from $(11\bar{2}1)$ and $(01\bar{1}0)$, respectively. These observations suggest that the third facet and the $(01\bar{1}0)$ facet are spatially symmetric relative to the $(11\bar{2}1)$ facet, which leads to $(10\bar{1}0)$ as the logical choice of the orientation of the third facet (see the stereographic projection in Fig. 3.1(c)). The small amount of symmetry-breaking in LEED is due to the fact that the incident electron beam is along the normal direction of $(12\bar{3}1)$ rather than that of $(11\bar{2}1)$ and the tilt angle between these two orientations is only 12.0°. To verify this, a kinematical simulation of the LEED pattern based on the bulk-truncated structures of $(11\bar{2}1)$, $(01\bar{1}0)$ and $(10\bar{1}0)$ is shown in Fig. 3.5(b) with spots a_1, b_1, c_1, a_2, b_2 and c_2 labeled, which agrees well with the experimental pattern in Fig. 3.5(a). The tilt angle between $(10\bar{1}0)$ and $(12\bar{3}1)$ is 42.2°, meaning the angle between the specular beam of $(10\bar{1}0)$ and the incident electron beam is 84.4°, which is greater than the half-maximum

acceptance angle of the LEED screen (60°), and is consistent with the experimental observation that the specular beam of $(10\bar{1}0)$ lies outside of the screen. The $(10\bar{1}0)$ orientation is further confirmed in the STM study discussed in next section.

Careful examination of LEED patterns like Fig. 3.5(a) reveals several faint streaks marked by three arrows. These streaks do not belong to any of the three identified facets because they converge to a fourth position lying outside of the LEED screen as E_e increases. The fact that the new features are faint and streaky implies that they originate from a fourth facet that is not well developed and has limited size in one direction. For this reason, it is difficult to identify the orientation of the fourth facet from LEED. In the following section, we show how STM measurements can help provide a solution.

It is important to point out that when the oxygen dose is between 3L and 5L ($0.9\text{ML} \leq \theta < 1\text{ML}$), the streaks marked by the arrows in Fig. 3.5(a) become less prominent. With the oxygen dose reduced to the lower limit 3L ($\theta = 0.9\text{ML}$), the streaks disappear and only diffraction spots from $(11\bar{2}1)$, $(01\bar{1}0)$, and $(10\bar{1}0)$ can be observed. Annealing the oxygen-covered surface in Fig. 3.5(a) at 1200K leads to the LEED pattern in Fig. 3.5(c). The streaks associated with the fourth facet disappear and the pattern looks like that from the ridges without truncation since the spots associated with the third facet are also weak. This morphology reversion can be attributed to desorption of oxygen at 1200K [29]. By annealing at 1600K, the coverage of oxygen remaining on the surface is not even sufficient to maintain the surface as partially faceted; the surface reverts to the planar morphology with a LEED pattern similar to Fig. 3.3(a).

B. STM study

Fig 3.6(a) shows a typical STM image from a faceted Re($12\bar{3}1$) surface prepared by dosing 1L O_2 (θ = 0.7ML) and annealing at 1000K. The eye-catching feature is that the surface is not planar but completely covered by long ridges along the [$\bar{2}113$] direction with typical length larger than 500 Å and the longest length about 1000 Å. Fig. 3.6(b) is the cross-section profile along the line marked in Fig. 3.6(a), showing the sawtooth-like character of the facet morphology, from which the tilt angles of the facets relative to ($12\bar{3}1$) can be determined by measuring the slopes of the line segments. Based on analysis of several similar cross-section lines, the tilt angles with respect to the substrate are measured as 23.5±1.9° and 12.2±1.2°, respectively, which agree well with the ideal
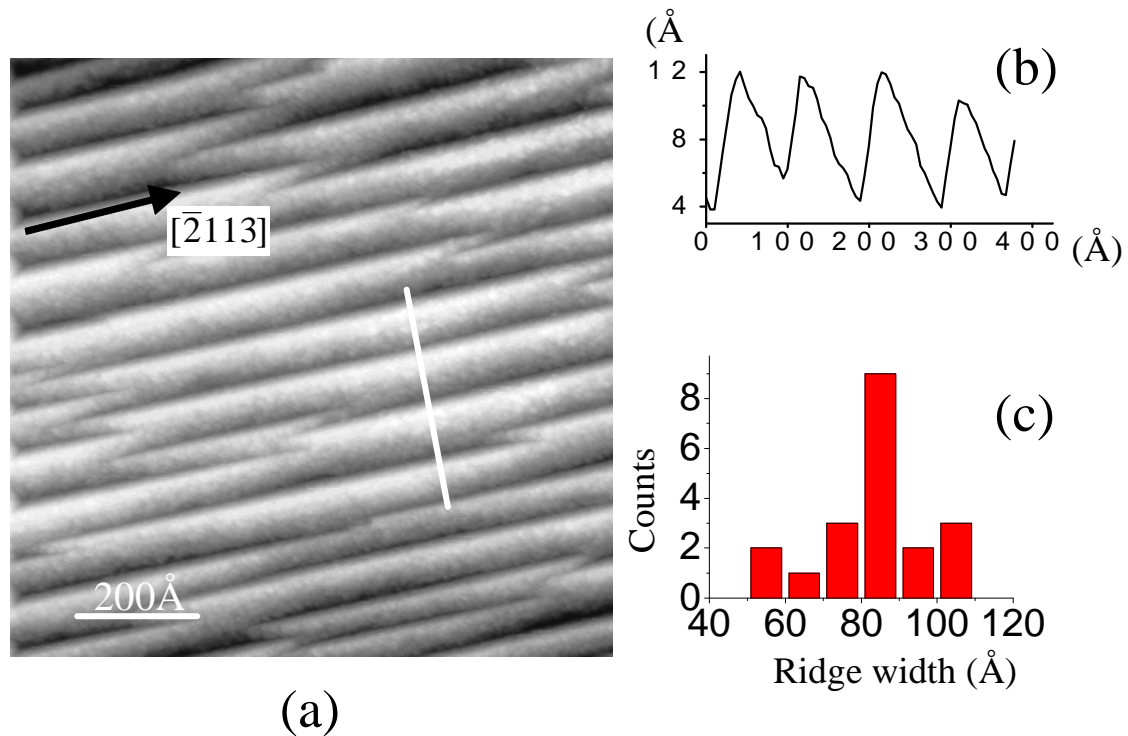
Fig. 3.6. (a) STM image of a faceted O/Re($12\bar{3}1$) surface prepared by dosing 1L O_2 (θ = 0.7ML) at 300K followed by annealing at 1000K. The dimensions are 1000Å×1000Å. (b) A cross-section profile of the line marked in (a). (c) Histogram of the ridge width distribution in (a).

values 22.2° and 12.0° of the $(01\bar{1}0)$ and $(11\bar{2}1)$ facets identified in LEED experiments. The width of the ridges is quite uniform with a mean value 82±7Å; the result of a ridge width survey is shown in Fig. 3.6(c). The ridge-like morphology on the faceted Re$(12\bar{3}1)$ surface is very different from those reported to date for other refractory metal surfaces, such as W(111), Mo(111) and Ir(210), where three sided-pyramidal facets are observed [8, 10, 30]. Nevertheless, similar faceting morphology has been reported in other systems such as faceting on Pt(210) induced by CO oxidation [9], the Ga rich GaAs($\bar{1}\bar{1}\bar{2}$)B surface [31] and faceting on vicinal Si(111) surfaces [32]. These ridge-like structures on O/Re$(12\bar{3}1)$ are stable at room temperature; no morphological change can be found over the time span of more than a week.

As manifested in the LEED study, the STM results also reveal in greater detail that the morphology of the faceted surface depends on oxygen coverage. Fig. 3.7(a) is a typical STM image taken from the O/Re$(12\bar{3}1)$ surface prepared by dosing 3L O$_2$ ($\theta =$ 0.9ML) followed by annealing at 800K, in which the ridges are all truncated by a third set of facets as indicated by LEED measurements. Because of the large undulation of height in the ridge structure and the limited resolution of the gray scale, it is difficult to see topographic details of the facets in the raw STM images. By differentiating the height along the X direction (X-slope), the details can be enhanced at the cost of losing the height information. In an X-slope STM image, regions with the same slope along the X direction are displayed with the same gray color. Fig. 3.7(b) is the X-slope image of Fig. 3.7(a); this image exhibits enhanced contrast, in which the light gray areas are $(01\bar{1}0)$ facets, the gray areas are $(11\bar{2}1)$ facets and the dark areas are attributed to the third facet $(10\bar{1}0)$. It is noteworthy that the $(11\bar{2}1)$ facets often contain bunched steps within one

Fig. 3.7. STM images of faceted O/Re($12\bar{3}1$) surfaces prepared by dosing 3L O$_2$ ($\theta = 0.9$ML) at 300K followed by annealing at 800K for 2 minutes. (a) 500Å×500Å, raw data; (b) after the X-slope taken. (c) and (d) show measured and ideal azimuthal angles of edge lines formed by facets, respectively.

ridge (examples marked by small arrows), while the ($01\bar{1}0$) facets have a much lower

step density. The existence of the steps on ($11\bar{2}1$) is essential in the sense that ridges

with one end truncated by a facet alone cannot maintain the macroscopic orientation of

the original planar ($12\bar{3}1$) substrate. If we focus on the end of one ridge shown in Fig.

3.7(c), the orientations of the facets identified by LEED can be further confirmed by

measuring the azimuthal angles between the edge lines. The measured angle values are

also shown in Fig. 3.7(c), which are in good agreement with the ideal values calculated

from the projected intersection lines between $(11\overline{2}1)$, $(01\overline{1}0)$, and $(10\overline{1}0)$ planes on the $(12\overline{3}1)$ surface (see Fig. 3.7(d)).
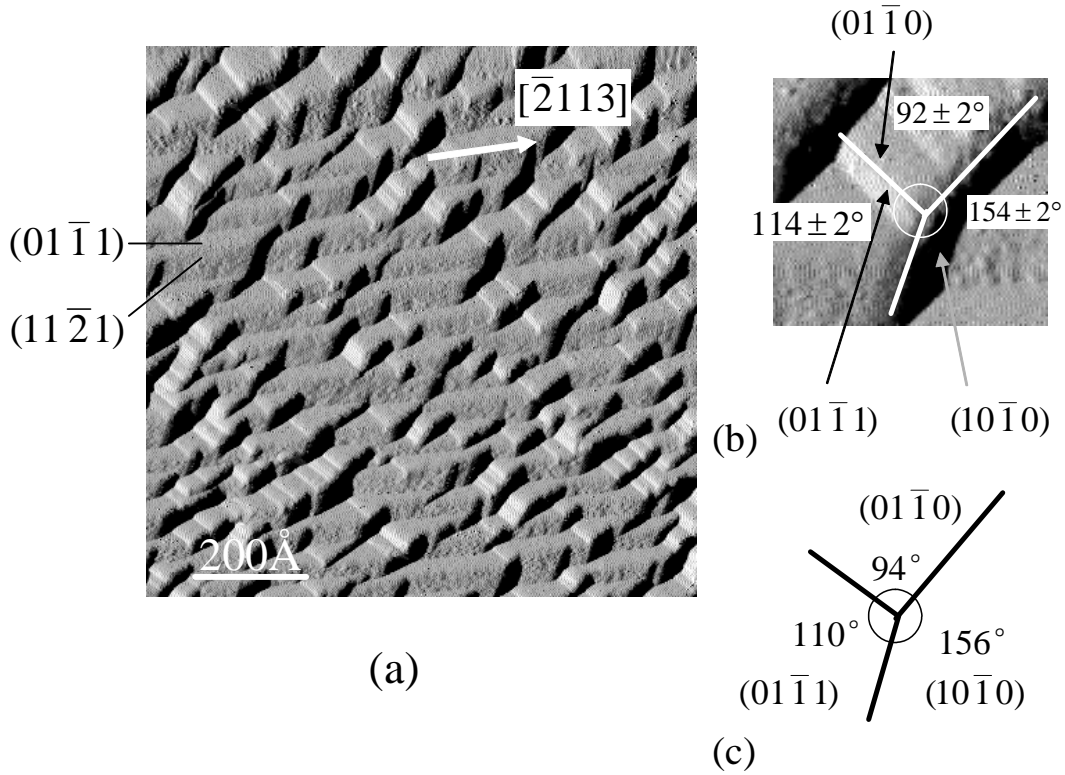
Fig. 3.8. (a) X-slope STM image of a faceted O/Re($12\overline{3}1$) surface prepared by dosing 10L O_2 ($\theta = 1ML$) at 300K followed by annealing at 1000K. (b) and (c) show measured and ideal azimuthal angles of edge lines formed by facets, respectively.

Fig. 3.8(a) is a typical X-slope STM image from a surface prepared by dosing 10L O_2 ($\theta = 1ML$) and annealing at 900K. Besides the ridges formed by $(11\overline{2}1)$ and $(01\overline{1}0)$ facets (light gray and gray areas) and truncated by $(10\overline{1}0)$ facets (dark areas), a fourth set of facets is also prominent, as shown by bright quasi-rectangular areas. Most of the fourth facets have limited size in one dimension, which explains why streaks rather than sharp spots are observed from the fourth facet in LEED as previously discussed in Fig. 3.5(a). The fourth facet, together with $(11\overline{2}1)$, $(01\overline{1}0)$, and $(10\overline{1}0)$ facets, can maintain the macroscopic orientation of the original planar substrate ($12\overline{3}1$).

Accordingly, the bunched steps on $(11\bar{2}1)$ disappear because they are not necessary to help maintain the $(12\bar{3}1)$ orientation. The orientation of the fourth facet is identified as $(01\bar{1}1)$ by measuring the angles between relevant edge lines. Fig. 3.8(b) shows a typical three-sided pyramid formed by $(01\bar{1}0)$, $(10\bar{1}0)$ facets and the fourth facet, in which the measured angles between the edge lines are labeled. For comparison, the ideal angles between the edge lines of $(01\bar{1}0)$, $(10\bar{1}0)$ and $(01\bar{1}1)$ facets are shown in Fig. 3.8(c); the small difference with the measured angle values may come from the fact that the edge lines are projected on a surface slightly deviated from the ideal $(12\bar{3}1)$ surface in the measurement because the sample surface is often not perpendicular to the tip during the STM scan. A previous study on $Re(01\bar{1}0)$ has also found that the surface forms the $(01\bar{1}1)$ facet when heated in oxygen atmosphere [33].

3.3.2 Atomic structure of the facets

Kinematical simulations of the LEED patterns agree well with the experimental results if we assume all the facets have the ideal bulk-truncated structures. STM images with atomic resolution can provide strong support for this assumption. Fig. 3.9(a) is an X-slope STM image showing the details of a 2-sided faceted surface with atomic resolution: the presence of herringbone structures. On the topside of the herringbones, the stripes are continuous as marked by a double line in Fig. 3.9(a); the stripes correspond to the close packed atomic rows on the $(01\bar{1}0)$ facet, in which individual atoms are not well resolved (see the hard sphere model in Fig. 3.9(c)). On the bottom side of the herringbones, some individual atoms on the $(11\bar{2}1)$ facet are resolved. In contrast to faceting on Pd/W(111) where the facet edges are truncated [30], the edges along $[\bar{2}113]$ are atomically sharp.
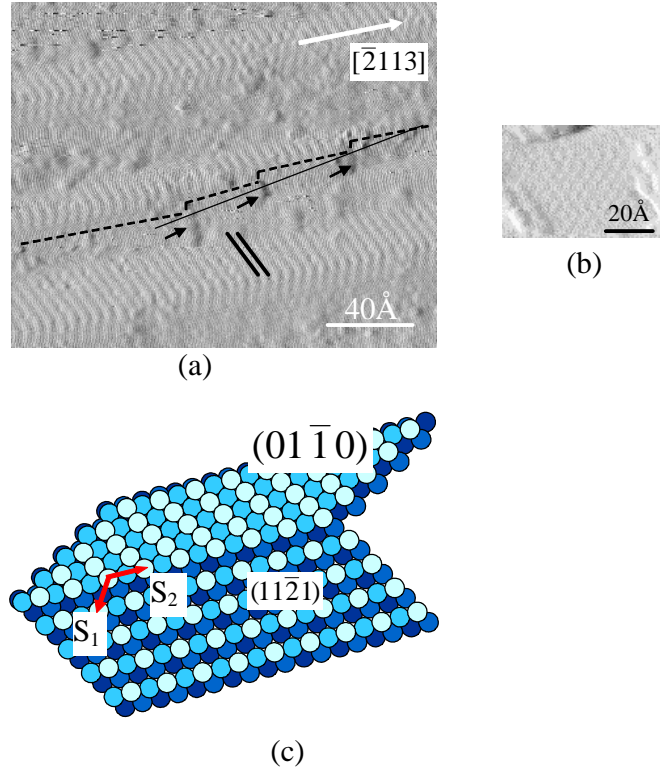
Fig. 3.9. Atomically resolved X-slope STM images of faceted O/Re($12\bar{3}1$) surfaces prepared under different conditions. (a) The surface is prepared by dosing 1L O_2 ($\theta = 0.7$ML) at 300K followed by annealing at 1000K; the dimensions of the image are 200Å×165Å. See text for the labels. (b) The surface is prepared by dosing 10L O_2 ($\theta = 1$ML) at 300K followed by annealing at 1000K; the dimensions of the image are 70Å×50Å. (c) A hard sphere model for the 2-sided faceting with two characteristic dimension parameters labeled as S_1 and S_2.

The quasi-hexagonal arrangements of the atoms on ($11\bar{2}1$) facets can be better seen in Fig. 3.9(b) taken from another surface with truncated ridges. For comparison, Fig. 3.9(c) shows a hard-sphere model of the bulk-truncated structures of ($01\bar{1}0$) and ($11\bar{2}1$) facets projected onto ($12\bar{3}1$), in which two unit vectors of ($11\bar{2}1$) are labeled as S_1 and S_2. The length of S_2 is also equal to the distance between atoms along [$\bar{2}113$] in two neighboring atomic rows on the ($01\bar{1}0$) facet. The ideal lengths of S_1 and S_2 are 5.24Å and 5.17Å, respectively, and the corresponding values measured in Fig. 3.9(a) and (b) are 5.3±0.2 Å and 5.1±0.2 Å. The good agreement further confirms the conclusions drawn from the

LEED study: the two sides of the ridge are $(01\bar{1}0)$ and $(11\bar{2}1)$, and no reconstruction occurs on these two facets.

One constraint on faceting is that the faceted structures must maintain the overall symmetry of the original planar surface [1]. In point group notation, the $Re(12\bar{3}1)$ surface has the lowest symmetry, C_1. Consequently, no higher symmetry should be found in all the faceted structures. One might think that the untruncated ridges display a 2-fold mirror symmetry perpendicular to the ridge direction $[\bar{2}113]$. However, when one considers the atomic arrangements on the two facets of the ridges (see Fig. 3.9(c)), the mirror symmetry does not exist.

Fig. 3.9(a) also provides insights into why the ridges that are not truncated by $(10\bar{1}0)$ facets have wedge-like terminations (see Fig. 3.6(a)). The $(11\bar{2}1)$ facet shown in the middle section of Fig. 3.9(a) actually consists of four terraces separated by three steps marked by three arrows. The interception lines along $[\bar{2}113]$ between the terraces and the top neighboring $(01\bar{1}0)$ facet are shifted from each other by a small amount (see the dashed lines in Fig. 3.9(a)). The overall envelope of the interception lines (see the solid lines in Fig. 3.9(a)) thus shows a deviation from the $[\bar{2}113]$ direction, resulting in a wedge-like end shape for the ridge.

3.3.3 Size dependence of the facets

Faceting is a thermodynamically driven but kinetically limited process [1, 10]. Several factors control the final facet size, including coverage of the adsorbate, annealing temperature and annealing time. For fixed oxygen coverage and annealing time, Fig. 3.10(a) and (b) show that the facet size grows as the annealing temperature increases.
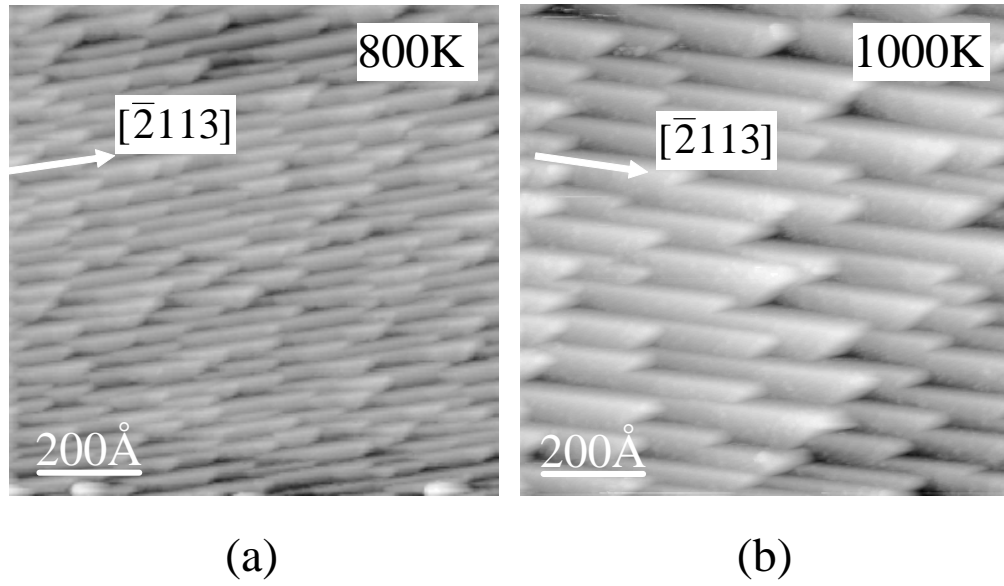
(a)   (b)

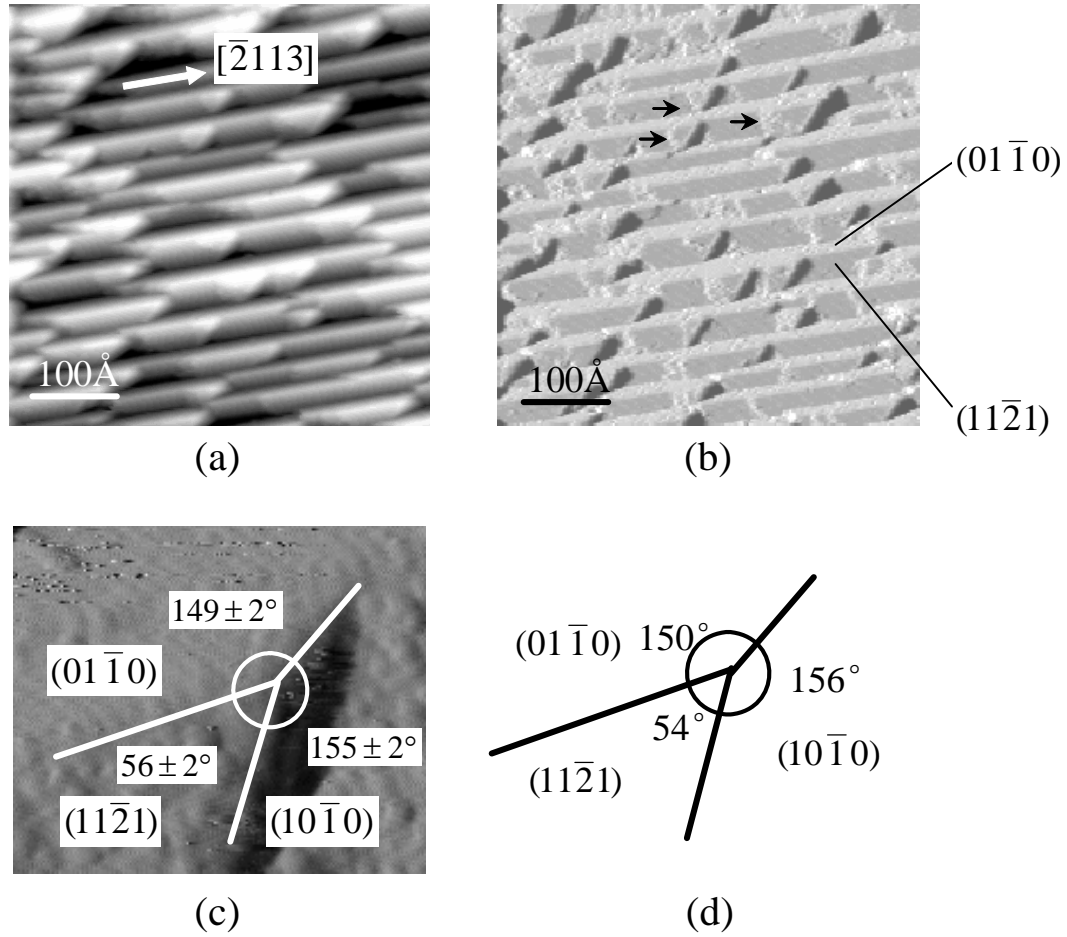Fig. 3.10. 1000Å×1000Å STM images of faceted O/Re($12\bar{3}1$) surfaces prepared by dosing 3L O_2 (θ = 0.9ML) at 300K followed by annealing at different temperatures for 2min. (a) 800K; (b)1000K.

Similarly, for fixed oxygen coverage and annealing temperature, the facet size increases
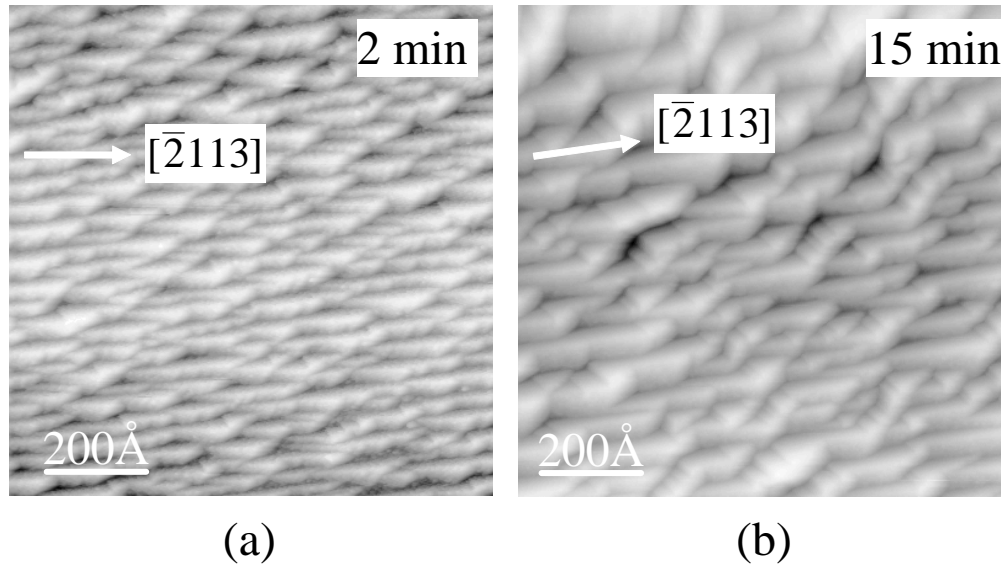
(a)   (b)

Fig. 3.11. 1000Å×1000Å STM images of faceted O/Re($12\bar{3}1$) surfaces prepared by dosing 10L O_2 (θ =1ML) at 300K followed by annealing at 900K for different time. (a) 2 minutes; (b) 15 minutes.

when the annealing time increases, as shown in Fig. 3.11(a) and (b). In this section, we

focus on how the facet size depends on oxygen coverage. Fig. 3.12 (a)-(c) show

morphologies of the faceted surfaces prepared with different oxygen coverages ranging

from 0.7ML to 1ML and the same annealing temperature (T = 800K) and annealing time
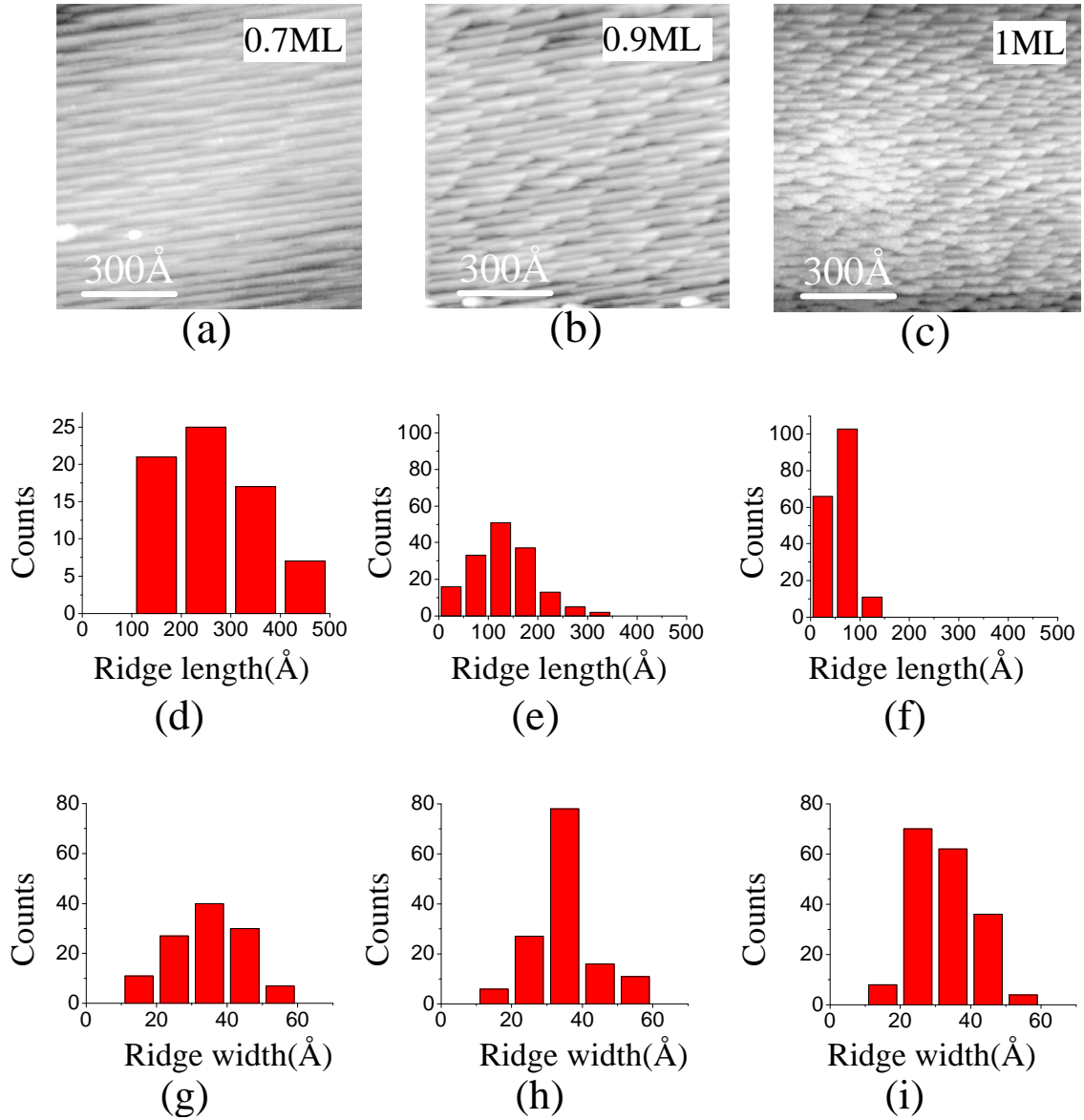
Fig. 3.12. (a)-(c) are STM images of faceted O/Re($12\bar{3}1$) surfaces prepared by dosing different amounts of O$_2$ at 300K followed by annealing at 800K for 2 minutes. The dimensions of all images are 1000Å×1000Å. (a) 1L, θ = 0.7ML; (b) 3L, θ = 0.9ML; (c) 10L, θ = 1ML. Histograms in (d)-(f) are the [$\bar{2}113$] ridge length distributions corresponding to (a)-(c). Histograms in (g)-(i) are the [$\bar{2}113$] ridge width distributions corresponding to (a)-(c). Only the top half region is surveyed in (c).

(t = 2min). Since for all the faceted structures, the ridges along the [$\bar{2}113$] direction are

present no matter whether they are truncated or not, we can use the ridge length and

width as two characteristic quantities to describe the facet size. The histograms in Fig.

3.12(d)-(f) are the ridge length distributions corresponding to the surfaces in Fig. 3.12(a)-

(c), and Fig. 3.12(g)-(i) show the ridge width distributions, respectively. Clearly, the most probable ridge length decreases when the oxygen coverage increases. However, although the profiles of the width distributions are quite different for surfaces with different oxygen coverage, the most probable ridge width does not vary much. To better illustrate these two different trends in the ridge length and width distributions, the mean values of the ridge length and width vs. oxygen coverage are plotted in Fig. 3.13(a) and (b) for two fixed annealing temperatures (800K and 1000K), in which the error bars show the corresponding standard deviations of the means. For any of the given oxygen coverages, both the ridge width and length increase with increasing annealing temperature. However, at the same annealing temperature, the mean ridge length decreases with increasing oxygen coverage, while the mean ridge width remains almost constant.
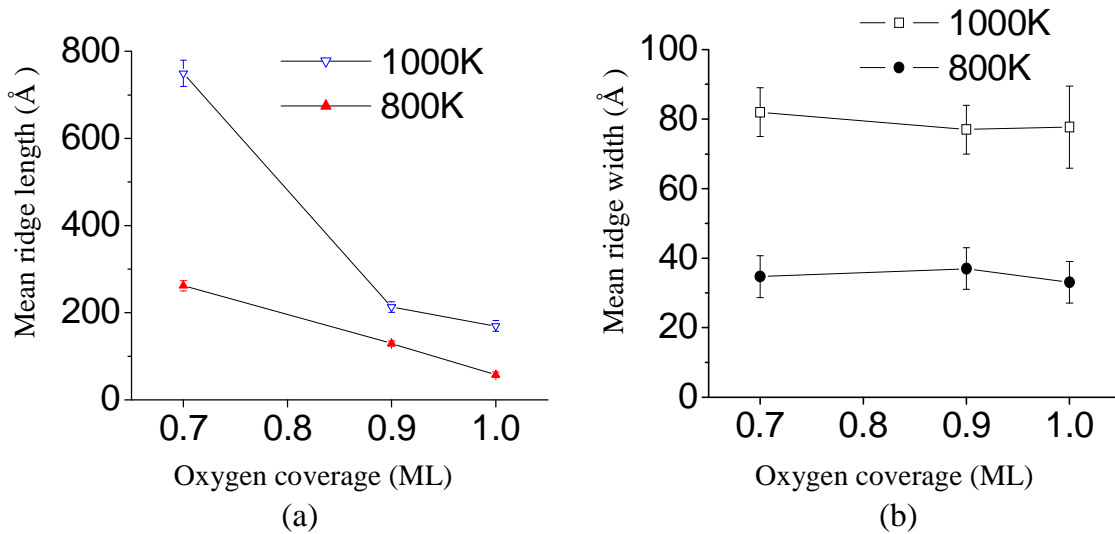
Fig. 3.13. (a) Plot of mean $[12\bar{3}1]$ ridge length vs. oxygen coverage upon annealing at 800K and 1000K. (b) Plot of mean $[\bar{2}113]$ ridge width vs. oxygen coverage upon annealing at 800K and 1000K.

3.4. Discussion

The thermodynamical analysis of faceting is usually conducted in the context of the equilibrium crystal shape (ECS) of a small crystal with fixed volume [34], and the

driving force for surface faceting is the anisotropy of surface free energy. When a planar surface forms facets, all the thermally stable facets must be present in the ECS [35], and the total surface free energy of the faceted surface $\sum_i \gamma_i A_i$ is smaller than that of the original planar surface, where γ_i is the surface free energy of facet i per unit area and A_i is the total surface area of facet i. For clean metal surfaces, the anisotropy of surface free energy is generally so small that a thermally annealed surface with relative high surface free energy (e.g. W(111), Ir(210) and Re($12\overline{3}1$)) can still retain its orientation against faceting [36, 37]. However, when the planar surface is covered by a thin layer of adsorbate atoms, the anisotropy of surface free energy can be increased to the extent that a faceted surface is more favorable energetically.

Specifically, for Re($12\overline{3}1$), if we ignore all edge energies, the energetic requirement for facet formation can be expressed as

$$\sum_i \frac{\gamma_i}{\cos\theta_i} \lambda_i - \gamma_{(12\overline{3}1)} < 0, \qquad (3.1)$$

where θ_i is the tilt angle between facet i and the ($12\overline{3}1$) plane, and λ_i is the structural coefficient describing the partial contribution of facet i to the total projected area on ($12\overline{3}1$) by all the facets, i.e. $\sum_i \lambda_i = 1$. Equation (3.1) is valid not only for a fully faceted surface but also for the coexistence of facets and the original planar surface at a steady state. From Eq. (3.1), the most likely facets are those having the lowest γ_i and the smallest θ_i. In general, the smoother a surface is, the smaller is the specific surface free energy. For example, although the most close-packed (0001) surface is expected to have the lowest γ_i, its θ_i is so large (78.5°) that the increase of surface area offsets the energy gain

from reducing specific surface energy. Therefore, the (0001) orientation does not appear in the facets observed experimentally.

To predict whether a planar surface can transform into specific facets requires knowledge of γ_i, which in most cases can only be obtained from complicated electronic structure calculations [38-41]. However, for clean metal surfaces with bulk-truncated structures, a useful qualitative comparison of γ_i can be achieved by simply counting the number of broken bounds when the bulk of a crystal is cleaved to form a surface [42]. To a first approximation, we consider only the nearest-neighbor bonds on clean Re surfaces. Since the c/a ratio of Re is 1.615, only 1.1% smaller than that of the ideal hcp lattice (1.633), we assume the bond strength is the same for the nearest-neighbor bonds in all orientations. Based on the broken-bond counting method, the surface energies of $(12\overline{3}1)$ and the possible facet candidates, when they are clean, are listed in Table 3.1 together with the tilt angles between the facets and the $(12\overline{3}1)$ surface. We also include in Table 3.1 the structural coefficients λ_i of $(11\overline{2}1)$ and $(01\overline{1}0)$ facets for the simplest faceting case in which the $(12\overline{3}1)$ surface transforms into ridges composed of only these two facets. If we apply Eq. (3.1) to this simplest case assuming all the involved surfaces are clean, we have

$$\frac{\gamma^{clean}_{(11\overline{2}1)}}{\cos\theta_{(11\overline{2}1)}}\lambda_{(11\overline{2}1)} + \frac{\gamma^{clean}_{(01\overline{1}0)}}{\cos\theta_{(01\overline{1}0)}}\lambda_{(01\overline{1}0)} - \gamma^{clean}_{(12\overline{3}1)} = 0. \tag{3.2}$$

Therefore, a clean Re$(12\overline{3}1)$ surface does not transform spontaneously into ridges with $(11\overline{2}1)$ and $(01\overline{1}0)$ facets because there is no energy gain for such a transformation, which agrees with the experimental observation that the clean Re$(12\overline{3}1)$ surface is always thermally stable. However, upon adsorption of oxygen and annealing,

Table 3.1. Specific surface energies γ_i of $(12\bar{3}1)$ and its vicinal surfaces when they are clean in the unit of broken-bond number per unit surface area. For comparison, the numerical ratios of specific surface energies between the facets and $(12\bar{3}1)$ are listed in the 3rd column. The tilt angles of the facets with respect to $(12\bar{3}1)$ are also given in both analytical and numerical forms. The last column shows the structure coefficients λ_i of facets in the simplest case: the planar $(12\bar{3}1)$ surface completely transforms into 2-sided ridges composed of $(11\bar{2}1)$ and $(01\bar{1}0)$ facets.

surface	γ_i	$\dfrac{\gamma_i}{\gamma_{(12\bar{3}1)}}$	$\cos\theta_i$	θ_i	$\dfrac{\gamma_i}{\gamma_{(12\bar{3}1)}\cos\theta_i}$	λ_i
$(12\bar{3}1)$	$\dfrac{38}{a\sqrt{3a^2+28c^2}}$	1	1	0°	1	—
$(11\bar{2}1)$	$\dfrac{26}{a\sqrt{3a^2+12c^2}}$	1.02	$\dfrac{3a^2+18c^2}{\sqrt{(3a^2+28c^2)(3a^2+12c^2)}}$	12.0°	1.04	$\dfrac{3a^2+18c^2}{3a^2+28c^2}$
$(01\bar{1}0)$	$\dfrac{6}{ac}$	0.85	$\dfrac{5c}{\sqrt{3a^2+28c^2}}$	22.1°	0.92	$\dfrac{10c^2}{3a^2+28c^2}$
$(10\bar{1}0)$	$\dfrac{6}{ac}$	0.85	$\dfrac{4c}{\sqrt{3a^2+28c^2}}$	42.2°	1.15	—
$(01\bar{1}1)$	$\dfrac{14}{a\sqrt{3a^2+3c^2}}$	0.88	$\dfrac{3a^2+10c^2}{\sqrt{(3a^2+28c^2)(3a^2+12c^2)}}$	24.5°	0.97	—
$(11\bar{2}0)$	$\dfrac{4\sqrt{3}}{ac}$	0.98	$\dfrac{3\sqrt{3}c}{\sqrt{3a^2+28c^2}}$	15.6°	1.02	—
$(11\bar{2}2)$	$\dfrac{14}{a\sqrt{3a^2+4c^2}}$	0.98	$\dfrac{\sqrt{3}(a^2+3c^2)}{\sqrt{(3a^2+28c^2)(a^2+c^2)}}$	22.7°	1.06	—

the Re$(12\bar{3}1)$ surface is observed to form $(11\bar{2}1)$ and $(01\bar{1}0)$ facets; this indicates that oxygen can induce an anisotropic change of the surface free energies of $(12\bar{3}1)$, $(11\bar{2}1)$ and $(01\bar{1}0)$ so that Eq. (3.2) is no longer valid but Eq. (3.1) is fulfilled.

Generally, the adsorption of oxygen reduces the free energy of a surface; for example, the surface free energies of most metal oxides are invariably lower than those of the corresponding metal surfaces [38, 43]. More importantly, oxygen can induce enhancement of the anisotropy of surface free energy, which may be explained in terms

of preferential adsorption of oxygen on certain facets. In all discussion of coverage-dependent morphology to this point, we have used the average coverage of oxygen on the planar $Re(12\bar{3}1)$ surface as the reference for comparison. When faceting occurs, the actual oxygen coverages on different facets may be different, which, when coupled with possible different O-Re binding energies on different facets, leads to different amounts of surface energy reduction, i.e. increase of the anisotropy of surface free energy. Such an oxygen-induced enhancement of surface energy anisotropy is also observed in other systems: Avraamov *et al.* in an early experiment reported the influence of oxygen on the anisotropy of the surface free energy of silicon(3%)-iron alloy surfaces using the zero creep method [44]; recently, Walko *et al.* reported that in oxygen-induced faceting on Cu(115), the surface energy of (104) decreases with an increase of oxygen coverage and the resulting anisotropy causes the Cu(115) surface to form both {104} facets and stepped facets, which gradually shift to the (113) orientation [45].

For surface faceting, a necessary condition is that the area-weighted combinations of all the facets and steps must retain the original macroscopic orientation of the planar surface, which, together with the energy requirement in Eq. (3.1), can give a qualitative explanation of the coverage-dependent evolution of surface morphology. Since for clean surfaces, $(01\bar{1}0)$ has the smallest γ_i and the lowest value of $\gamma_i/\cos\theta_i$ among those near $(12\bar{3}1)$, it must appear as a facet and be the major source of lowering the total surface energy if adsorbate-induced faceting ever occurs on $Re(12\bar{3}1)$. This explains why only the $(11\bar{2}1)$ facet appears with $(01\bar{1}0)$ to form ridges along $[\bar{2}113]$ at low average oxygen coverages ($0.7ML \leq \theta < 0.9ML$), although it is rough with four layers of atoms exposed and has higher surface energy than $(12\bar{3}1)$ when both are clean (see Table 3.1).

At low average oxygen coverages ($0.7ML \leq \theta < 0.9ML$), the remaining oxygen atoms after preferential adsorption on ($01\bar{1}0$) facets may not be sufficient to modify γ_i of another possible facet i significantly so that $\gamma_i/\cos\theta_i$ is probably still close to that of the clean surface listed in Table 3.1. The ($11\bar{2}1$) surface is the only possible choice that is close enough to ($12\bar{3}1$) ($\theta_{(11\bar{2}1)} = 12.0°$) with a medium value of $\gamma_i/\cos\theta_i$ and can retain the ($12\bar{3}1$) orientation by forming ridges with the ($01\bar{1}0$) facet. Other attempts to retain the ($12\bar{3}1$) orientation are unfavorable because they either involve surfaces with higher $\gamma_i/\cos\theta_i$ to form ridges or require larger mass transport to form more complex structures. On the other hand, since the ($11\bar{2}1$) surface is atomically rough and does not appear in the ECS of a hcp crystal [42], it is also a metastable phase. When the average oxygen coverage increases ($\theta > 0.9ML$), some surface may appear as a new facet because it now has enough oxygen available to reduce γ_i so that $\gamma_i/\cos\theta_i$ becomes much less than that of ($11\bar{2}1$). This is especially true for ($10\bar{1}0$) since it has the same surface structure as the favored ($01\bar{1}0$) facet and can have the same low surface energy as $\gamma_{(01\bar{1}0)}$. The total surface free energy is reduced by replacing the ($11\bar{2}1$) facet with ($10\bar{1}0$) that has lower γ_i, resulting in the truncation of the ridges and decrease of the average ridge length. When the Re($12\bar{3}1$) crystal is held at 900K while dosing oxygen, the ($11\bar{2}1$) facet can even disappear completely [46].

In the above discussion, the contribution of edge energy is ignored. In fact, reducing the edge energy is the dominating factor for dependence of facet size on annealing temperature and time [10]. For a fully faceted surface under steady state conditions, the total surface area for each facet is fixed no matter what facet size distribution there is. No

energy gain can be made by simply increasing the mean facet size. However, the edge density is reduced for bigger facet size, providing a driving force for the observed increasing of facet size at higher annealing temperature and longer annealing time. Similar phenomena have also been observed in the faceting of O/Ir(210), Pd/W(111) and Pt/W(111) [8, 10, 47].

Being driven by surface thermodynamics, the faceting process is also controlled by kinetics of nucleation and surface diffusion. According to Che *et al.* [48], when faceting occurs, there is always a nucleation barrier associated with the edge energy and the anisotropy of surface free energy; a lower barrier requires lower edge energy and larger surface energy anisotropy. That faceting on $O/Re(12\bar{3}1)$ occurs only when the annealing temperature is higher than 700K is a manifestation that there exists such an energy barrier to overcome toward faceting. Large facet size can be achieved by either annealing at higher temperature for shorter time or at lower temperature for longer time (see Fig. 3.10(b) and Fig. 3.11(b)). This indicates the diffusion rate is important in determining the facet size.

3.5. Conclusion

We have found that the adsorption of oxygen can induce faceting of $Re(12\bar{3}1)$, and the morphology of the faceted surface depends on oxygen coverage. For oxygen coverage $\theta < 0.5$ML, the $O/Re(12\bar{3}1)$ surface remains planar upon annealing. However, for 0.5ML $\leq \theta < 0.7$ML, the $O/Re(12\bar{3}1)$ surface becomes partially faceted upon annealing at $\geq$700K. For 0.7ML $\leq \theta < 0.9$ML, the $O/Re(12\bar{3}1)$ surface becomes completely faceted, forming long sawtooth ridges which are composed of $(01\bar{1}0)$ and $(11\bar{2}1)$ facets upon

annealing at ≥700K. The distance between the ridges is quite uniform and the ridges have atomically sharp edges. For 0.9ML ≤ θ < 1ML, similar annealing treatment leads to the emergence of $(10\bar{1}0)$ facets which truncate the original ridges. With the surface fully covered by oxygen (θ = 1ML), a fourth facet $(01\bar{1}1)$ becomes prominent. This morphological evolution is accompanied by the reduction of the average ridge length along $[\bar{2}113]$, indicating that the $(11\bar{2}1)$ facet is metastable.

Our work demonstrates that even in a simple adsorbate/substrate system, the adsorbate-induced modification of the anisotropy of surface free energy can bring a complex change of the surface morphology. This complex morphological evolution is perhaps related to the low symmetry of the Re($12\bar{3}1$) surface, which reduces the symmetry constraint of faceted structures and leads to wider choices of facet orientations. Theoretical studies are necessary to give detailed energetic descriptions of the bonding characteristics between oxygen and Re on different facets, which, we believe, drives the change of surface energy anisotropy. Since the morphology of the faceted structures can be controlled by adjusting oxygen coverage, the faceted Re surfaces provide plausible model systems to study structure sensitivity in Re-based catalytic reactions as well as promising templates to grow nano-structures, perhaps nano-wires.

3.6 Acknowledgment

3.7 References

[1]   Q. Chen and N. V. Richardson, Prog. Surf. Sci. **73** (2003) 59.
[2]   R. E. Kirby, C. S. McKee and R. W. Roberts, Surf. Sci. **55** (1976) 725.
[3]   R. E. Kirby, C. S. McKee and L. V. Renny, Surf. Sci. **97** (1980) 457.
[4]   K. Pelhos, J. B. Hannon, G. L. Kellogg and T. E. Madey, Surf. Sci. **432** (1999) 115.
[5]   K. J. Song, J. C. Lin, M. Y. Lai and Y. L. Wang, Surf. Sci. **327** (1995) 17.
[6]   D. B. Danko, M. Kuchowicz and J. Kolacziewicz, Surf. Sci. **552** (2004) 111.
[7]   A. T. S. Wee, J. S. Foord, R. G. Egdell and J. B. Pethica, Phys. Rev. B **58** (1998) R7548.
[8]   I. Ermanoski, K. Pelhos, W. Chen, J. S. Quinton and T. E. Madey, Surf. Sci. **549** (2004) 1.
[9]   M. Sander, R. Imbihl, R. Schuster, J. V. Barth and G. Ertl, Surf. Sci. **271** (1992) 159.
[10]   T. E. Madey, J. Guan, C.-H. Nien, H.-S. Tao, C.-Z. Dong and R. A. Campbell, Surf. Rev. and Lett. **3** (1996) 1315.
[11]   T. E. Madey, C.-H. Nien, K. Pelhos, J. J. Kolodziej, I. M. Abdelrehim and H.-S. Tao, Surf. Sci. **438** (1999) 191.
[12]   R. A. Campbell, J. Guan and T. E. Madey, Catal. Lett. **27** (1994) 273.
[13]   R. Barnes, I. M. Abdelrehim and T. E. Madey, Topics in Catalysis **14** (2001) 53.
[14]   W. Chen, I. Ermanoski, Q. Wu, T. E. Madey, H. Hwu and J. G. Chen, J. Phys. Chem B **107** (2003) 5231.
[15]   W. Chen, I. Ermanoski and T. E. Madey, J. AM. CHEM. SOC. **127** (2005) 5014.
[16]   W. Chen, I. Ermanoski, T. Jacob and T. E. Madey, Langmuir **22** (2006) 3166.
[17]   L. S. Wang, R. Ohnishi and M. Ichikawa, J. Catal. **190** (2000) 276.
[18]   Y. Z. Yuan, H. C. Liu, H. Imoto, T. Shido and Y. Iwasawa, J. Catal. **195** (2000) 51.
[19]   F. Solymosi, P. Tolmacsov and T. S. Zakar, J. Catal. **233** (2005) 51.
[20]   K. Liu, S. C. Fung, T. C. Ho and D. S. Rumschitzki, J. Catal. **206** (2002) 188.
[21]   A. S. Y. Chan, W. Chen, H. Wang, J. E. Rowe and T. E. Madey, J. Phys. Chem. B **108** (2004) 14643.
[22]   A. S. Y. Chan, G. K. Wertheim, H. Wang, M. D. Ulrich, J. E. Rowe and T. E. Madey, Phys. Rev. B **72** (2005) 035442.
[23]   D. E. Gray, *American Institute of Physics Handbook (3rd edition)*, 3rd edition ed., McGraw-Hill, (1972).
[24]   C.-H. Nien and T. E. Madey, Surf. Sci. **433** (1999) 254.
[25]   A. Szczepkowicz, A. Ciszewski, R. Bryl, C. Oleksy, C.-H. Nien, Q. F. Wu and T. E. Madey, Surf. Sci. **599** (2005) 55.
[26]   R. Pantel and M. Bujor, Surf. Sci. **83** (1979) 228.
[27]   C. Morant, L. Galan and J. M. Sanz, Anal. Chim. Acta **297** (1994) 179.
[28]   M.-C. Desjonqueres and D. Spanjaard, *Concepts in surface physics*, Springer-Verlag, (1993).
[29]   G. K. L. Cranstroun and D. R. Pyke, Surf. Sci. **60** (1976) 157.
[30]   C.-H. Nien and T. E. Madey, Surf. Sci. **380** (1996) L527.
[31]   T.Suzuki, Y. Temko, M. C. Xu and K. Jacobi, Surf. Sci. **573** (2004) 457.

[32] F. K. Men, F. Liu, P. J. Wang, C. H. Chen, D. L. Cheng, J. L. Lin and F. J. Himpsel, Phys. Rev. Lett. **88** (2002) 096105.
[33] D. M. Zehner and H. E. Farnsworth, Surf. Sci. **30** (1971) 335.
[34] E. D. Williams and N. C. Bartelt, Ultramicroscopy (1989).
[35] C. Herring, Phys. Rev. **82** (1951) 87.
[36] M. Drechsler and A. Müller, J. Crystal Growth **3/4** (1968) 518.
[37] R. Kumar and H. E. Grenga, Surf. Sci. **50** (1975) 399.
[38] L. Vitos, A. V. Ruban, H. L. Skriver and J. Kollar, Surf. Sci. **411** (1998) 186 and reference therein.
[39] D. Yu and M. Scheffler, Phys. Rev. B **70** (2004) 155417.
[40] H. P. Bonzel and M. Nowicki, Phys. Rev. B **70** (2004) 245430.
[41] M. J. S. Spence, A. Hung, I. K. Snook and I. Yarovsky, Surf. Sci. **513** (2002) 389.
[42] G. A. Wolff and J. G. Gualtieri, Am. Mineral. **47** (1962) 562.
[43] S. H. Overbury, P. A. Bertrand and G. A. Somorjai, Chem. Rev. **75** (1975) 547.
[44] Y. S. Avraamov, A. G. Govozdev and V. M. Kutsak, Phys. Met. Metallogr. **39** (1975) 84.
[45] D. A. Walko and I. K. Robinson, Phys. Rev. B **64** (2001) 045412.
[46] H. Wang, A. S. Y. Chan, P. Kaghazchi, T. Jacob and T. E. Madey, ACS Nano **1** (2007) 449.
[47] C.-Z. Dong, S. M. Shivaprasad, K. J. Song and T. E. Madey, J. Chem. Phys. **99** (1993) 9172.
[48] J. G. Che, C. T. Chan, C. H. Kuo and T. C. Leung, Phys. Rev. Lett. **79** (1997) 4230.
[49] H. Wang, W. Chen and T. E. Madey, Phys. Rev. B **74** (2006) 205426.

Chapter 4 Facet stability in oxygen-induced nano-faceting of Re($12\bar{3}1$)

4.1 Introduction

In Chapter 3 we have reported a complex morphological evolution of faceting on Re($12\bar{3}1$) when the surface is covered by oxygen at 300K and annealed at T>700K [1, 2]. As shown in Fig. 4.1 (a) and (b), the Re($12\bar{3}1$) surface is atomically rough with 6 layers of atoms exposed; it has relatively high surface free energy and high probability to form facets when covered by certain adsorbates and annealed. The morphology of the
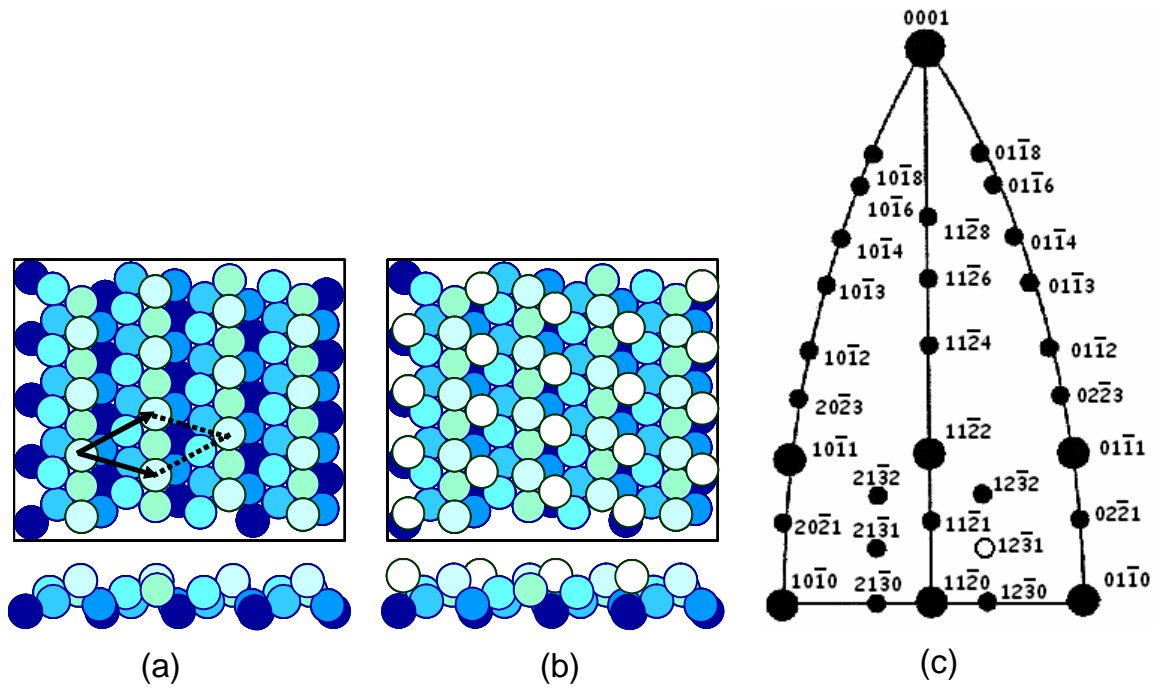
Fig. 4.1. Ball models of the Re($12\bar{3}1$) surface showing two different stacking sequences (a) and (b). A unit cell is also labeled in (a). (c) Stereographic projection of the hcp lattice on the ($11\bar{2}0$) plane. The ($12\bar{3}1$) surface is labeled by a hollow circle.

faceted surface depends on the initial oxygen coverage on Re($12\bar{3}1$) and the evolution of facets is believed to be induced by the change of surface energy anisotropy due to adsorption of oxygen. When oxygen coverage (θ) is between 0.7 monolayer (ML) and 0.9 ML, long ridges formed by ($01\bar{1}0$) and ($11\bar{2}1$) facets emerge on Re($12\bar{3}1$) upon

annealing [1]; here 1ML refers to the saturation coverage of oxygen at 300K. According to an early measurement of oxygen adsorption on another reactive transition metal surface, W(100) [3], the approximate limit of oxygen concentration imposed by room temperature exposure to Re(12$\bar{3}$1) can be estimated as ~1×10^{15} cm^{-2}. For 0.9ML< θ < 1ML, the ridges become truncated by a third facet (10$\bar{1}$0), which has the same surface structure as (01$\bar{1}$0) but higher tilt angle with respect to (12$\bar{3}$1) [1]. When Re(12$\bar{3}$1) is fully covered by oxygen (θ=1ML), a fourth facet (01$\bar{1}$1) also emerges upon annealing [1]. The spatial relationship between Re(12$\bar{3}$1) and all the observed facets is shown in the stereographic projection plot of the hcp lattice in Fig. 4.1(c). It is not surprising that (01$\bar{1}$0), (10$\bar{1}$0) and (01$\bar{1}$1) appear as facets because they all have rather smooth surfaces and thus low surface free energies. However, the last facet that forms, (11$\bar{2}$1), is atomically rough with four layers of atoms exposed; this raises the question why it appears as a facet. One clue lies in the experimental observation that the surface area occupied by (11$\bar{2}$1) decreases when the initial oxygen coverage increases [1], indicating that the (11$\bar{2}$1) facet may be metastable if oxygen coverage exceeds the limit imposed by oxygen adsorption at 300K.

In this chapter we build upon our previous work [1] and demonstrate that the stability of the (11$\bar{2}$1) facet indeed relies on surface oxygen concentration by investigating the faceting behavior of Re(12$\bar{3}$1) when oxygen is adsorbed at high temperatures. In contrast to the behavior observed for room temperature adsorption followed by annealing [1], the (11$\bar{2}$1) facet completely disappears and a new facet (10$\bar{1}$1) emerges together with the other three facets when Re(12$\bar{3}$1) is exposed to >120L (1L = 10^{-6} Torr·s = 1.33×10^{-4} Pa·s) of oxygen between 800 and 1000K. Only at higher substrate

temperatures ($>\sim$1200K) does the ($10\bar{1}1$) facet become unfavorable, and the faceted surface reverts to the previous morphology including the ($11\bar{2}1$) facet. Our results demonstrate the complexity of surface morphology in adsorbate-induced faceting of hcp metal surfaces and have important implications for Re-based catalysts that operate under oxygen-rich conditions since the structure of the catalysts often affect their performance.

4.2 Experimental and computational procedures

The experimental procedures are similar to that described in Chapter 3. The major difference is that oxygen is now adsorbed on Re($12\bar{3}1$) at elevated substrate temperatures in stead of room temperature. All the LEED and STM experiments are performed after the oxygen-covered surface is cooled to room temperature. The STM images are presented in the differential mode to enhance details of the facets: the measured height variation is differentiated along the X direction and regions having the same X-slope are represented by the same gray color. The high resolution soft X-ray photoemission spectroscopy (HRSXPS) measurements are conducted on beamline U4A of the National Synchrotron Light Source (NSLS) at Brookhaven National Laboratory [4]. The UHV end-station chamber is equipped with a VSW 100 mm hemispherical analyzer operating at a pass energy of 2eV and the total instrumental resolution is about 150 meV.

The O-Re binding energies on several Re surfaces are calculated by density functional theory (DFT) using the CASTEP code [5]. Throughout the calculations, optimized Vanderbilt-type ultrasoft pseudopotentials [6] and the generalized gradient approximation (GGA) exchange-correlation functional suggested by Perdew, Burke, and

Ernzerhof (PBE) [7] are used. The calculations are performed by Jacob and Kaghazchi [8]. Re($10\bar{1}1$), ($01\bar{1}0$) and ($11\bar{2}1$) surfaces are represented by 14-layer 11-layer and 19-layer slabs with ~13 Å vacuum, respectively. For each system, the bottom four layers are fixed at the calculated bulk-crystal structure, and the remaining Re atoms and the adsorbates are allowed to relax freely. For the oxygen-adsorbed system, the cutoff energy is converged to 380 eV, and the Brillouin zone (BZ) sampling of the (1×1) unit cell is converted to 4×4, 5×8 and 4×8 Monkhorst-Pack meshes for Re($11\bar{2}1$), ($01\bar{1}0$)and ($10\bar{1}1$), respectively [9].

4.3 Results

Figure 4.2(a) shows a typical low energy electron diffraction (LEED) pattern from a fully faceted surface prepared by dosing 120L O_2 at 300K followed by annealing at 900K. None of the LEED spots converges to the screen center when the incident electron energy (E_e) increases, indicating the surface is completely faceted. This LEED pattern is almost the same as that in our previous report, where the surface is prepared by dosing 10L O_2 (θ = 1ML) at 300K followed by annealing at 1000K [1]. Following the procedure described in chapter 3, we can identify representative but relatively weak spots from ($11\bar{2}1$) facets as marked by arrows in Fig. 4.2(a). However, when the same amount of O_2 (120L) is dosed at 900K, the LEED pattern changes: LEED spots from the ($11\bar{2}1$) facets completely disappear and more streaky features appear (see Fig. 4.2(b)). Some of the new streaky features (two examples labeled by arrows in Fig. 4.2(b)) also do not move toward the converging centers of the facets seen in Fig. 4.2(a) as E_e is changed, indicating the formation of new facets.
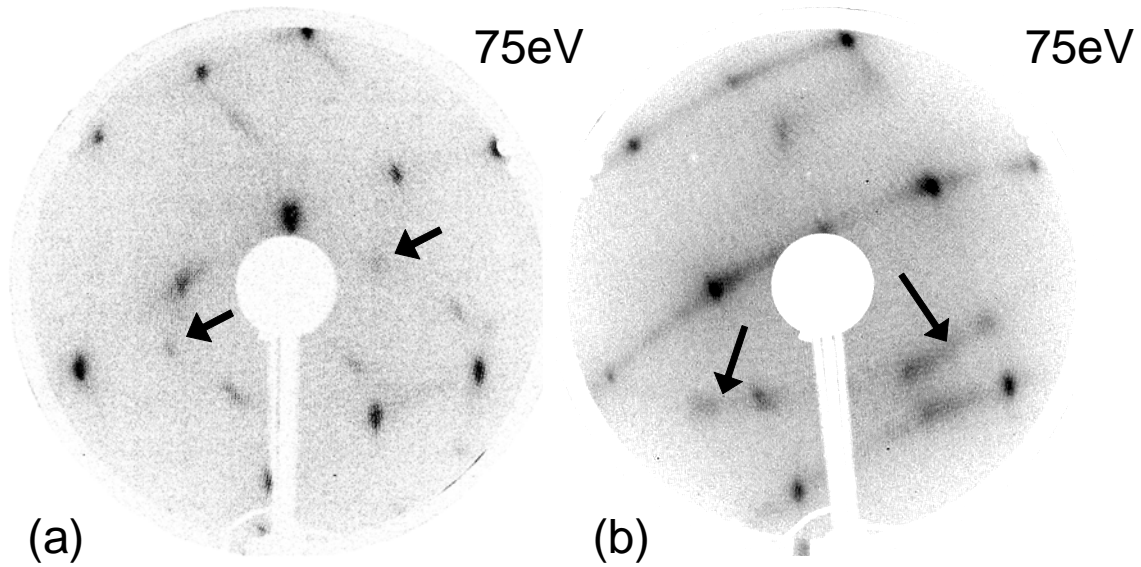
Fig. 4.2. LEED patterns of faceted Re($12\overline{3}1$) surfaces prepared by (a) dosing 120L O_2 at 300K followed by annealing at 900K; (b) dosing 120L O_2 at 900K.

The morphological changes can be better revealed in scanning tunneling microscopy (STM) measurements. Fig. 4.3(a) is a typical STM image taken from a faceted surface prepared by dosing 120L O_2 at 300K followed by annealing at 900K. The morphology is the same as reported before: four different facets of orientations ($11\overline{2}1$), ($01\overline{1}0$), ($01\overline{1}1$) and ($10\overline{1}0$) are present [1]. Fig. 4.3(b) is a typical STM image taken after the Re($12\overline{3}1$) surface is exposed to 120L O_2 at 900K, in which we can identify three of the four facets that appear in Fig. 4.3(a). However, a notable difference is that the ($11\overline{2}1$) facet totally disappears and a new facet takes its place. This observation is consistent with the LEED results. Since the area-weighted combinations of all the observed facets must retain the orientation of the macroscopic Re($12\overline{3}1$) surface, the replacement of ($11\overline{2}1$)by the new facet is accompanied by the rebalancing of the relative amounts of the other three remaining facets; for example, the ($01\overline{1}0$) and ($01\overline{1}1$) facets occupy more surface area per projected unit area on Re($12\overline{3}1$) in Fig. 4.3(b) than in Fig. 4.3(a). The

(a)

(b)
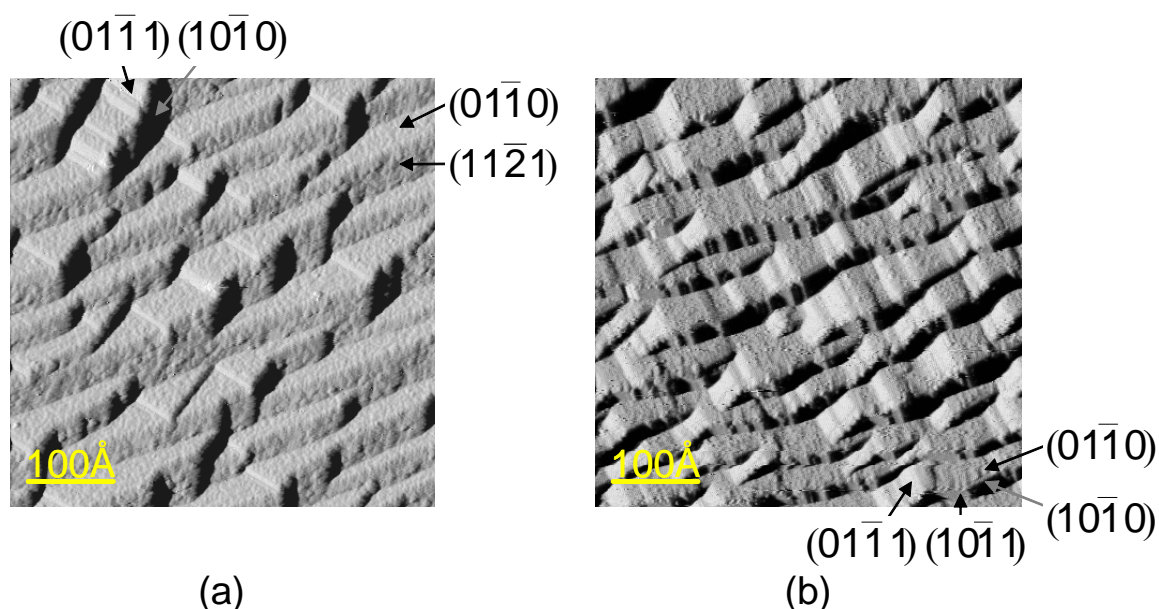
Fig. 4.3. 500Å×500Å STM images of faceted Re($12\overline{3}1$) surfaces prepared by (a) dosing 120L O_2 at 300K followed by annealing at 900K; (b) dosing 120L O_2 at 900K.

orientation of the new facet can be identified by measuring the angles between the edge lines of neighboring facets. The results of the angle measurements are shown in Fig. 4.4(a) and the only plausible facet that gives good agreement is ($10\overline{1}1$) (see Fig. 4.4(b)).

(a)

(b)
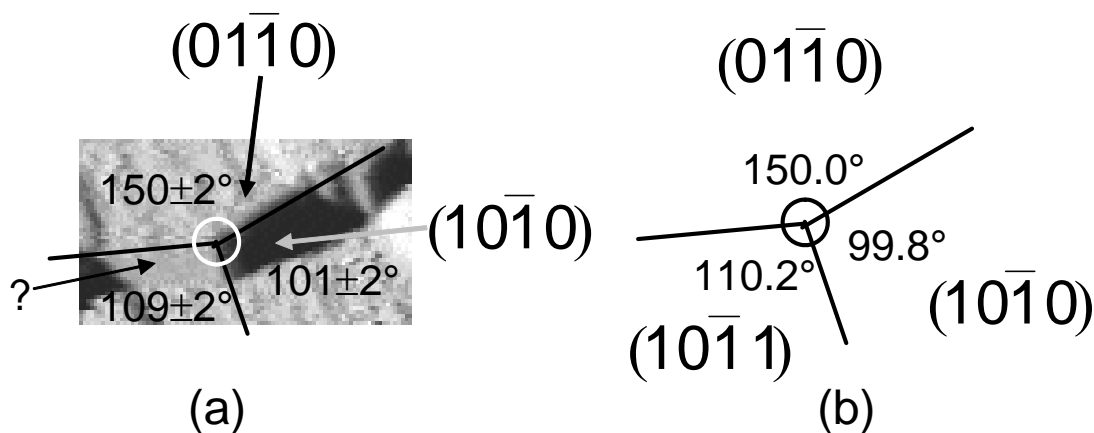
Fig. 4.4. (a) A 220Å×120Å STM image showing measurements of the angles between intersection lines of ($01\overline{1}0$), ($01\overline{1}1$) and the new facet. (b) Ideal angle values calculated from the projected intersection lines between ($01\overline{1}0$), ($01\overline{1}1$) and ($10\overline{1}1$) on the ($12\overline{3}1$) surface.

This morphological phase transition occurs only in a narrow temperature window. Fig. 4.5(a), (b) and (c) show STM images of the surface morphology after Re($12\overline{3}1$) is
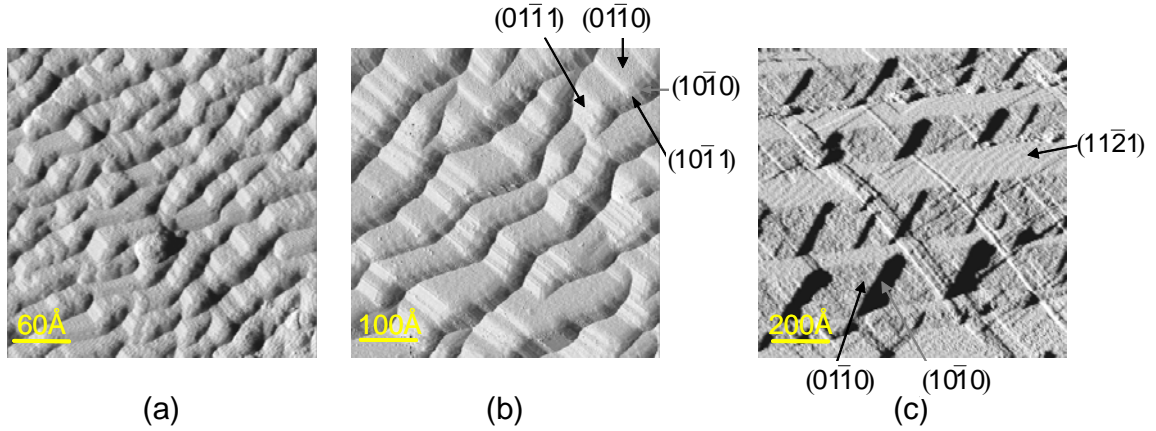
Fig. 4.5. STM images of faceted Re($12\bar{3}1$) surfaces prepared by dosing 360L O_2 at different temperatures. (a) 800K, 300Å×300Å; (b) 1000K, 500Å×500Å; (c) 1200K, 1000Å×1000Å.

exposed to 360L O_2 at 800K, 1000K and 1200K, respectively. The average facet size increases with temperature but the ($10\bar{1}1$) facet only exists when the substrate temperature is between 800K and 1000K during oxygen exposure. When the sample is heated at 1200K during oxygen exposure, not only the ($11\bar{2}1$) facet reemerges but also the ($01\bar{1}1$) facet almost disappears. Note that in Fig. 4.5(c) there are many steps on ($11\bar{2}1$) facets. Although a combination of only ($01\bar{1}0$), ($10\bar{1}0$) and ($11\bar{2}1$) facets cannot retain the macroscopic orientation of the Re($12\bar{3}1$) (see the stereographic projection in Fig. 4.1(c)), these steps lead to local effective orientations that deviate from ($11\bar{2}1$) and help retain the macroscopic orientation.

The chemical properties of the faceted Re($12\bar{3}1$) surfaces prepared under different conditions are investigated by HRSXPS. Figure 4.6(a) shows a Re4$f_{7/2}$ spectrum taken from the faceted Re($12\bar{3}1$) surface prepared by dosing 10L O_2 at 300K followed by annealing at 1000K. Besides the Re bulk peak at 40.3 eV, the Re4$f_{7/2}$ spectrum shows distinct features on the higher binding energy side that reflect Re4$f_{7/2}$ surface core level shifts (SCLS) induced by Re-O bonding in different chemical environments. Four SCLS
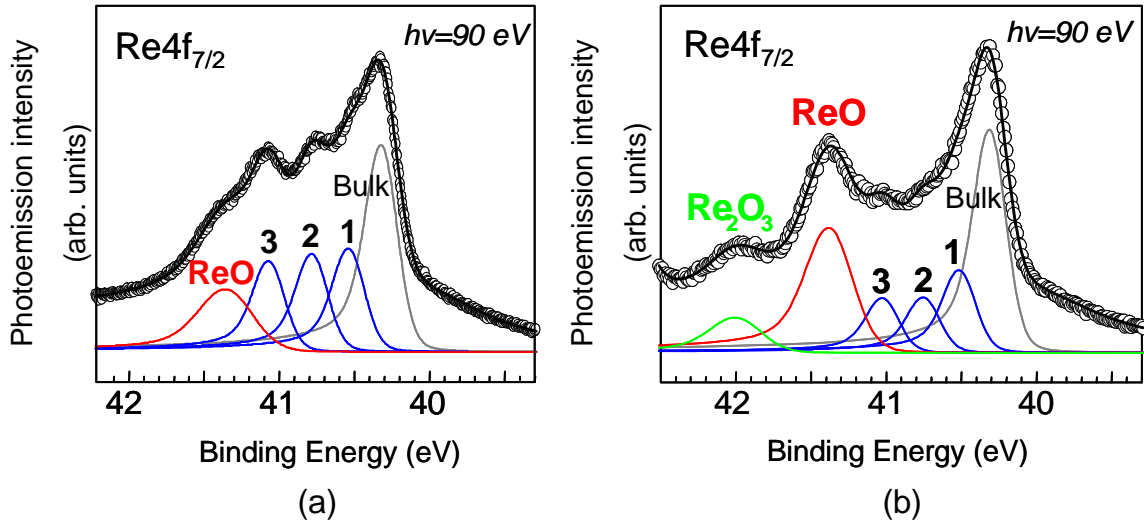
Fig. 4.6. HRSXPS spectra of Re4f$_{7/2}$ taken with normal emission angle from surfaces prepared by (a) dosing 10L O$_2$ (θ=1ML) followed by annealing at 1000K and (b) dosing 300L O$_2$ at 1000K. The photon energy is 90eV. The peak components labeled as 1, 2, and 3 correspond to Re atoms bonded to 1, 2, and 3 O atoms, respectively. The peak components for Re bulk and surface oxides ReO and Re$_2$O$_3$ are also labeled.

components are needed to fit the Re4f$_{7/2}$ spectrum satisfactorily and details of the fitting

procedure have been described elsewhere [2, 10]. The components labeled as 1, 2, and 3

in Fig. 4.6(a) correspond to SCLS of 0.22, 0.45 and 0.73eV, respectively; they are

assigned to surface Re atoms bonded to one, two and three O atoms based on similar

shifts measured on the p(2×1)-O/Re(0001) surface [11]. The component with a 1.03 eV

binding energy shift is attributed to the formation of a surface oxide ReO by comparing

the shift with those for Re oxides and assuming that core level shifts are additive for

oxidation states [12]. Similar binding energy shifts (1-1.1 eV) observed on O-covered

polycrystalline Re [13] and Re(0001) [11] surfaces are also attributed to the formation of

ReO.

When the Re(12$\overline{3}$1) surface is exposed to 300L O$_2$ at 1000K, the Re4f$_{7/2}$ spectrum

changes drastically (see Fig. 4.6(b)); not only the ReO component becomes dominant

among surface peaks, but also an extra peak with SCLS of 1.68 eV emerges. This new

peak is attributed to the formation of a new surface oxide species Re_2O_3 [13]. By comparing the Re4f$_{7/2}$ spectra in Fig. 4.6(a) and (b), it is clear that the surface oxygen concentration upon adsorption at high temperature is larger than upon room temperature adsorption, which may be the key factor to cause the morphological change.

4.4 Discussion

Faceting is believed to be thermodynamically driven by the anisotropy of surface free energy but limited by kinetic factors such as nucleation and diffusion [14, 15]. When surfaces are covered by thin layers of chemisorbed molecules/atoms, not only do their surface free energies decrease due to the energy release from the chemical binding process, but also the anisotropy of the surface free energy changes. This originates from different adsorbate binding energy on inequivalent surfaces, associated with variations in bonding geometry. Apparently, the adsorption coverage (cm^{-2}) of available molecules/atoms and their chemical states are important in determining the surface energy anisotropy and the morphology of the faceted surface. For the O/Re($12\bar{3}1$) surface, we have demonstrated that the morphology of the faceted surface upon annealing in vacuum at T>700K evolves as the initial oxygen coverage at 300K increases [1]. In this process, the atomically rough ($11\bar{2}1$) surface always appears as a facet although it occupies less surface area when the oxygen initial coverage increases. An important characteristic of the ($11\bar{2}1$) facet is that it has the smallest tilt angle (12.0°) with respect to the ($12\bar{3}1$) substrate among all the facets observed. So for other facets that have tilt angles higher than 12.0° to replace ($11\bar{2}1$), they must not only have a lower surface free

energy than $(11\overline{2}1)$, but the energy must be low enough to compensate the higher surface area creation.

When the surface is exposed to oxygen at 300K, the maximum coverage of available oxygen atoms is limited by the density of adsorption sites on the planar $Re(12\overline{3}1)$ surface. Here we neglect the possibility of oxygen diffusing into the bulk because the exposure is moderate (< 360L). To explore possible morphological changes beyond this limit, one can anneal the $Re(12\overline{3}1)$ surface in an oxygen atmosphere so that some facets may become energetically unfavorable and undergo further faceting; our results show that $(11\overline{2}1)$ is such a facet. Upon dosing oxygen at high substrate temperatures, the total concentration of adsorbed oxygen atoms can exceed 1ML, and is controlled by both the total oxygen exposure and the substrate temperature; the latter affects the balance of oxygen adsorption, oxidation and desorption. The fact that the $(11\overline{2}1)$ facet disappears at 800-1000K and reemerges at ~1200K (Fig. 4.5) gives strong evidence that the instability of $(11\overline{2}1)$ is induced by adsorbed oxygen atoms exceeding some critical concentration.

Since the main morphological difference between the faceted surfaces prepared by dosing oxygen at different temperatures is whether $(11\overline{2}1)$ or $(10\overline{1}1)$ appears, we first focus the discussion on how their surface energies can be affected by oxygen adsorption. Using density functional theory (DFT) calculations, we find the surface energies of clean $(10\overline{1}1)$ and $(11\overline{2}1)$ are very close: $\gamma^{clean}_{(10\overline{1}1)} = 2.13\times10^{15}$ eV·cm^{-2} and $\gamma^{clean}_{(11\overline{2}1)} = 2.20\times10^{15}$ eV·cm^{-2}. The calculated energies are in good agreement with the experimental value of the average surface energy for Re surfaces, which is about 2.3×10^{15} eV·cm^{-2} [16, 17]. However, since the tilt angle of $(10\overline{1}1)$ with respect to $(12\overline{3}1)$ is 41.7°, much higher

than that of $(11\bar{2}1)$ $(12.0°)$, the surface energy per projected unit area on $(12\bar{3}1)$ for

clean $(10\bar{1}1)$ is much larger than that for clean $(11\bar{2}1)$. The surface energy difference

$\Delta\gamma_1$ due to this tilt angle effect can be estimated as

$$\Delta\gamma_1 = \frac{\gamma_{(10\bar{1}1)}^{clean}}{\cos 41.7°} - \frac{\gamma_{(11\bar{2}1)}^{clean}}{\cos 12.0°} = 0.60\times 10^{15}\,eV\cdot cm^{-2}. \qquad (4.1)$$

When both $(11\bar{2}1)$ and $(10\bar{1}1)$ are covered by low oxygen concentrations, $(11\bar{2}1)$ is

still favored against $(10\bar{1}1)$. Figure 4.7 shows oxygen binding energies on $Re(11\bar{2}1)$,

$Re(10\bar{1}1)$ and $Re(01\bar{1}0)$ for different oxygen concentrations per projected unit area on

$(12\bar{3}1)$ based on our DFT calculations. For a given oxygen concentration, a higher

oxygen binding energy on a facet helps reduce its surface free energy more. Clearly in

Fig. 4.7 even when the oxygen concentration is as high as $\sim 1\times 10^{15}$ cm^{-2}, the approximate

limit of oxygen concentration imposed by room temperature exposure to $Re(12\bar{3}1)$, the

O-Re binding energy difference for $Re(10\bar{1}1)$ and $Re(11\bar{2}1)$ is only about $0.2eV\cdot atom^{-1}$,

not enough to offset the initial surface energy advantage of $Re(11\bar{2}1)$. However, when

oxygen concentration is further increased by formation of surface oxides at higher sample

temperature, the O-Re binding energy difference for $Re(10\bar{1}1)$ and $Re(11\bar{2}1)$ may

increase and eventually cause $Re(10\bar{1}1)$ to be more favorable. In Fig. 4.7, when the

oxygen concentration is about 2×10^{15} cm^{-2}, the O-Re binding energy difference for

$Re(10\bar{1}1)$ and $Re(11\bar{2}1)$ is increased to $0.5eV\cdot atom^{-1}$. Therefore, the binding energy

difference per projected unit area on $(12\bar{3}1)$ is 1×10^{15} $eV\cdot cm^{-2}$, which is more than

enough to overcome the initial surface energy advantage of $Re(11\bar{2}1)$ and to trigger the

formation of $(10\bar{1}1)$ facets. Although the above discussion is confined to the T=0 K

limit and does not include the effects of background oxygen pressure and substrate
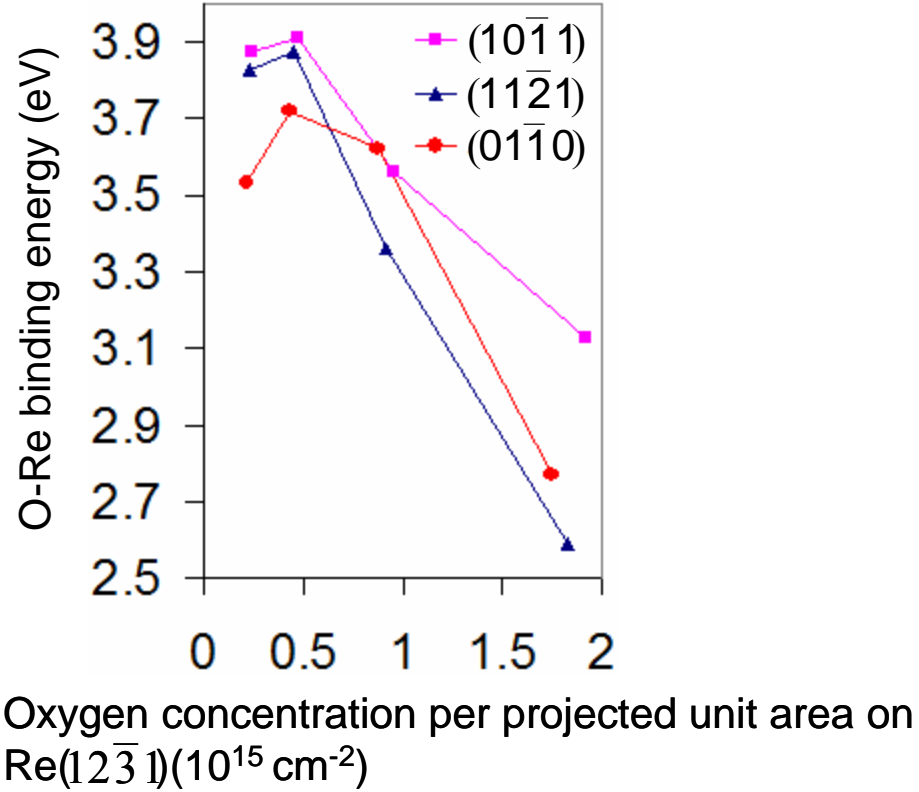
Fig. 4.7. Oxygen binding energies on Re($11\bar{2}1$), ($10\bar{1}1$) and ($01\bar{1}0$) as functions of oxygen concentration per projected unit area on ($12\bar{3}1$). The O-Re binding energies are referenced to gas phase O_2.

temperature on surface free energy, it already shows the importance of oxygen concentration in determining the surface morphology of faceted Re($12\bar{3}1$).

When the ($11\bar{2}1$) facet is replaced by the ($10\bar{1}1$) facet, the relative surface areas occupied by the other three remaining facets must also change to retain the macroscopic orientation of the Re($12\bar{3}1$) surface. Here we illustrate qualitatively that even after considering energetic contributions from the remaining facets, the removal of ($11\bar{2}1$) still does not occur at low oxygen concentrations. Because among the three remaining facets, ($01\bar{1}0$) has both the most close-packed surface structure and the smallest tilt angle (22.1°) to ($12\bar{3}1$), we neglect the ($10\bar{1}0$) and ($01\bar{1}1$) facets and focus on the effect of ($01\bar{1}0$). We do this by comparing the surface energies of a ridge formed by ($11\bar{2}1$) and

$(01\bar{1}0)$ (type I) with a ridge formed by $(10\bar{1}1)$ and $(01\bar{1}0)$ (type II). The cross sections of these two types of ridges are shown in Fig. 4.8, and the structural transition from the first to the second type of ridge can be regarded as follows: 31% of the projected area on $(12\bar{3}1)$ that is originally occupied by $(11\bar{2}1)$ gets replaced by $(10\bar{1}1)$, 35% of the projected area on $(12\bar{3}1)$ that is also originally occupied by $(11\bar{2}1)$ gets replaced by
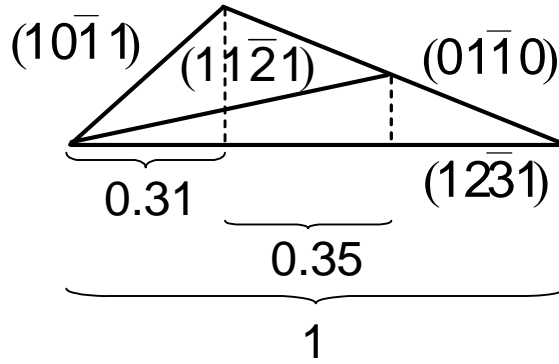
Fig. 4.8. Cross sections of ridges formed by $(11\bar{2}1)$ and $(01\bar{1}0)$ as well as by $(10\bar{1}1)$ and $(01\bar{1}0)$.

$(01\bar{1}0)$, and the remaining 34% of the projected area on $(12\bar{3}1)$ that is originally occupied by $(01\bar{1}0)$ is intact. The surface energy of clean $(01\bar{1}0)$ is $\gamma_{(01\bar{1}0)}^{clean} = 1.83 \times 10^{15}$ eV·cm^{-2} from our DFT calculations, so the surface energy difference $\Delta\gamma_2$ per projected unit area on $(12\bar{3}1)$ between clean $(01\bar{1}0)$ and $(11\bar{2}1)$ due to the tilt angle effect can be estimated as

$$\Delta\gamma_2 = \frac{\gamma_{(01\bar{1}0)}^{clean}}{\cos 22.1^\circ} - \frac{\gamma_{(11\bar{2}1)}^{clean}}{\cos 12.0^\circ} = -0.27 \times 10^{15} \, eV \cdot cm^{-2}. \tag{4.2}$$

When the surface is clean, the energy difference per projected unit area on $(12\bar{3}1)$ between type II and type I ridges is

$$\Delta E = 0.31\Delta\gamma_1 + 0.35\Delta\gamma_2 = 0.09 \times 10^{15} \, eV \cdot cm^{-2} > 0. \tag{4.3}$$

Therefore, a type I ridge formed by $(11\bar{2}1)$ and $(01\bar{1}0)$ is favored against a type II ridge formed by $(10\bar{1}1)$ and $(01\bar{1}0)$ if faceting ever occurs on the clean surface. This situation does not change when the surface is covered by low oxygen concentrations ($<0.5\times10^{15}$cm^{-2}) because ΔE remains positive due to the following reasons: $\Delta\gamma_1$ almost does not change because the O-Re binding energies on $(10\bar{1}1)$ and $(11\bar{2}1)$ are comparable while $\Delta\gamma_2$ increases because O-Re binding energy on $(01\bar{1}0)$ is much less than that on $(11\bar{2}1)$ at low oxygen concentrations (see Fig. 4.7). When the oxygen concentration per projected unit area on $(12\bar{3}1)$ is about 1×10^{15} cm^{-2}, the O-Re binding energies on $(01\bar{1}0)$ and $(10\bar{1}1)$ both become ~0.2 eV·atom^{-1} more than that on $(11\bar{2}1)$, so $\Delta\gamma_1$ and $\Delta\gamma_2$ are reduced to 0.4×10^{15} eV·cm^{-2} and -0.47×10^{15} eV·cm^{-2}, respectively. If we put the new values of $\Delta\gamma_1$ and $\Delta\gamma_2$ into Eq. (4.3), the energy difference per projected unit area on $(12\bar{3}1)$ between type II and type I ridges is now negative ($\Delta E = -0.04\times10^{15}$ eV·cm^{-2}) and is able to trigger the structural transition of the ridge from type I to type II. Considering the uncertainties in the O-Re binding energies and the fact that 1×10^{15} cm^{-2} is only a rough estimation of the saturation oxygen coverage on Re$(12\bar{3}1)$ at 300K, the small total energy gain ($\sim0.04\times10^{15}$ eV·cm^{-2}) from the structural transition of the ridge suggests that the oxygen saturation coverage on Re$(12\bar{3}1)$ at 300K is close to the critical oxygen concentration necessary for complete removal of the $(11\bar{2}1)$ facet. When the oxygen concentration per projected unit area on $(12\bar{3}1)$ is increased further to $\sim2\times10^{15}$ cm^{-2}, both the $(01\bar{1}0)$ and $(10\bar{1}1)$ facets become energetically favorable against the $(11\bar{2}1)$ facet, which is consistent with the experimental observation that the $(11\bar{2}1)$ facet disappears at high oxygen concentrations.

When the Re(12$\bar{3}$1) surface is exposed to 300L O_2 at 1000K(see Fig. 4.6(b)), the HRSXPS data show the formation of ReO and Re_2O_3 but no other Re oxides with higher oxidation states such as ReO_3 and Re_2O_7,. Since both ReO_3 and Re_2O_7 are volatile at 1000K, one should consider the possibility that the new faceted surface morphology is due mainly to surface etching by oxygen; for various reasons we believe this is not the case. Jacobson and colleagues studied the Re/O interactions at elevated temperatures in high pressure O/Ar mixtures and found that the Re weight loss due to oxidation at 1300K with an oxygen partial pressure 0.2 Torr is about 0.025mg·cm^{-2}·min^{-1} [18]. In our study, the average depth of the trench formed by (01$\bar{1}$0) and (11$\bar{2}$1) is $h \approx 40\text{Å}$ after the Re(12$\bar{3}$1) surface is heated at 1200K in oxygen (3×10^{-7} Torr) for 20min; if removal of ReO_x is the cause, the etching rate could be estimated as $\rho h/2t = 2.1×10^{-4}$ mg·cm^{-2}·min^{-1}, where ρ is the bulk density of Re and t is the heating time. Since the oxygen pressure used in our study is about 6 orders smaller than that in Jacobson's study, and our maximum temperature is 100K less than Jacobson's, it is unlikely that the assumed etching rate is only 2 orders smaller; the morphological change upon oxygen exposure at high temperature is attributed to surface diffusion of Re rather than etching by sublimation of ReO_x.

4.5 Conclusion

The surface morphology is very complex in oxygen-induced nano-faceting of Re(12$\bar{3}$1): five different facets with orientations of (11$\bar{2}$1), (01$\bar{1}$0), (10$\bar{1}$0), (01$\bar{1}$1), and (10$\bar{1}$1) are observed under different conditions. Only the first four facets appear when faceting is induced by saturation adsorption of oxygen ($\theta = 1\text{ML}$) at room temperature followed by annealing at T>700K. However, unlike (01$\bar{1}$0), (10$\bar{1}$0) and

(01 $\bar{1}$ 1), (11 $\bar{2}$ 1) becomes unstable when Re(12 $\bar{3}$ 1) is exposed to oxygen (120-360L) at 800-1000K. Evidence of ReO and Re_2O_3 formation is found in this temperature region, which is believed to further increase the surface energy anisotropy and lead to the replacement of (11 $\bar{2}$ 1) by the fifth facet (10 $\bar{1}$ 1). The (11 $\bar{2}$ 1) facet reemerges when Re(12 $\bar{3}$ 1) is exposed to oxygen at 1200K and is attributed to reduced oxygen coverage at this temperature. Surface etching by oxidation under our experimental conditions does not appear to play a major role in determining the final surface morphology. Our DFT calculations reveal the importance of adsorbate coverage in determining the surface morphology by affecting the anisotropy of surface free energy.

4.6 Acknowledgement

4.7 References:

[1]   H. Wang, W. Chen and T. E. Madey, Phys. Rev. B **74** (2006) 205426.

[2]   A. S. Y. Chan, W. Chen, H. Wang, J. E. Rowe and T. E. Madey, J. Phys. Chem. B **108** (2004) 14643.

[3]   T. E. Madey, Surf. Sci. **33** (1972) 355.

[4]   P. Thiry, P. A. Bennett, S. D. Kevan, W. A. Royer, E. E. Chaban, J. E. Rowe and N. V. Smith, Nucl. Instrum. Methods Phys. Res. Sect. A **222** (1984) 85.

[5]   M. D. Segall, P. L. D. Lindan, M. J. Probert, C. J. Pickard, P. J. Hasnip, S. J. Clark and M. C. Payne, J. Phys.: Condens. Matter **14** (2002) 2717.

[6]   D. Vanderbilt, Phys. Rev. B **41** (1990) 7892.

[7]   J. P. Perdew, K. Burke and M. Ernzerhof, Phys. Rev. Lett. **77** (1996) 3865.

[8]   P. Kaghazchi, T. Jacob, H. Wang, W.Chen and T. E. Madey, in preparation.

[9]   H. J. Monkhorst and J. D. Pack, Phys. Rev. B **13** (1976) 5188.

[10]   A. S. Y. Chan, G. K. Wertheim, H. Wang, M. D. Ulrich, J. E. Rowe and T. E. Madey, Phys. Rev. B **72** (2005) 035442.

[11]   R. Ducros and J. Fusy, J. Electron Spectrosc. Relat. Phenom. **42** (1987) 305.

[12]   W. T. Tysoe, F. Zaera and G. A. Somorjai, Surf. Sci. **200** (1988) 1.

[13]   C. Morant, L. Galán and J. M. Sanz, Anal. Chim. Acta **297** (1994) 179.

[14]   Q. Chen and N. V. Richardson, Prog. Surf. Sci. **73** (2003) 59.

[15]   C. Herring, Phys. Rev. **82** (1951) 87.

[16]   W. R. Tyson and W. A. Miller, Surf. Sci. **62** (1977) 267.

[17]   F. R. deBoer, R. Boom, W. C. M. Mattens, A. R. Miedema and A. K. Niessen, *Cohesion in Metals*, North-Holland, Amsterdam, (1988) pp 758.

[18]   N. S. Jacobson, D. J. Myers, D. Zhu and D. L. Humphrey, Oxid. Met. **55** (2001) 471.

[19]   H. Wang, A. S. Y. Chan, P. Kaghazchi, T. Jacob and T. E. Madey, ACS Nano **1** (2007) 449.

Chapter 5   Oxygen-induced morphological instability of Re($11\overline{2}1$)

5.1. Introduction

To explain how catalysts work in the atomic scale is one of the ultimate goals of surface science research. One important step in this endeavor is to study how various gas molecules react with the single crystal metal surfaces that are used as the simplest model systems for real catalysts. However, real catalysts, usually in the form of supported particles in the scale between nanometers to microns, do not contain just one single crystalline surface but many faces. A good approach then is to study adsorbate induced faceting of metal surfaces and use the faceted surfaces as better model systems to study catalysis. Examples include structure sensitivity found in ammonia decomposition [1] and CO oxidation [2] on planar and faceted Ir(210) surfaces.

Rhenium is an important component of many catalysts [3-6], so the first step toward understanding the reactivity of model Re surfaces is to investigate how the surface morphology changes in the presence of adsorbates. In Chapters 3 and 4, we have reported that the adsorption of oxygen on an atomically rough Re($12\overline{3}1$) surface can induce formation of various facets upon annealing. The morphology of the faceted surface depends on the oxygen coverage and adsorption temperature. Among all the facets that are observed on Re($12\overline{3}1$), ($11\overline{2}1$) is unique since it persists when oxygen concentration is low but disappears at high oxygen concentration [7, 8]. An interesting question is whether the metastability of the ($11\overline{2}1$) surface remains if we start with a ($11\overline{2}1$) surface. Also the ($11\overline{2}1$) surface has higher symmetry than ($12\overline{3}1$), so the faceted structures that

form will also have higher symmetry than those forming on $(12\bar{3}1)$, which may simplify the interpretation of the facet orientations.

In this chapter we report oxygen-induced faceting of $Re(11\bar{2}1)$ combining several experimental techniques such as low energy electron diffraction (LEED) and scanning tunneling microscopy (STM) as well as density functional theory (DFT) calculations. The results suggest that the anisotropy of surface free energies between $(11\bar{2}1)$ and the facets changes as the oxygen concentration increases.

5.2. Experimental and computational procedures

The experimental procedure is similar to that described in Chapter 3. A $Re(11\bar{2}1)$ single crystal, 99.99% pure and aligned within 0.5° of the $(11\bar{2}1)$ orientation, is used in the study; it is ~8mm in diameter and ~1mm thick. A hard-sphere model of $Re(11\bar{2}1)$ and its position in the stereographic projection plot are given in Fig. 5.1. Oxygen is adsorbed on $Re(11\bar{2}1)$ either at room temperature or at elevated temperatures. All the LEED and STM experiments are performed after the oxygen-covered surface is cooled to room temperature.

The O-Re binding energies on several Re surfaces are calculated by density functional theory (DFT) using the CASTEP code [9] with Vanderbilt-type ultrasoft pseudopotentials [10] and the generalized gradient approximation (GGA) of the exchange-correlation functional [11]. The calculations are performed by Jacob and Kaghazchi [12]. $Re(01\bar{1}0)$, $(01\bar{1}1)$and $(11\bar{2}1)$ surfaces are represented by 11-layer, 14-layer and 19-layer slabs with ~13 Å vacuum, respectively. For each system, the bottom four layers are fixed at the calculated bulk-crystal structure, and the
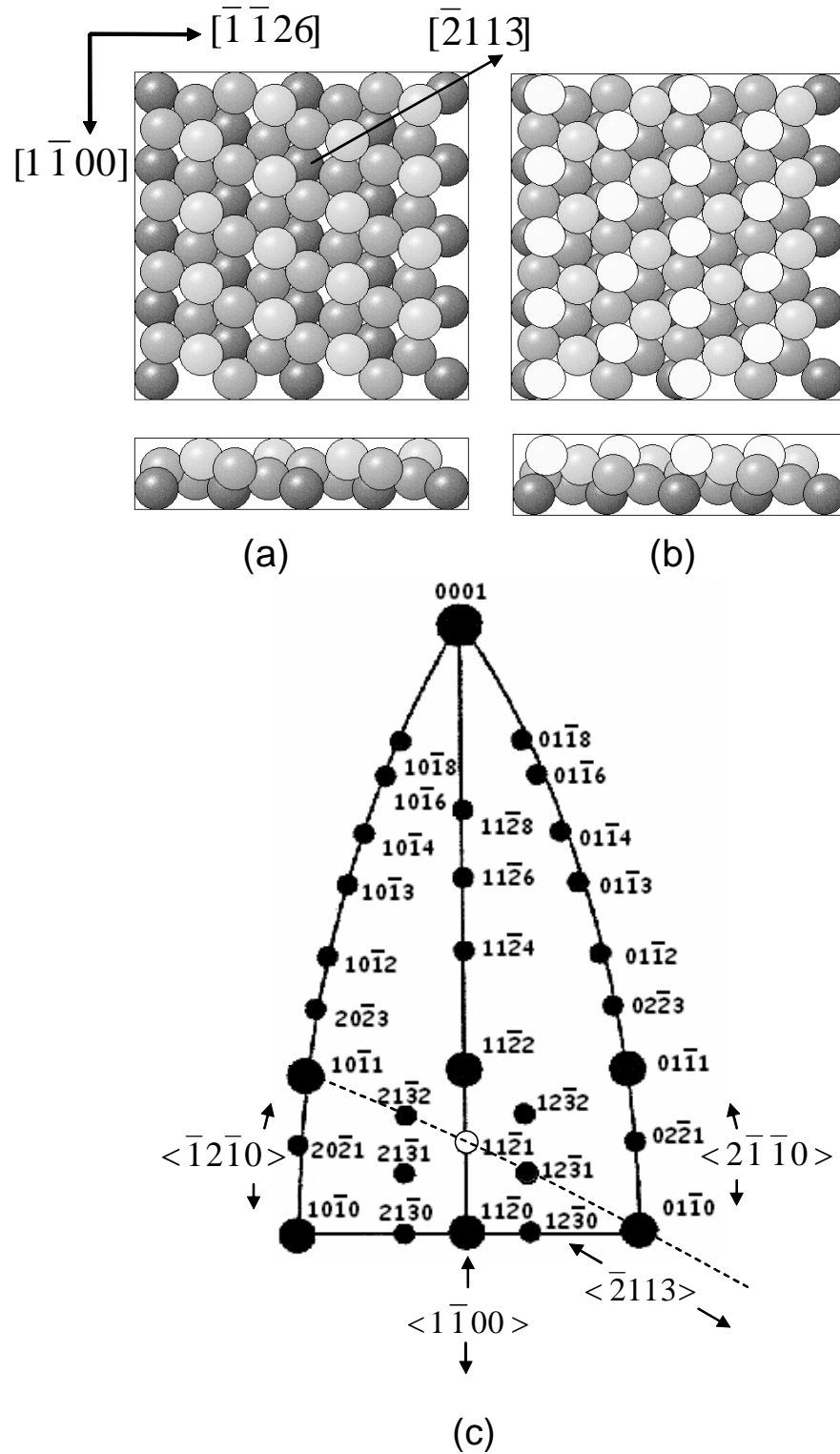
Fig. 5.1. Hard-sphere models of the two different terminations of bulk truncated Re($11\bar{2}1$) shown in (a) and (b). (c) is a stereographic projection plot of the hcp lattice on ($11\bar{2}0$). The ($11\bar{2}1$) surface is labeled by a hollow circle. The $<1\bar{1}00>$, $<2\bar{1}\bar{1}0>$, $<\bar{1}2\bar{1}0>$ and $<\bar{2}113>$ crystallographic zones are also labeled in (c).

remaining Re atoms and the adsorbates are allowed to relax freely. For the oxygen-adsorbed system, the cutoff energy is converged to 380 eV, and the Brillouin zone sampling of the (1×1) unit cell is converted to 5×8, 4×8 and 4×4 Monkhorst-Pack meshes for Re($01\bar{1}0$), ($01\bar{1}1$), and ($11\bar{2}1$), respectively [13].

If the total surface area of a slab is denoted as A, the Gibbs free surface energy per unit area as a function of temperature T and oxygen pressure p is

$$\gamma(T,p) = [G_{slab}(T,p,N_{Re},N_O) - N_{Re}\mu_{Re} - N_O\mu_O(T,p)]/A, \qquad (5.1)$$

where G_{slab} is the total Gibbs free energy of the slab, N_{Re} and N_O are the numbers of Re and O atoms in the slab, respectively, and μ_{Re} and $\mu_O(T, \text{p})$ are the chemical potentials of Re-bulk and gaseous oxygen, respectively. G_{slab} is determined from the total internal energy of the slab with vibrational contributions neglected [14]. The temperature and pressure dependence of γ dominantly comes from $\mu_O(T, \text{p})$, which is given by

$$\mu_O(T,p) = [E_{O_2} + \bar{\mu}_{O_2}(T,p^0) + k_B T \ln(p/p^0)]/2. \qquad (5.2)$$

Here E_{O_2} is the DFT-calculated total energy of an isolated O_2 molecule and $\bar{\mu}_{O_2}(T,p^0)$ is the standard chemical potential of oxygen gas at $p^0 = 1$ atm with the value taken from the JANAF thermochemical tables [15].

5.3. Results and Discussion

5.3.1. LEED study

A. Oxygen adsorption at room temperature followed by annealing

No reconstruction is found on a a clean Re($11\bar{2}1$) surface after being annealed at elevated temperatures up to 2000K; a (1×1) pattern is always observed in LEED as shown in Fig. 5.2(a). When the incident electron beam energy E_e increases, all the LEED
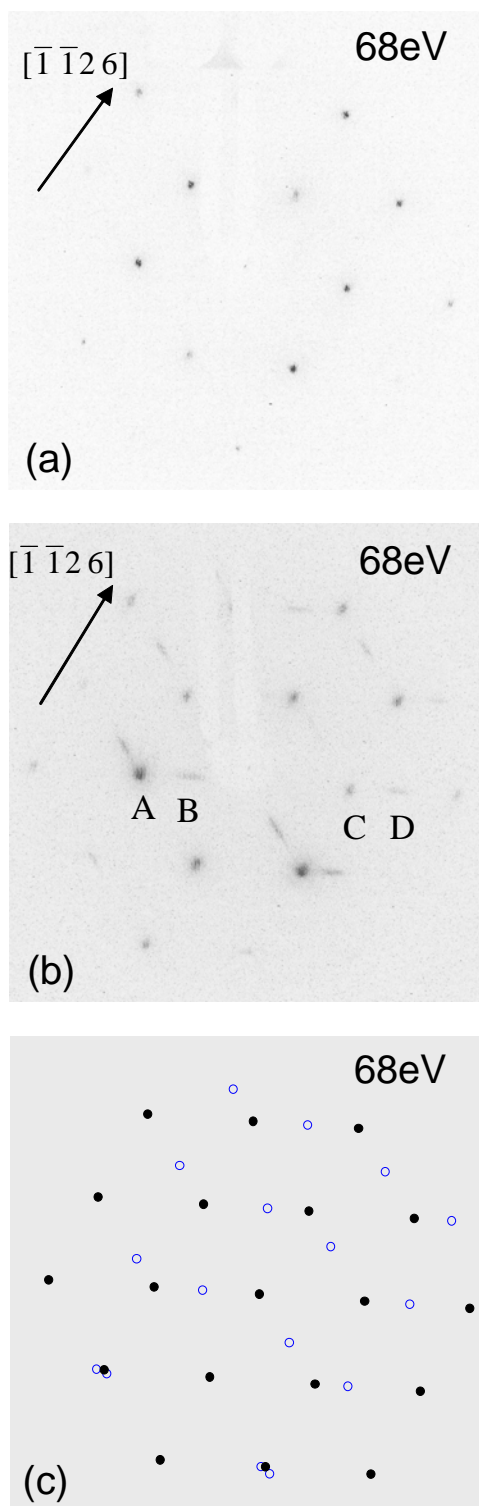
Fig. 5.2. LEED patterns from a Re($11\bar{2}1$) surface when it is (a) clean and (b) exposed to 10L O$_2$ at 300K followed by annealing at 1000K for 2 min. (c) is a kinematical simulation of (b) based on 2D lattices of ($11\bar{2}1$), ($01\bar{1}0$) and ($10\bar{1}0$), in which the solid circles are beams from ($11\bar{2}1$) and the hollow circles are beams from ($01\bar{1}0$) and ($10\bar{1}0$).

spots converge to the center of the screen, indicating the surface is planar. When the surface is exposed to oxygen at 300K, reconstruction is still not observed in LEED and the pattern looks almost same as Fig. 5.2(a) except for a slight increase of the background signal associated with random adsorption of oxygen.

New features appear in the LEED pattern only after the $Re(11\bar{2}1)$ surface is exposed to >3L oxygen and annealed at T>700K (see Fig. 5.2(b)). These new features move toward two positions that are located outside the LEED screen when E_e increases, suggesting the formation of two facets that coexist with $(11\bar{2}1)$. The diffraction beams from the facets show an axis of symmetry along the $[\bar{1}\,\bar{1}2\,6]$ direction and imply that the two facets are symmetrical to each other with respect to the mirror plane of $(11\bar{2}1)$, which is not surprising since the faceted surface must maintain the symmetry of $(11\bar{2}1)$. Moreover, the diffraction beams from the facets are streaky, indicating that the facet size is small along one direction. It is impossible to identify the facet orientations on the basis of the specular beam positions because they are located outside of the LEED screen. However, a correlation is observed between the moving fashion of the facet beams and that of the planar beams when E_e increases, which can help identify the facet orientations. Because of the symmetry between the two facets, here we only show how to identify the orientation of one facet by analyzing the motions of some representative diffraction beams. In Fig. 5.2(b), four diffraction beams are labeled as A, B, C and D, among which A and C are from $(11\bar{2}1)$ while B and D are from the facet. When E_e changes, these four beams change positions but they always stay on a straight line along a fixed direction. On the basis of the Ewald construction of a LEED pattern [16], this observation indicates that the reciprocal rods corresponding to these four beams are located in the same plane

parallel to the incident electron beam otherwise A, B, C and D should fall on a smooth curve rather than a straight line. The normal vector of this plane is the crystallographic zone axis of $(11\bar{2}1)$ and the facet, which is also perpendicular to the AC direction. Because the LEED pattern from $(11\bar{2}1)$ resembles its lattice pattern in real space rotated by 90°, the zone axis can be identified as $[\bar{2}113]$ (see Fig. 5.1(a)). As shown in the stereographic projection plot in Fig. 5.1(c), among all the surfaces in the $<\bar{2}113>$ zone, $(01\bar{1}0)$ is the most plausible facet candidate because it is the most close-packed surface near $(11\bar{2}1)$. Fig. 5.2(c) shows a kinematical LEED simulation at the same E_e as in Fig. 5.2(b) and based on the 2-D lattices of $(01\bar{1}0)$ and its symmetrical counterpart $(10\bar{1}0)$. The positions of the diffraction spots in the simulated pattern are almost identical to those in Fig. 5.2(b); this resemblance retains for other values of E_e, indicating that indeed the facets are $(01\bar{1}0)$ and $(10\bar{1}0)$ and they are not reconstructed. When the partially faceted surface is annealed at ~1300K, the surface becomes planar again due to desorption of oxygen and the LEED pattern reverts to that seen in Fig. 5.2(a).

When oxygen exposure is increased to 60L, new subtle changes are found in the LEED pattern after the surface is annealed between 800-1100K. Figure 5.3(a) shows a LEED pattern taken from a surface exposed to 60L O_2 followed by annealing at 1000K for 2 min; it looks similar to the LEED pattern in Fig. 5.2(b) taken at the same E_e: diffraction beams from $(11\bar{2}1)$ coexist with those from $(01\bar{1}0)$ and $(10\bar{1}0)$ facets. However, if we focus on the four beams labeled as A-D in Fig. 5.3(a) that are located in similar positions as the A-D beams in Fig. 5.2(b), they are not on a straight line anymore. This deviation from a straight line is also observed for other values of E_e, indicating that the surface morphology must have changed from $(11\bar{2}1)$ coexisting with $(01\bar{1}0)$ and
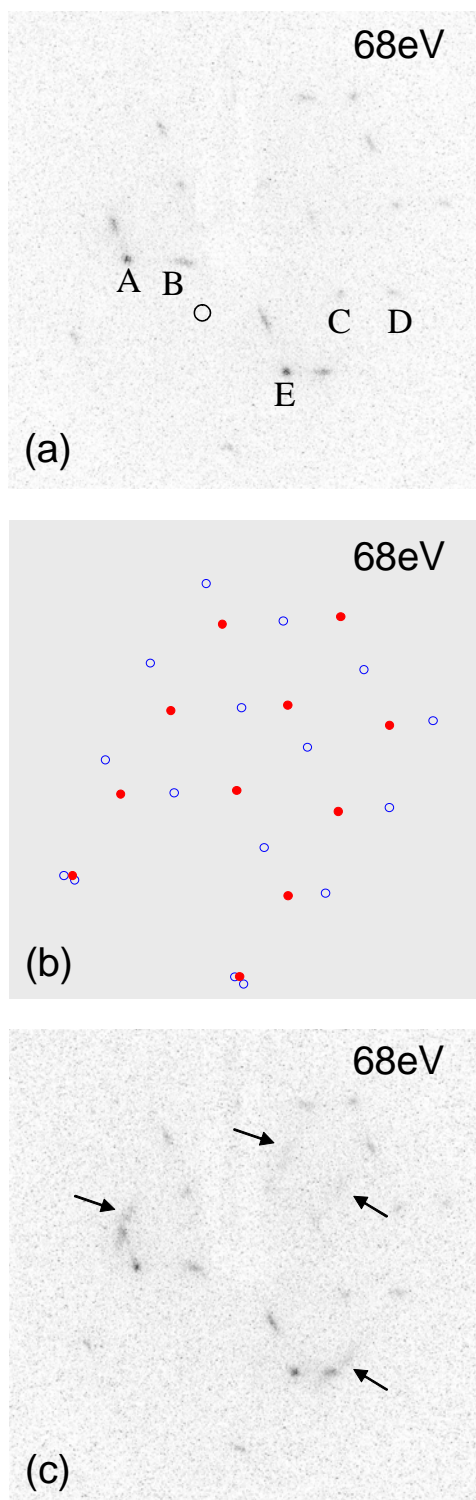
Fig. 5.3. LEED patterns of Re($11\bar{2}1$) taken after it is exposed to (a) 60L and (c)120L O_2 at 300K followed by annealing at 1000K for 2 min. (b) is a kinematical simulation of (a) based on 2D lattices of ($33\bar{6}4$), ($01\bar{1}0$) and ($10\bar{1}0$), in which the solid circles are beams from ($33\bar{6}4$) and the hollow circles are beams from ($01\bar{1}0$) and ($10\bar{1}0$). See text for other labels.

($10\bar{1}0$) facets. By observing how the diffraction beams move when E_e changes, we know the ($01\bar{1}0$) and ($10\bar{1}0$) facets are intact while the beams such as A and C in Fig. 5.3(a) are not from ($11\bar{2}1$) but from a new facet. The specular beam of the new facet has almost zero intensity for different values of E_e, but its position can still be approximately located on the basis of the following two observations: 1) the diffraction beams from the new facet retain the mirror symmetry along the [$\bar{1}\bar{1}26$] direction, thus the specular beam must be on the symmetry axis of the LEED pattern; 2) the A and E beams in Fig. 5.3(a) move toward each other when E_e increases, indicating the specular beam is also located on the line connecting these two beams. As labeled by a hollow circle in Fig. 5.3(a), the intersection point between the symmetry axis and the AE line is the specular beam position of the new facet, whose tilt angle with respect to ($11\bar{2}1$) is then determined to be ~6°. The diffraction beams from the new facet are similar to those from ($11\bar{2}1$) because the new facet is vicinal to ($11\bar{2}1$) and located in the $<1\bar{1}00>$ zone. Two possible candidates for the new facet are ($22\bar{4}3$) and ($33\bar{6}4$), with tilt angles of 7.7° and 5.2°, respectively. However, kinematical simulations of the LEED pattern based on 2-D lattices of ($22\bar{4}3$) and ($33\bar{6}4$) reveal that only the latter gives a good match to the experimental LEED pattern. Figure 5.3(b) shows a kinematical simulation of Fig. 5.3(a) based on 2D lattices of ($01\bar{1}0$), ($10\bar{1}0$) and ($33\bar{6}4$); because ($33\bar{6}4$) can be regarded as a stepped ($11\bar{2}1$) surface with the terrace width equal to one unit size of ($11\bar{2}1$), among all the diffraction beams from ($33\bar{6}4$) only those close to the beam positions of ($11\bar{2}1$) can have enough intensity to be detected experimentally. As a result, only those diffraction beams from ($33\bar{6}4$) satisfying this criterion are shown in the simulation.

Further annealing the surface at 1200K, the LEED pattern reverts to that in Fig. 5.2(b) due to slight desorption of oxygen.

When Re($11\bar{2}1$) is exposed to 120L of oxygen followed by annealing at 800-1100K, the LEED pattern shown in Fig. 5.3(c) looks similar to Fig. 5.3(b) except for some new faint streaks as marked by arrows in Fig. 5.3(c). These streaks are from new facets because they do not converge to the specular beam positions of ($01\bar{1}0$), ($10\bar{1}0$) and ($33\bar{6}4$) when E_e increases. However, since the streaks are weak, it is difficult to identify the orientations of the new facets. In the following section, we show that the unknown facets become better developed and give stronger LEED beam intensity when Re($11\bar{2}1$) is exposed to oxygen at high temperature; the facet orientations can then be determined as ($01\bar{1}1$) and ($10\bar{1}1$).

B. Oxygen adsorption at high temperatures

The LEED results in the previous section show that the morphology of a faceted Re($11\bar{2}1$) surface depends on the initial oxygen exposure at 300K before annealing. However, with this facet preparation procedure, the maximum amount of oxygen is limited by the saturation coverage at 300K. In order to go beyond this coverage limit and explore the possibility of other facet formation, we dose oxygen with the Re($11\bar{2}1$) surface heated at high temperatures and then let the surface cool down to 300K before conducting LEED measurements. This new facet preparation procedure has been proved successful in our previous study of oxygen-induced faceting of Re($12\bar{3}1$) [17].

Figures 5.4(a)-(d) show LEED patterns taken after a Re($11\bar{2}1$) surface is exposed to different amounts of oxygen ranging from 10L to 120L at 1000K. When the oxygen exposure is 10L, the LEED pattern (Fig. 5.4(a)) looks similar to Fig. 5.2(b), showing the
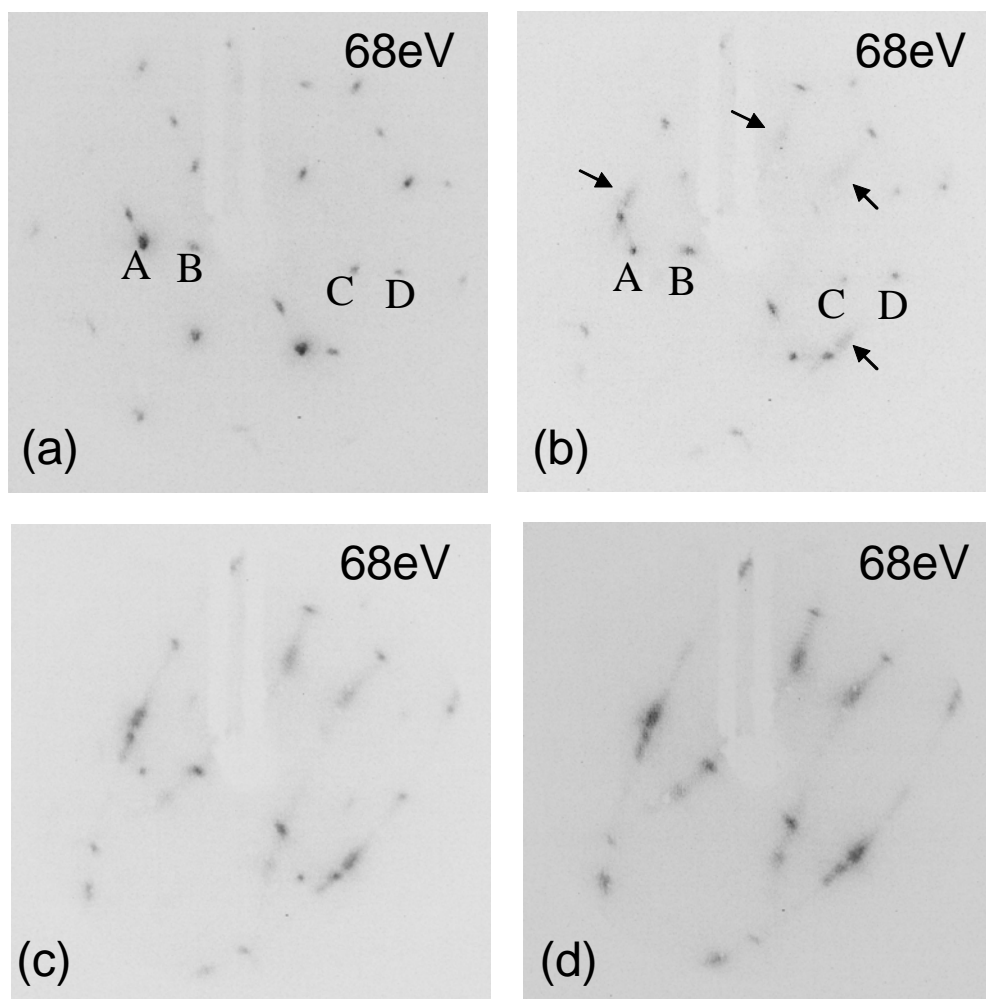
Fig. 5.4. LEED patterns taken after a Re($11\bar{2}1$) surface heated at 1000K is exposed to (a) 10L O_2 , (b) 30L O_2, (c) 60L O_2 and (d) 120L O_2.

($01\bar{1}0$) and ($10\bar{1}0$) facets coexisting with ($11\bar{2}1$). Since the Re crystal is kept at 1000K for 20min, much longer than the 2min annealing time used for Fig. 5.2(b), the diffraction beams from the facets in Fig. 5.4(a) are less streaky than those in Fig. 5.2(b), indicating that the facets size increases with longer annealing time. When the oxygen exposure is increased to 30L, the LEED pattern (Fig. 5.4(b)) evolves to look like Fig. 5.3(c): the surface is completely faceted with ($01\bar{1}0$), ($10\bar{1}0$), ($33\bar{6}4$) coexisting with two unknown facets (see streaks marked by arrows in Fig. 5.4(b)). With further increase of oxygen exposure to 60L, the LEED pattern in Fig. 5.4(c) looks similar to Fig. 5.4(b)

except that the beam intensity from $(33\bar{6}4)$ is weakened while the beam intensity from the two unknown is enhanced. In Fig. 5.4(d), when oxygen exposure is increased to 120L, the diffraction beams from $(33\bar{6}4)$ completely disappear and the surface is fully faceted with $(01\,\bar{1}\,0)$, $(10\,\bar{1}\,0)$ and the two unknown facets. Further increasing oxygen exposure to as high as 300L does not bring any new surface structures, since the corresponding LEED pattern in Fig. 5.5(a) is almost the same as in Fig. 5.4(d).
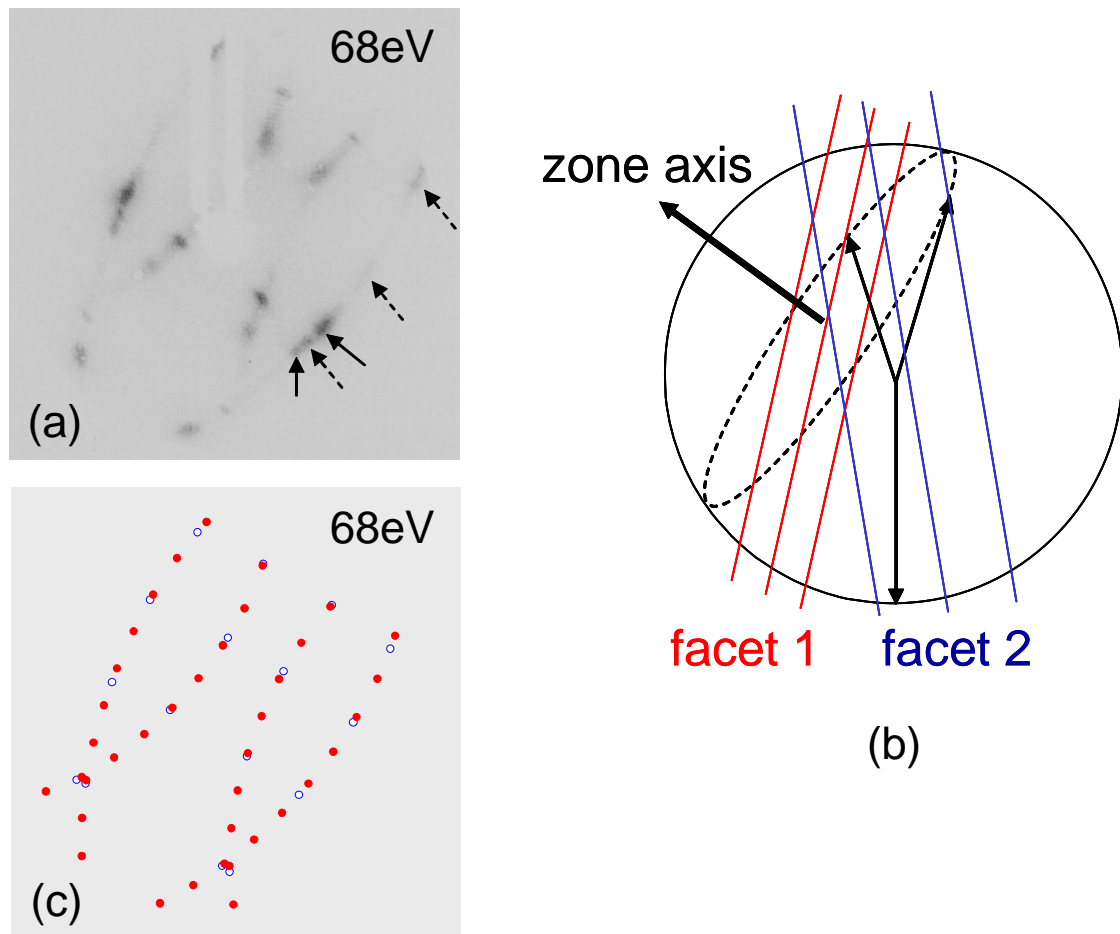
Fig. 5.5. (a) LEED patterns taken after a Re$(11\bar{2}1)$ surface heated at 1000K is exposed to 300L O$_2$. (b) An Ewald sphere construction showing the relationship between two facets. (c) is a kinematical simulation pattern of (a).

The diffraction beams from the two unknown facets are also symmetrical along the $[\bar{1}\,\bar{1}\,26]$ direction; moreover, they form smooth curves together with the beams from

($01\bar{1}0$) and ($10\bar{1}0$) for different E_es (see Fig. 5.5(a)). According to the Ewald sphere construction of a LEED pattern, beams on a smooth curve indicate that their corresponding reciprocal rods are located in the same plane (see Fig. 5.5(b)). The fact that the beams form a smooth curve instead of a straight line indicates the plane is not parallel to the incident electron beam. Because the reciprocal rods are perpendicular to their corresponding facets, the crystallographic zone axis of the facets is perpendicular to the plane of the reciprocal rods. Five beams on a smooth curve are labeled in Fig. 5.5(a), among which three are from ($01\bar{1}0$) and labeled by solid arrows and the other two are from one of the unknown facets and labeled by dashed arrows. The reciprocal rods corresponding to the three beams of ($01\bar{1}0$) are located in the ($2\bar{1}\bar{1}0$) plane, whose normal direction is [$2\bar{1}\bar{1}0$]. Therefore, one of the unknown facets must be in the $<2\bar{1}\bar{1}0>$ zone and the other must be in the $<\bar{1}2\bar{1}0>$ zone due to the mirror symmetry. As shown in the stereographic projection plot in Fig. 5.1(c), ($01\bar{1}1$) and ($10\bar{1}1$) are the only probable facet candidates because both are close-packed surface and may have low surface free energy; (0001) cannot be the facet orientation because two unknown facets are observed. Our previous study conducted under similar oxygen adsorption conditions on Re($12\bar{3}1$), a surface tilted 12.0° from ($11\bar{2}1$), found that ($01\bar{1}1$) and ($10\bar{1}1$) also appear as facets, so we propose that the new facets are ($01\bar{1}1$) and ($10\bar{1}1$) as well.

Kinematical simulations of the LEED pattern in Fig. 5.5(a) are performed on the basis of the 2-D lattices of ($01\bar{1}0$), ($10\bar{1}0$), ($01\bar{1}1$) and ($10\bar{1}1$) to confirm the facet orientations. However, a good match between the simulated and experimental LEED patterns can only be achieved by assuming that ($01\bar{1}1$) and ($10\bar{1}1$) are (2×1) reconstructed (see the simulated pattern in Fig. 5.5(c)); the reconstruction is along the

[1 $\bar{1}$ 00] direction (see details in Sec. 5.3.4 below). For example, the two beams labeled by solid arrows in Fig. 5.5(a) are the direct evidence of the (2×1) reconstruction because the distance between them is about half of the value from an unreconstructed (01 $\bar{1}$ 1) surface.

So far we have shown the morphology of a faceted Re(11$\bar{2}$1) surface depends on the oxygen coverage at 1000K. The effect of substrate temperature during oxygen adsorption is two-folds: first, the substrate temperature affects the kinetics of facet formation; second, the substrate temperature affects the balance of oxygen adsorption-desorption processes, which determines the oxygen coverage that in turn determines the facet morphology. As shown in Fig. 5.6(a), when the Re(11$\bar{2}$1) surface is exposed to 120L of oxygen at 700K, only diffuse features associated with (01 $\bar{1}$ 0) and (10 $\bar{1}$ 0) facets can be identified besides a few diffraction spots from the (1×1) structure of Re(11$\bar{2}$1). This suggests that the size of the facets that form at 700K is very small and the growth of the facets is controlled by kinetics. When the oxygen adsorption temperature is increased to 900K, even with a reduced oxygen exposure (60L), facets become better developed as evidence by sharper diffraction spots in Fig. 5.6(b). The surface also becomes completed faceted because all the diffraction spots of (11$\bar{2}$1) disappear. In Fig. 5.6(b) the diffraction beams from (01 $\bar{1}$ 0) (10 $\bar{1}$ 0), (01 $\bar{1}$ 1) and (10 $\bar{1}$ 1) form four smooth curves just like those in Fig. 5.5(a), however, there coexists another set of diffraction beams that converge to a spot labeled by a circle in Fig. 5.6(b). These diffraction spots cannot be from (33$\bar{6}$4) as in Fig. 5.4(b) and (c) because they form a rectangular pattern instead of a distorted hexagonal pattern and the facet tilt angle determined from the specular beam position is higher than that of (33$\bar{6}$4). The new found facet is metastable because it disappears with
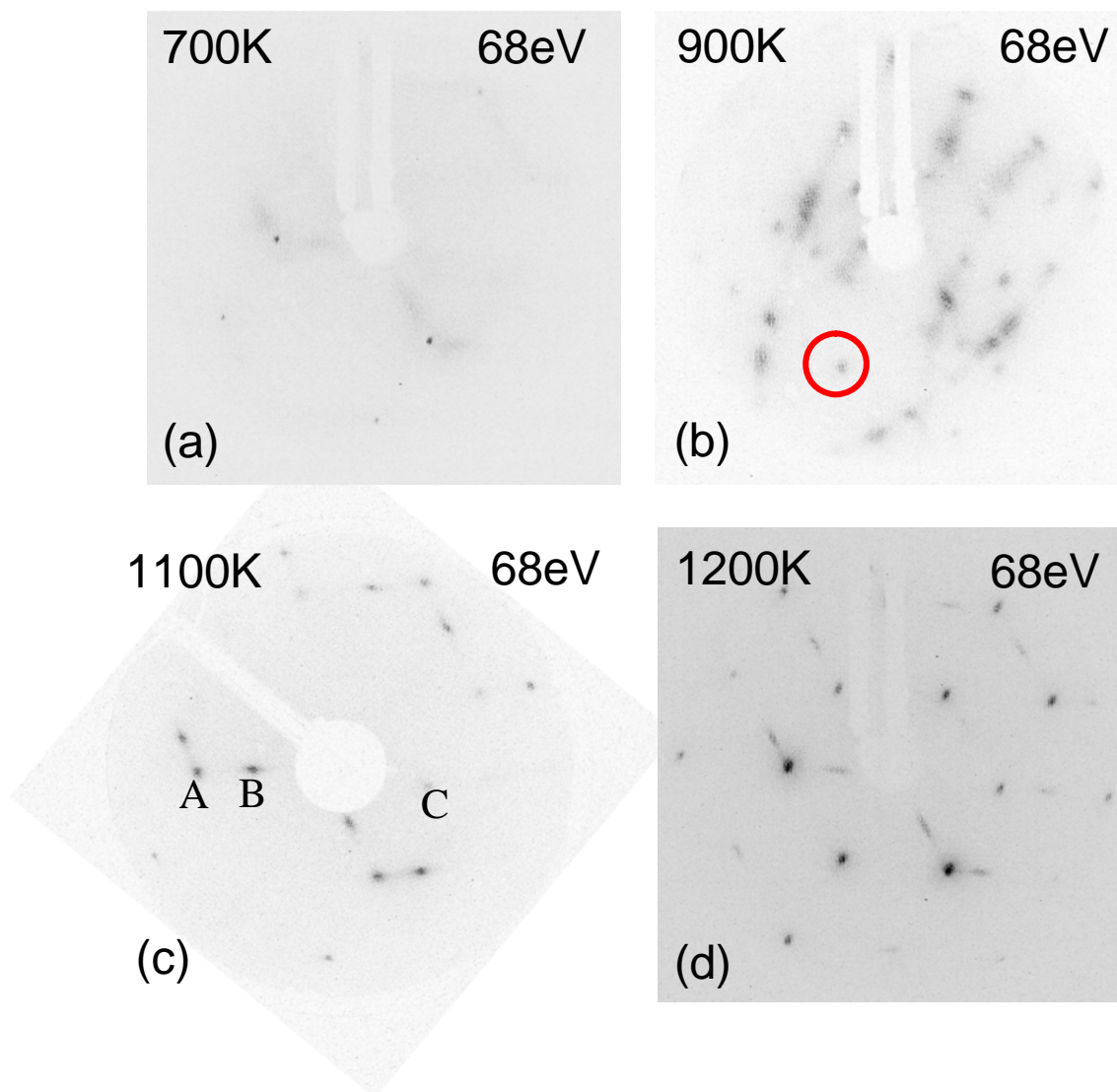
Fig. 5.6. LEED patterns of Re(11$\bar{2}$1) taken after it is exposed to 120L O$_2$ at different temperatures: (a) 700K, (b) 1000K, (c) 1100K and (d) 1200K.

further increasing of oxygen exposure; its orientation will be identified below. When the oxygen adsorption temperature is increased to 1100K, the (11$\bar{2}$1) surface is completely faceted with (01$\bar{1}$0) (10$\bar{1}$0) and (33$\bar{6}$4) (see Fig. 5.6(c)); note the diffraction beams labeled as A, B and C in Fig. 5.6(c) are not in a straight line, which is the signature used to distinguish between (33$\bar{6}$4) and (11$\bar{2}$1). When Re(11$\bar{2}$1) is exposed to 120L of O$_2$ at 1200K, the LEED pattern in Fig. 5.6(d) resembles Fig. 5.2(b) taken from a surface

prepared by dosing 10L at 300K followed by annealing at 1000K; the Re(11$\bar{2}$1) surface becomes partially faceted with (01$\bar{1}$0) and (10$\bar{1}$0) facets. The fact that the surface is not completely faceted indicates 1200K is a temperature too high for the surface to accumulate enough oxygen coverage for the formation of other facets.

To identify the orientation of the metastable facet observed upon oxygen adsorption at 900K, we first determine the tilt angle of the facet by using the LEED pattern from planar Re(11$\bar{2}$1) as a reference frame. Figure 5.7(a) shows a LEED pattern taken at E_e equal to 24eV from Re(11$\bar{2}$1) after being exposed to 60L O$_2$ at 900K, in which the rectangular pattern from the metastable facet is clearly recognizable. The specular beam of the metastable facet, labeled by a solid circle in Fig. 5.7(a), is located at the same position in the LEED screen as the (0$\bar{1}$) beam from planar Re(11$\bar{2}$1) when E_e is 30±5 eV (see Fig. 5.7(b)). On the basis of the reciprocal lattice of Re(11$\bar{2}$1) and the Ewald sphere construction of LEED patterns, the angle between the (0$\bar{1}$) beam and the incident beam is $28 \pm 3°$ for E_e equal to 30 ± 5eV. Therefore, the angle between the specular beam of the metastable facet and the incident beam is also $28 \pm 3°$; the tilt angle of the metastable facet with respect to Re(11$\bar{2}$1) is 14 ± 2 °.

Since the metastable facet must be on the $<1\bar{1}00>$ crystallographic axis due to the symmetry of the LEED pattern, the possible candidates of the facet is either (11$\bar{2}$2) or (11$\bar{2}$0), whose tilt angles to (11$\bar{2}$1) are 14.6° and 17.2°, respectively. However, after considering the spatial relationship between the metastable facet, (01$\bar{1}$0) and (10$\bar{1}$0) (see the approximate specular beam positions of (01$\bar{1}$0) and (10$\bar{1}$0) in Fig. 5.7(a)), (11$\bar{2}$2) must be the orientation of the metastable facet; the spatial relationship between (11$\bar{2}$2), (01$\bar{1}$0) and (10$\bar{1}$0) can be seen in the stereographic projection plot in Fig.

$(10\,\overline{1}\,0)$
specular beam

$(01\,\overline{1}\,0)$
specular beam

24eV

(a)

30eV

(b) $(0\,\overline{1})$

24eV

(c)
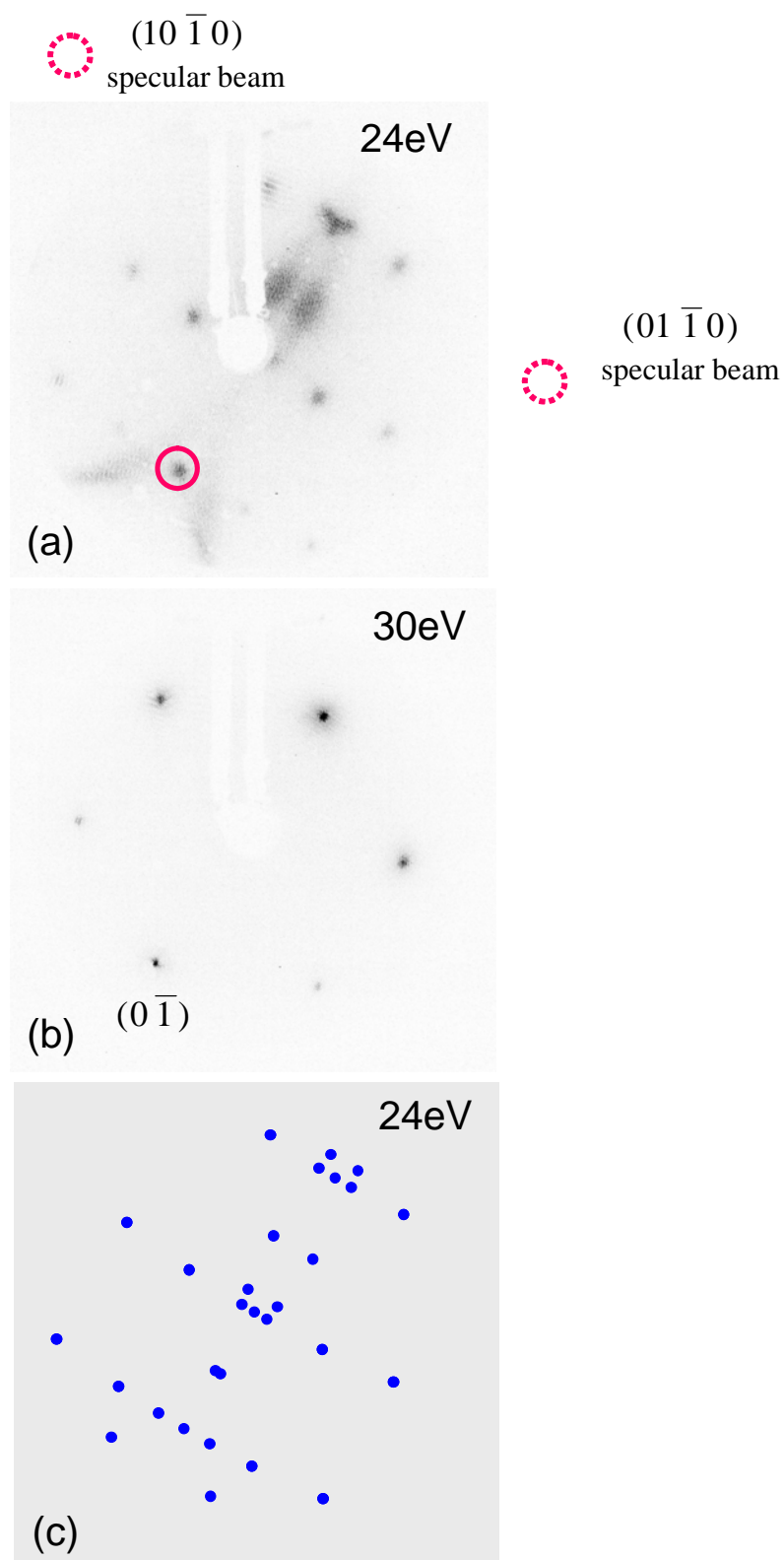
Fig. 5.7. (a) LEED pattern of Re($11\overline{2}1$) after being exposed to 60L O$_2$ at 900K; the solid circle labels the specular beam of ($11\overline{2}2$). (b) LEED pattern of planar Re($11\overline{2}1$) with the ($0\,\overline{1}$) beam labeled; (c) is a kinematical simulation of (a).

5.1(c). Figure 5.7(c) shows a kinematical simulation of the LEED pattern in Fig. 5.7(a) assuming the $(11\bar{2}2)$ facet is (2×1) reconstructed; the resemblance between Fig. 5.7(a) and (c) suggests that the orientation of the metastable facet is $(11\bar{2}2)$.

5.3.2. STM study

STM measurements are conducted to reveal the morphology of faceted $Re(11\bar{2}1)$ in real space and to confirm the LEED results. Here we focus on the morphology of the four stable facets: $(01\bar{1}0)$ $(10\bar{1}0)$, $(01\bar{1}1)$ and $(10\bar{1}1)$. Figure 5.8(a) is a typical STM image taken from a $Re(11\bar{2}1)$ surface exposed to 10L O_2 at 300K followed by annealing at 1000K, showing terraces separated by zigzag steps. The zigzag steps are actually made of $(01\bar{1}0)$ and $(10\bar{1}0)$ facets as shown in Fig. 5.8(b), a 3-D perspective view of the same STM image as Fig. 5.8(a). The orientation of the terraces is confirmed as $(11\bar{2}1)$ by atomic resolution STM image taken from one of the terraces (Fig. 5.8(c)), in which a squashed hexagonal pattern characteristic to $(11\bar{2}1)$ is clearly seen. The orientations of the two facets can be confirmed by measuring their tilt angles with respect to $(11\bar{2}1)$ and the angle of the intersection lines between the facets. The inset in Fig. 5.8(a) shows the cross section profile along the solid line marked in Fig. 5.8(a), in which the slope of the tilted line segment AB gives a tilt angle of $32\pm2°,$ agreeing well with the ideal tilt angle $(34.2°)$ of $(01\bar{1}0)$ (or $(10\bar{1}0)$) with respect to $(11\bar{2}1)$. The angle of the intersection lines between the facets and $(11\bar{2}1)$ is measured to be $55\pm2°$ (see the two dashed lines in Fig. 5.8(a)), also agreeing with the ideal value $54.2°$ calculated from the spatial relationship between $(01\bar{1}0)$, $(10\bar{1}0)$ and $(11\bar{2}1)$. Note in Fig. 5.8(a) each $(11\bar{2}1)$ terrace is shaded in several different colors, indicating the $(11\bar{2}1)$ terrace is stepped. The
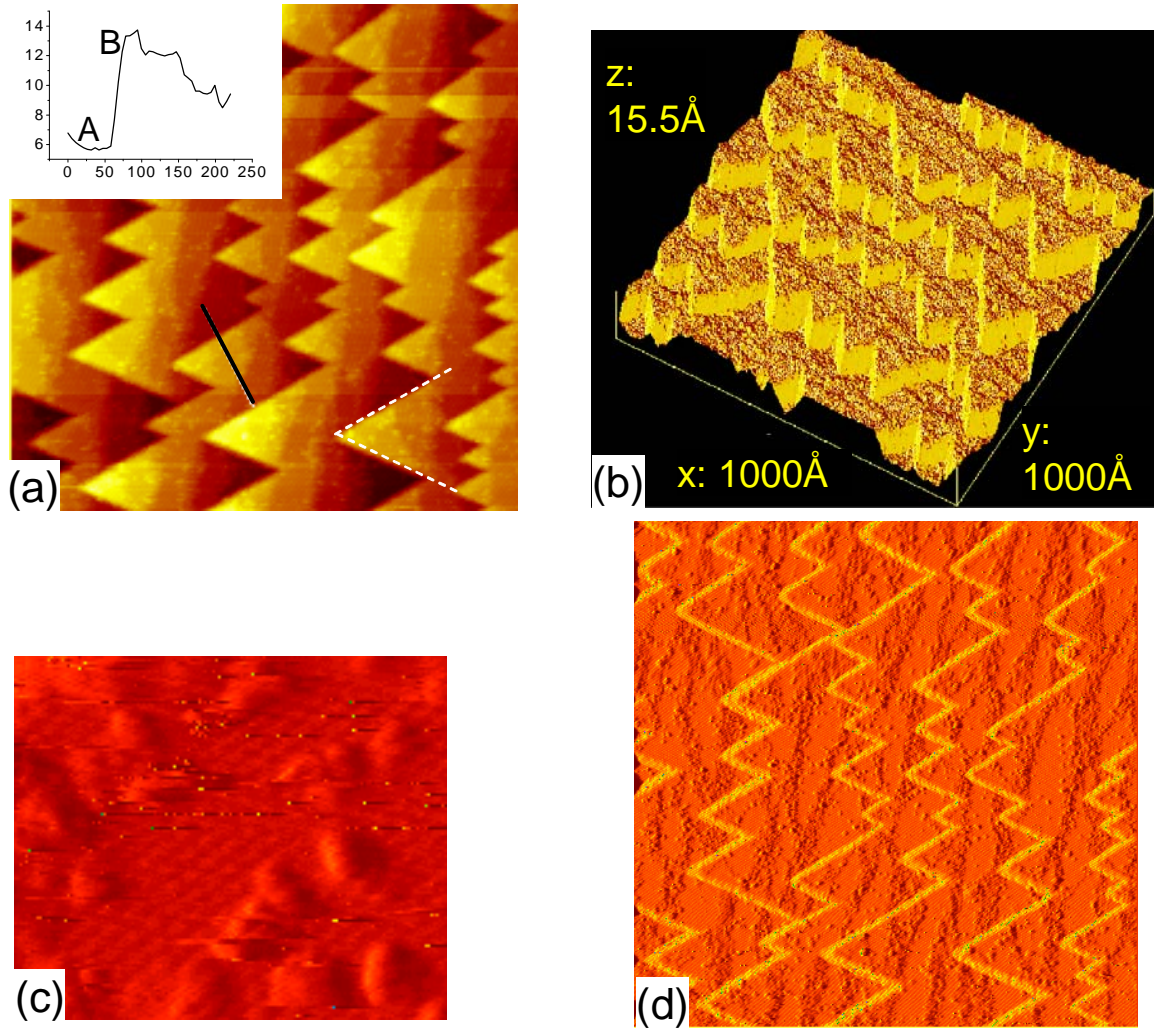
Fig. 5.8. 1000Å× 1000Å STM images of a partially faceted Re(11$\bar{2}$1) surface prepared by dosing 10L O$_2$ at 300K followed by annealing at 1000K. (a) top view with an inset showing a cross-section profile along the solid line marked in (a). (b) 3-D perspective view; (d) X-slope image. (c) 80Å× 60Å STM image from the same surface as (a) showing atomic structure of the (11$\bar{2}$1) terrace.

distribution of the steps can be better viewed in Fig. 5.8(d) after taking height derivative along the X direction; in the differentiated image the dark lines are the steps on the (11$\bar{2}$1) terrace; since (01 $\bar{1}$ 0), (10 $\bar{1}$ 0) and (11$\bar{2}$1) alone cannot retain the macroscopic orientation of the (11$\bar{2}$1) surface, these steps cause the local effective orientation of the terraces to deviate from (11$\bar{2}$1), which makes it possible to retain the macroscopic orientation.
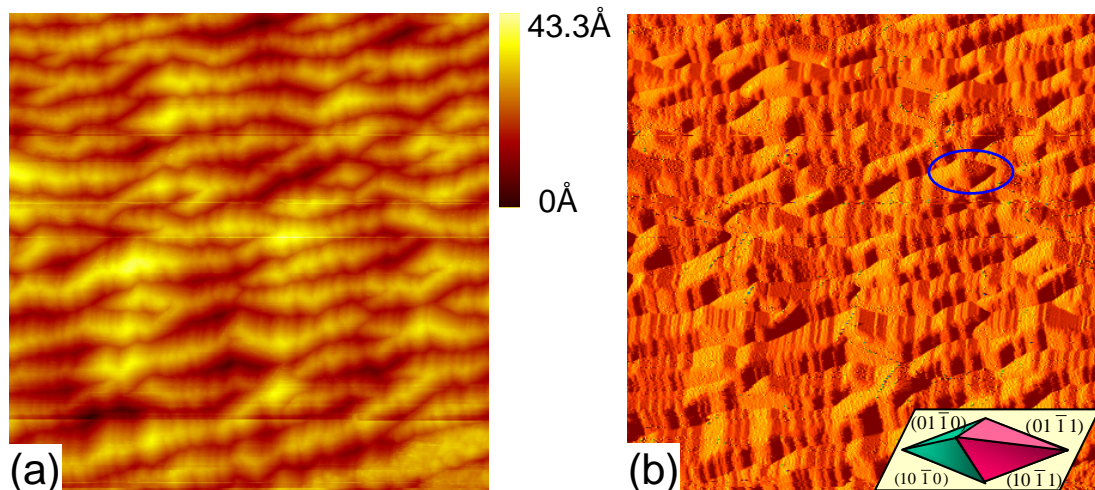
Fig. 5.9. 1000Å×1000Å STM images of a fully faceted Re($11\bar{2}1$) surface prepared by dosing 300L O_2 at 1000K: (a) raw image; (b)X-slope image. The oval in (b) highlights a 4-sided pyramid formed by four facets; a model of the pyramid is also shown in (b).

When the Re($11\bar{2}1$) surface is exposed to >120L O_2 at 800-1100K, it becomes completely faceted with four facets: ($01\bar{1}0$), ($10\bar{1}0$), ($01\bar{1}1$) and ($10\bar{1}1$). Figure 5.9(a) and (b) show typical raw and differentiated STM images after Re($11\bar{2}1$) is exposed to 300L O_2 at 1000K. Four different facets can be identified in Fig. 5.9 and in some regions they meet together to form 4-sided pyramids (see the pyramid marked by an oval in Fig. 5.9(b)). The orientations of these four facets can be confirmed by measuring the angles between facet edges. Figure 5.10(a) and (b) show the measured and ideal angles, respectively; the good agreement confirms the four stable facets are ($01\bar{1}0$), ($10\bar{1}0$), ($01\bar{1}1$) and ($10\bar{1}1$).
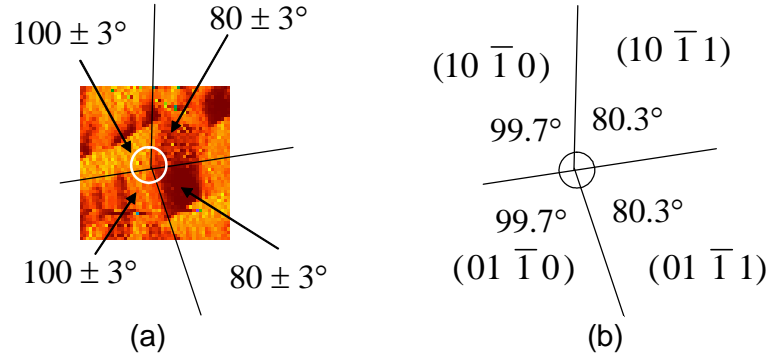
Fig. 5.10. Comparison of the angles between the facet edge lines. (a) experimental values; (b) calculated values.

5.3.3. Theoretical insights

Adsorbate-induced faceting is believed to be driven by the increased anisotropy of surface free energy due to differential adsorption of the adsorbates on surfaces with different orientation. The total surface energy is minimized by forming facets with low surface free energy although the total surface area may increase. The total surface free energy of a faceted surface per projected unit area on $(11\overline{2}1)$ is

$$\gamma_f = \sum_i \lambda_i \frac{\gamma_i}{\cos\theta_i}, \qquad (5.3)$$

where γ_i is the specific surface free energy of the ith facet, θ_i is the tilt angle between this facet and $(11\overline{2}1)$, and λ_i is a structure factor that accounts for the fact that the ith facet when projected on $(11\overline{2}1)$ only occupies part of the whole surface area; the constraint for λ_i is $\sum_i \lambda_i = 1$. Since the completely faceted surface formed by $(01\overline{1}0)$, $(01\overline{1}1)$, $(10\overline{1}0)$ and $(10\overline{1}1)$ is the most stable structure under quasi-equilibrium conditions (fixed sample temperature and constant background oxygen pressure), we focus our discussion on comparing its surface free energy with respect to that of $(11\overline{2}1)$. Using *ab-initial* DFT methods, we have calculated the surface free energies of clean

Table 5.1. Surface free energies for various clean surfaces from our DFT calculations. The tilt angles of the facets with respect to $(11\bar{2}1)$ are listed in the 3rd column; the structure factors of the facets are listed in the 4th column for the case when $(11\bar{2}1)$ is completely covered by $(01\bar{1}0)$, $(10\bar{1}0)$, $(01\bar{1}1)$ and $(10\bar{1}1)$.

Surface orientation	Surface free energy(eV/Å^2)	Tilt angle to $(11\bar{2}1)$	Structure factor
$(11\bar{2}1)$	0.220	0°	n/a
$(01\bar{1}0)$ or $(10\bar{1}0)$	0.183	34.2°	0.228
$(01\bar{1}1)$ or $(10\bar{1}1)$	0.213	29.7°	0.272

$(11\bar{2}1)$ and the facets, as shown in Table I; the tilt angles and the structure factors of the facets are also included in the table. For clean surfaces, although each of the facets has lower surface free energy than $(11\bar{2}1)$, the difference is not enough to offset the cost of surface area increase. By putting the relevant information taken from Table I into Eq.(5.3), we have $\gamma_f^{clean} = 0.234$ eV/Å^2, larger than $\gamma_{(11\bar{2}1)}^{clean} = 0.220$ eV/Å^2. Therefore, a clean $(11\bar{2}1)$ surface is stable against faceting, which agrees with the experimental observation.

When oxygen is adsorbed on $(11\bar{2}1)$ at room temperature, the saturation coverage is limited by the total available adsorption sites on $(11\bar{2}1)$. Only if the oxygen exposure is extremely high, can the oxygen coverage exceed the above saturation coverage due to oxygen diffusion into the subsurface and bulk.

For a surface covered with oxygen, since we cannot determine the actual coverage in the experiment, we calculate the surface free energy of planar or faceted Re$(11\bar{2}1)$ with various initial oxygen concentration as a function of oxygen chemical potential. The results are shown in Fig. 5.11(a), in which each line represents a planar or faceted surface with different initial oxygen concentration. For a given background oxygen pressure, for

(a)

(b) 1ML O/Re($11\bar{2}1$) (c) 2ML O/Re($11\bar{2}1$)

(d) 1ML O/Re($01\bar{1}0$) (e) 2ML O/Re($01\bar{1}0$) (f) 2ML O/Re($01\bar{1}1$)
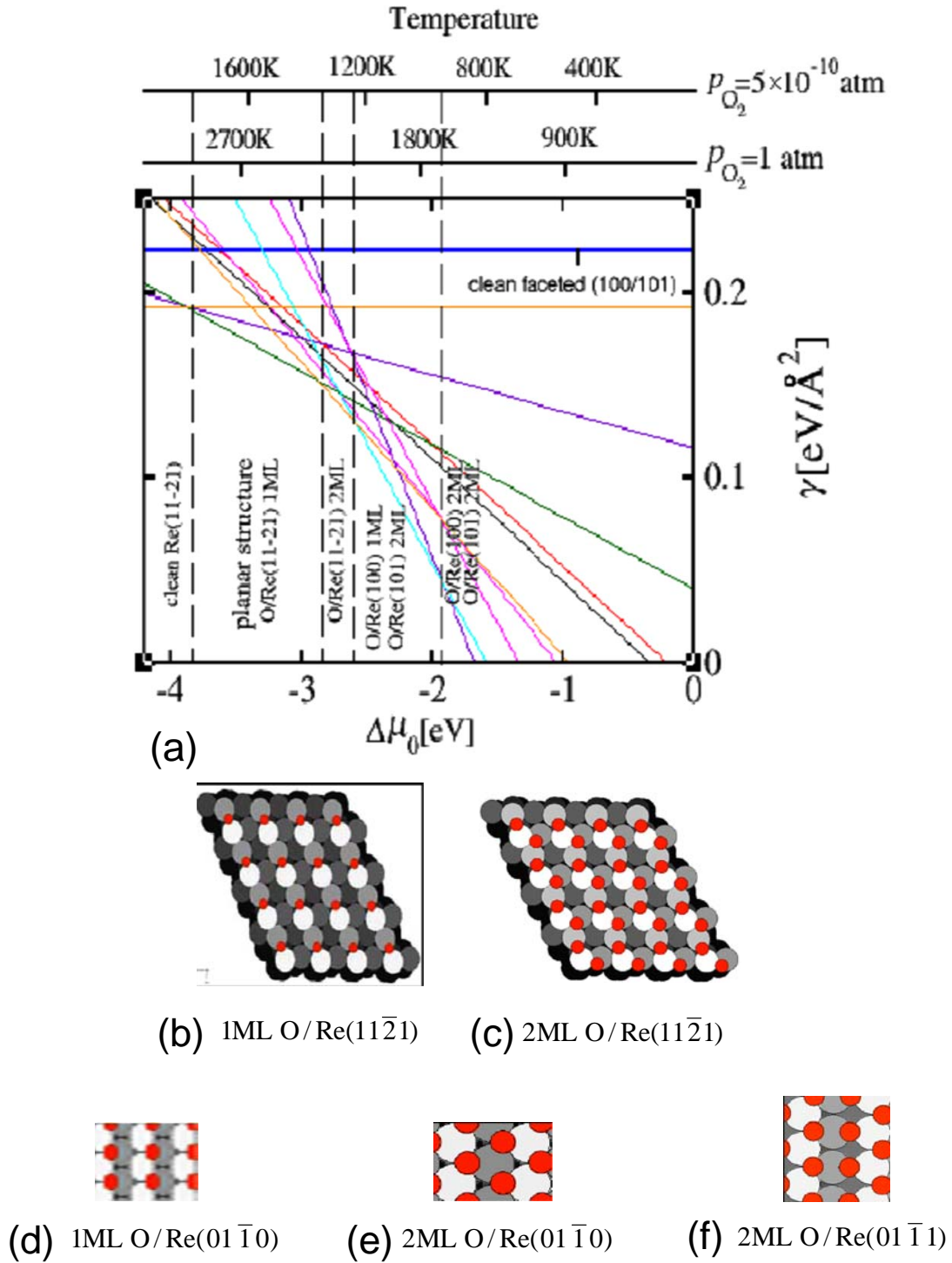
Fig. 5.11. (a) (p, T) phase diagram of the O/Re($11\bar{2}1$) system based on DFT calculations. (b)-(f) Calculated adsorption structures that appear in the phase diagram. From Ref. [12].

example, 5×10^{-10} atm used in our experiments, the oxygen chemical potential can be

converted into temperature which can be compared with the critical temperatures found experimentally. The surface-free-energy lines intersect with each other and the intersections determine some temperature windows, in which the structure that has the lowest surface free energies is the stable phase. Clearly the complete faceted surface with $(01\bar{1}0)$, $(01\bar{1}1)$, $(10\bar{1}0)$ and $(10\bar{1}1)$ facets is favored against planar $(11\bar{2}1)$ for T<1250K, which is consistent with our experimental observations. When the temperature is greater than 1250K, the oxygen-covered planar $(11\bar{2}1)$ surface is favored. When the temperature is even higher than 1700K, oxygen completely desorbs and a clean planar $(11\bar{2}1)$ surface becomes the most stable phase. Figure 5.11 (b)-(f) show the oxygen binding sites with the highest binding energy on $(11\bar{2}1)$, $(01\bar{1}0)$ and $(01\bar{1}1)$ for various oxygen coverages; here 1 monolayer (ML) refers to 1 oxygen atom per unit cell on $(11\bar{2}1)$, $(01\bar{1}0)$ or $(01\bar{1}1)$.

5.3.4. Structure models of facets and their connections

In O-induced faceting of Re$(11\bar{2}1)$, the surface morphology undergoes complex changes depending on the oxygen concentration on the surface. Among all the facets, $(01\bar{1}0)$ and $(10\bar{1}0)$ are stable and appear in all the faceted structures ranging from zig-zag chains to four-sided pyramids. This is not surprising since both facets are most close-packed among those near $(11\bar{2}1)$. However, for the other two metastable facets, $(33\bar{6}4)$ and $(11\bar{2}2)$, one may wonder why they take the path observed experimentally to evolve from one to another and eventually form $(01\bar{1}1)$ and $(10\bar{1}1)$ (Fig. 5.12(a)). Besides the thermodynamic driving force, are there any internal connections between their structures that may affect the kinetic process?

increasing oxygen coverage

(a)

(b)

(c)
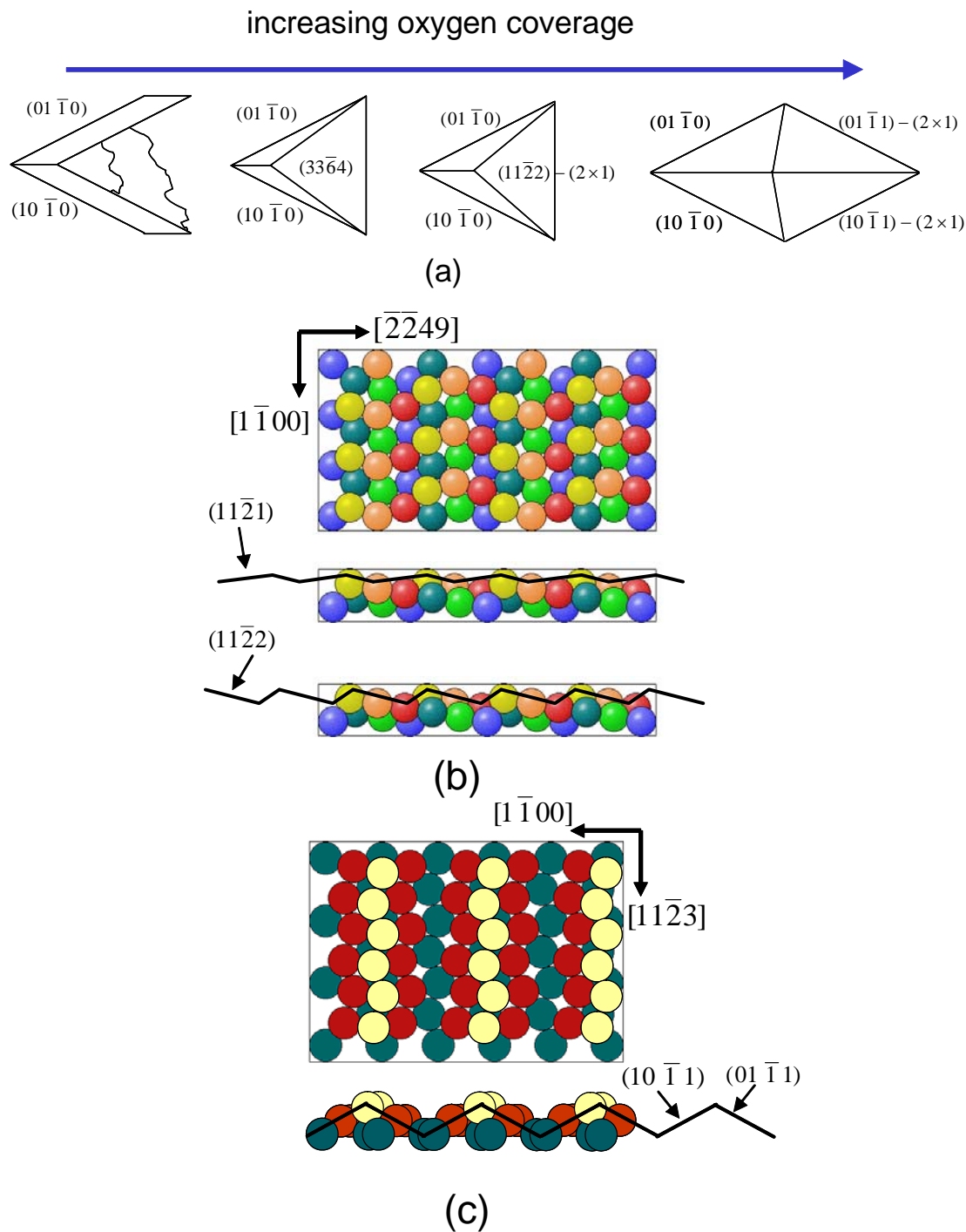
Fig. 5.12. (a) A schematic view of the morphological evolution of the facets. (b) A hard-sphere model of $(33\bar{6}4)$ with two ways of viewing the surface shown. (c) A proposed hard-sphere model of $(11\bar{2}2)$-(2×1). See text for details.

Figure 5.12 (b) and (c) show hard-sphere models of the metastable facets. A close

look at these models indeed reveals a natural connection between them. At the beginning,

when oxygen coverage is low, the surface is partially faceted with $\{01\bar{1}0\}$ facets coexisting with $(11\bar{2}1)$. Then an increase of oxygen coverage leads to the emergence of $(33\bar{6}4)$, whose bulk-truncated surface can be regarded as a stepped $(11\bar{2}1)$ surface with the terrace width equal to one $(11\bar{2}1)$ unit cell (Fig. 5.12(b)). So from the perspective of mass transport, it is an easy transition from $(11\bar{2}1)$ to $(33\bar{6}4)$. With further increasing oxygen coverage, $(33\bar{6}4)$ evolves into $(11\bar{2}2)$. This transition can be understood in the sense that $(33\bar{6}4)$ can also be considered as a stepped $(11\bar{2}2)$ surface from a different view angle (Fig. 5.12(b)). $(33\bar{6}4)$ is like a boundary state between $(11\bar{2}1)$ and $(11\bar{2}2)$; an increase of decrease of oxygen coverage can trigger $(33\bar{6}4)$ to tilt toward one or the other.

For the last transition from $(11\bar{2}2)$ to $\{01\bar{1}1\}$ at high oxygen coverages, there seems no natural connection between the structures of these two surfaces. However, since LEED shows that $(11\bar{2}2)$ is (2×1) reconstructed, a simple model based on reconstruction of the substrate may provide a clue. In this model (Fig. 5.12(c)), every other row of top-layer atoms along the $[11\bar{2}3]$ direction is removed, and the resulting $(11\bar{2}2)$-(2×1) surface contains micro-facets of $(01\bar{1}1)$ and $(10\bar{1}1)$. At high oxygen coverages, these micro-facets grow in size and eventually evolve into large $(01\bar{1}1)$ and $(10\bar{1}1)$ facets.

5.4. Conclusion

The clean Re$(11\bar{2}1)$ surface is stable against faceting upon annealing up to 2000K. However, oxygen can induce faceting of Re$(11\bar{2}1)$, and the morphology of the faceted surface depends on the surface preparation conditions. For oxygen adsorption at 300K with a moderate exposure between 3 and 60L, Re$(11\bar{2}1)$ only becomes partially faceted

upon annealing at T>700K; only $(01\overline{1}0)$ and $(10\overline{1}0)$ facets are observed forming zigzag chains and coexisting with stepped $(11\overline{2}1)$ terraces. Further increasing of the initial oxygen exposure, the $(11\overline{2}1)$ terraces are replace by $(33\overline{6}4)$ facets and eventually $(01\overline{1}0)$ and $(10\overline{1}0)$ facets also appear. For oxygen adsorption at high temperatures (700-1100K), the surface morphology also evolves as the oxygen exposure increases. First, the $(01\overline{1}0)$ and $(10\overline{1}0)$ facets appear and coexist with $(11\overline{2}1)$; then a (2×1) reconstructed $(11\overline{2}2)$ facet emerges and the surface becomes completely faceted; eventually, the $(11\overline{2}2)$ facet disappears and the surface is completely covered by four facets: $(01\overline{1}0)$, $(10\overline{1}0)$, $(01\overline{1}1)$ and $(10\overline{1}1)$. All facets disappear when the surface is annealed at T>1300K due to oxygen desorption and the surface reverts to planar. A connection between structures of the metastable facets is proposed, which may be related to the kinetics of mass transport. Our results indicate that the oxygen coverage is crucial in determining the morphology of a faceted $(11\overline{2}1)$ surface. A (T,p) phase diagram of the planar and faceted $(11\overline{2}1)$ surfaces is generated by DFT calculations. The calculation results confirm that the oxygen-induced enhancement of surface energy anisotropy is the driving force for faceting.

5.5. References

[1]   W. Chen, I. Ermanoski and T. E. Madey, J. Am. Chem. Soc. **127** (2005) 5014.

[2]   W. Chen, I. Ermanoski, T. Jacob and T. E. Madey, Langmuir **22** (2006) 3166.

[3]   L. S. Wang, R. Ohnishi and M. Ichikawa, J. Catal. **190** (2000) 276.

[4]   Y. Yuan, H. Liu, H. Imoto, T. Shido and Y. Iwasawa, J. Catal. **195** (2000) 51.

[5]   F. Solymosi, P. Tolmacsov and T. S. Zakar, J. Catal. **233** (2005) 51.

[6]   K. Liu, S. C. Fung, T. C. Ho and D. S. Rumschitzki, J. Catal. **206** (2002) 188.

[7]   H. Wang, W. Chen and T. E. Madey, Phys. Rev. B **74** (2006) 205426.

[8]   H. Wang, A. S. Y. Chan, W. Chen, P. Kaghazchi, T. Jacob and T. E. Madey, ACS Nano **1** (2007) 449.

[9]   M. D. Segall, P. L. D. Lindan, M. J. Probert, C. J. Pickard, P. J. Hasnip, S. J. Clark and M. C. Payne, J. Phys.: Condens. Matter **14** (2002) 2717.

[10]   D. Vanderbilt, Phys. Rev. B **41** (1990) 7892.

[11]   J. P. Perdew, K. Burke and M. Ernzerhof, Phys. Rev. Lett. **77** (1996) 3865.

[12]   P. Kaghazchi, T. Jacob, H. Wang, W.Chen and T. E. Madey, in preparation.

[13]   H. J. Monkhorst and J. D. Pack, Phys. Rev. B **13** (1976) 5188.

[14]   K. Reuter and M. Scheffler, Phys. Rev. B **65** (2001) 35406.

[15]   D. R. Stull and H. Prophet, *JANAF thermochemical tables*, 2nd ed., U.S National Bureau of Standards, Washington, DC, (1971).

[16]   M.-C. Desjonqueres and D. Spanjaard, *Concepts in surface physics*, Springer-Verlag, Berlin, (1993).

[17]   H. Wang, A. S. Y. Chan, W. H. Chen, P. Kaghazchi, T. Jacob and T. E. Madey, ACS Nano **1** (2007) 449.

Chapter 6   Ammonia induced reconstruction and faceting on Re($11\bar{2}1$)

6.1 Introduction

In chapters 3-5 we have demonstrated that oxygen adsorption can induce complex morphological changes through facet formation on Re surfaces; the driving force is the anisotropy of surface free energy which depends on oxygen coverage. One may wonder whether other adsorbate species can also induce faceting on Re surfaces. If the answer is yes, what are the facet orientations? Are they the same as those observed in O-induced faceting? To answer these questions, we choose to study the adsorption of ammonia on Re($11\bar{2}1$).

Ammonia (chemical formula NH_3) is one of the most significant products in chemical industry; it is a key raw material for synthesis of fertilizers, nitrogen-containing compounds and many pharmaceuticals. The worldwide production of ammonia in 2006 was estimated at 146.5 M tons [1]. It has been reported that rhenium and rhenium nitride are good catalysts for the synthesis of ammonia, and their catalytic activity is found to be structural sensitive [2-4]. It has also been reported that ammonia can induce faceting of Mo(111) [5]; the facets have {433} orientations that are different from the {447} and {211} facets found in O-induced faceting of Mo(111) [6]; If ammonia can induce faceting of Re($11\bar{2}1$), the faceted surface can be a good model system to study structural sensitivity in ammonia related reactions.

In this chapter, we report a combined experimental-theoretical investigation of the adsorption of ammonia on Re($11\bar{2}1$), focusing on the surface reconstruction and faceting induce by nitrogen that comes from the dissociation of ammonia. DFT calculations are also employed to understand the thermodynamic driving force of N-induced faceting. For

reference, a hard-sphere model of Re($11\bar{2}1$) and its position in the stereographic projection plot are given in Fig. 6.1.

(a)   (b)

(c)
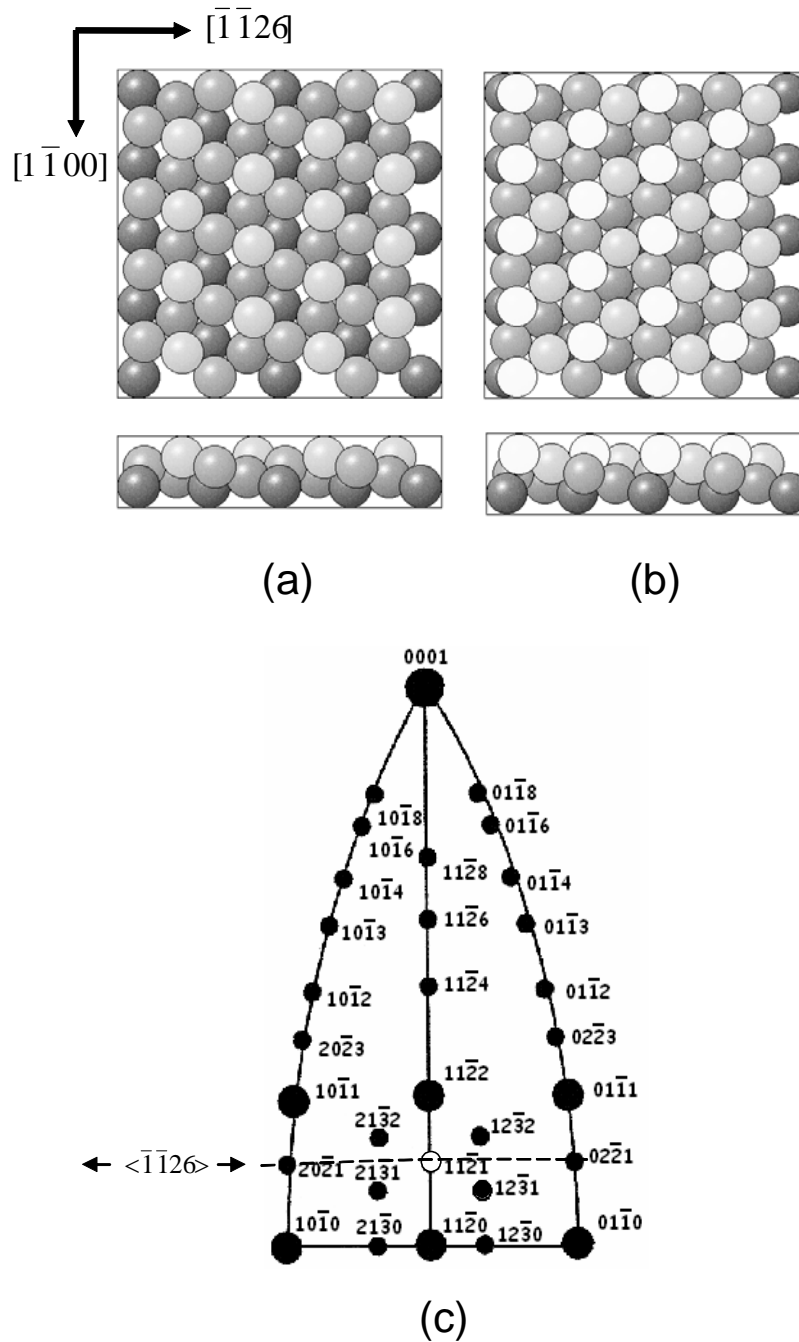
Fig. 6.1. Hard-sphere models of the two different terminations of bulk truncated Re($11\bar{2}1$) in (a) and (b). (c Stereographic projection plot of the hcp lattice on ($11\bar{2}0$). The ($11\bar{2}1$) surface is labeled by a hollow circle and the <$\bar{1}\bar{1}26$> zone is labeled by a dashed line.

6.2 Experimental and computational procedures

The experimental procedure is similar to that described in Chapter 3. The only difference is that after the $Re(11\bar{2}1)$ surface is cleaned, NH_3 instead of O_2 is introduced in the UHV chamber through a different leak valve for following experiments.

The DFT computational procedure is similar to that described in Chapter 5. The calculations are performed by Jacob and Kaghazchi [7]. The Brillouin zones of the (1×1)-surface unit cells of $Re(11\bar{2}1)$, $(13\bar{4}2)$, $(01\bar{1}0)$, and $(01\bar{1}1)$ are sampled with (4×4), (3×3), (5×8), and (4×8) Monkhorst–Pack k-point meshes. These surfaces are represented by 19-layer, 30-layer, 11-layer, and 14-layer slabs, respectively, separated by at least 13Å vacuum. For each system, the bottom four layers are fixed at the calculated bulk-crystal structure, and the remaining Re atoms and the adsorbates are allowed to freely relax. In the calculation, the system is assumed to be a N-covered surface in contact with a N_2 gas reservoir rather than NH_3-covered surface in a NH_3 environment. In section 6.3.1, we will show that this assumption is reasonable since NH_3 decomposes on Re surfaces at room temperature and the observed faceting is induced by N which desorbs as N_2 at high annealing temperatures.

6.3 Results

6.3.1 AES and TPD results

The N/Re AES peak height ratio is measured after $Re(11\bar{2}1)$ is exposed to different amounts of NH_3 at 300K. As shown in Fig. 6.2, after a rapid growth with increasing NH_3 exposure, the N/Re ratio saturates when the NH_3 exposure is greater than 6L, indicating the surface reaches a full coverage.
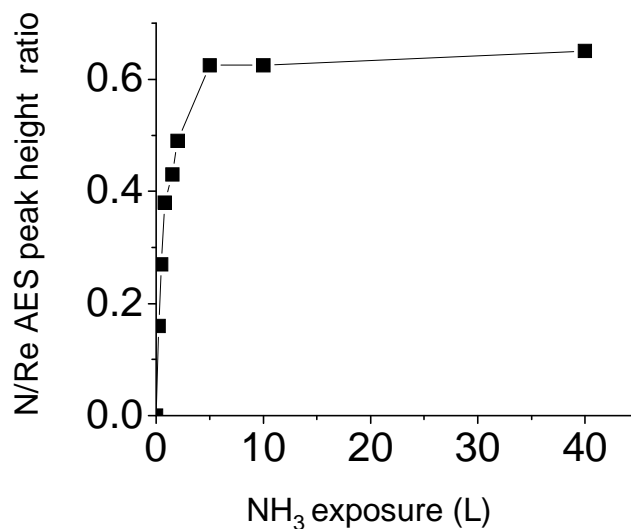
Fig. 6.2. AES uptake curve of NH_3 on $Re(11\bar{2}1)$ at 300K. The electron energies of the N and Re peaks are 392 eV and 176 eV, respectively.

To understand the surface composition after NH_3 adsorption, TPD spectra are measured from a fully covered surface after being exposed to 30L NH_3 at 300K (Fig. 6.3). No NH_3 signal is found in TPD measurements and the only species detected are N_2 and H_2, which indicates that NH_3 dissociates completely into N and H on $Re(11\bar{2}1)$.
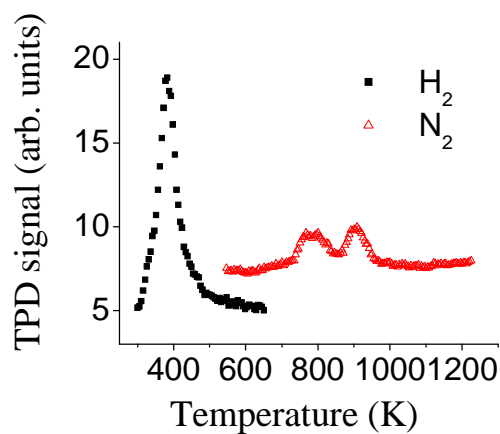
Fig. 6.3. TPD spectra taken after adsorption of 30L NH_3 on $Re(11\bar{2}1)$ at 300K

When the annealing temperature is slightly above 300K, adsorbed H aotms start to recombine into H_2 and desorb from the surface. By ~600K, all the adsorbed H atoms desorb in the form of H_2 and the surface is left only with N. The desorption behavior of hydrogen is in agreement with previous studies on H/Re(0001) [8-10]. N starts to desorb as N_2 when the annealing temperature is greater than 600K and completely desorbs by 1100K.

6.3.2 LEED and STM results

No reconstruction is found in LEED after $Re(11\bar{2}1)$ is exposed to NH_3 (up to 30L) at 300K. The LEED pattern (Fig. 6.4(a)) is the same as that from a clean $Re(11\bar{2}1)$ surface except for a slight increase in the background signal due to random adsorption of NH_3. When the incident electron energy (E_e) increases, all the diffraction beams move toward the center of the LEED screen, indicating that the surface remains planar. Annealing the NH_3-covered surface at 400-600K brings no change of the LEED pattern; however, for NH_3 exposure greater than 0.5L at 300K, extra beams appear in the LEED pattern (Fig. 6.4(b)) after the surface is annealed at 600-700K. These extra beams are located in the half-integral positions along the $[\bar{1}\,\bar{1}26]$ direction and are more diffuse than the original (1×1) beams. This (2×1) reconstructed surface remains planar since all the beams still move to the center of the LEED screen when E_e increases.

The (2×1) reconstruction only exists in a narrow temperature window because the half-integral order beams completely disappear when the surface is further annealed at temperatures higher than 800K. Meanwhile, new features start to emerge and coexist with the (1×1) beams from $(11\bar{2}1)$. These new features become well developed when the annealing temperature is about 900K (see an example beam marked by an arrow in Fig.
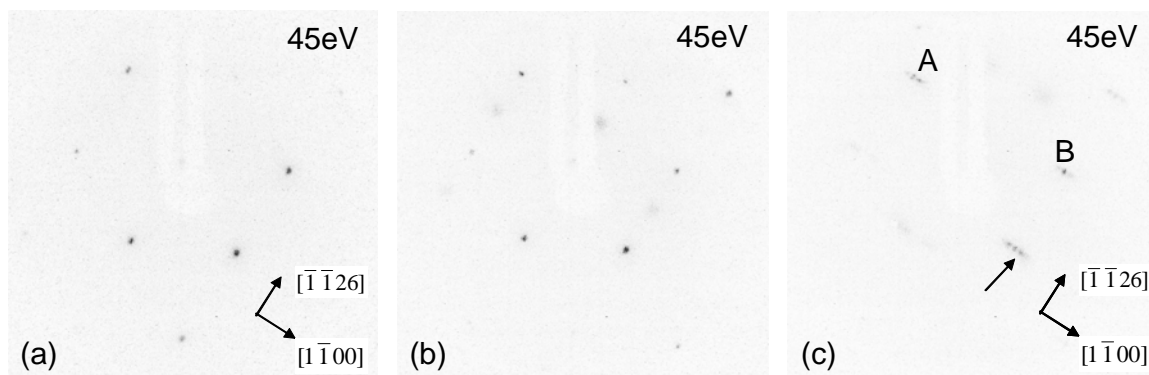
Fig. 6.4. LEED patterns taken in an annealing sequence after adsorption of 30L NH_3 on $Re(11\bar{2}1)$ at 300K: (a) as dosed, (b) 700K and (c) 900K. See text for labels.

6.4(c)). When E_e increases, these new beams do not move toward the screen center but two off-center positions located on the $[1\bar{1}00]$ direction, indicating that they are from two facets. Just like the (1×1) beams, these facet beams also have a mirror symmetry along the $[\bar{1}\bar{1}26]$ direction. Moreover, they always fall on the lines defined by the (1×1) beams along the $[1\bar{1}00]$ direction, which is an evidence that the reciprocal rods corresponding to the new beams are in the same planes as those correspond to the (1×1) beams along the $[1\bar{1}00]$ direction. Two examples of such (1×1) beams are labeled as A and B in Fig. 6.4(c), whose reciprocal rods should be in the plane normal to $[\bar{1}\bar{1}26]$ based on structure of $Re(11\bar{2}1)$; note that the (1×1) LEED pattern is rotated by 90° with respect to the atomic structure of $Re(11\bar{2}1)$ in real space. Therefore, the crystallographic zone axis of the two facets and $Re(11\bar{2}1)$ must be $[\bar{1}\bar{1}26]$. In the $<\bar{1}\bar{1}26>$ zone, $(02\bar{2}1)$ and $(20\bar{2}1)$ planes seem to be good candidates for the facets (see Fig. 6.1(c)). However, a kinematical simulation of the LEED pattern based on their surface structures rules out this possibility. Although the determination of the zone axis of the facets greatly reduces the size of candidate pool for the facet orientations, it is difficult to identify the facets just by this trial and error method; we need to know the tilt angles between the facets and

Re(11$\overline{2}$1) by locating the specular beams from the facets. However, because the surface in Fig. 6.4 (c) is partially faceted, the specular beams from the facets are weak whose locations are hard to identify. In the following, we will show that this obstacle can be overcome by preparing a fully faceted Re(11$\overline{2}$1) surface with NH$_3$ exposure at high substrate temperature. The partially faceted surface reverts to the unreconstructed planar surface upon further annealing at T>1000K, which is due to desorption of N.

In the above LEED experiments, the highest coverage of N is limited by the saturation coverage of NH$_3$ at 300K. To exceed this limit and explore possible new surface morphologies, we switch to NH$_3$ adsorption at high substrate temperatures. Figure 6.5(a) shows a typical LEED pattern taken after dosing 100L NH$_3$ on Re(11$\overline{2}$1) at 700K. The surface is (2×1) reconstructed similar as that in Fig. 6.4(b) but with more intense half-integral order beams, indicating the reconstruction is better developed. When Re(11$\overline{2}$1) is exposed to 100L at 900K, the LEED pattern changes drastically (Fig. 6.5(b)): the (1×1) beams completely disappear and the remaining beams are from two facets same as those found in Fig. 6.4(c). The specular beams of the facets can now be easily located because the beam intensity is higher than in Fig. 6.4(c) (see the two beams marked by circles in Fig. 6.5(b)). The orientations of the two facets can be identified by comparing their positions with the (1×1) diffraction beams from Re(11$\overline{2}$1).

Because the two facets are symmetrical along the [$\overline{1}\,\overline{1}$26] direction, for illustration purpose, we only need to focus on one of them: for example, the one whose specular beam is on the lower right side of Fig. 6.5(b). This specular beam is located in the same position as the (2, -1) beam from planar Re(11$\overline{2}$1) at E$_e$ equal to 100 ± 5eV (Fig. 6.5(c)). The corresponding angle between the (2, -1) beam and the normal direction

of
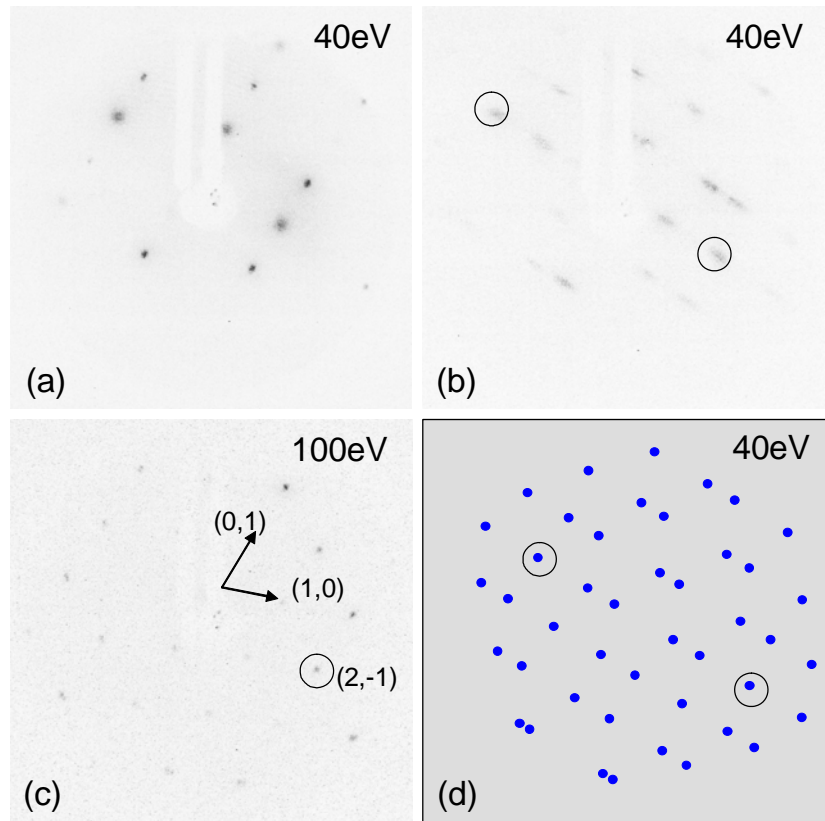
Fig. 6.5. LEED patterns of Re($11\bar{2}1$) taken after being exposed to 100L NH_3 at different temperatures: (a) 700K and (b) 900K. Specular beams of the two facets are labeled by circles in (b). (c) LEED pattern of planar Re($11\bar{2}1$) at E_e=100eV; the (2,-1) beam (marked by a circle) is located in similar position as one of the specular beams in (b). (d) is a kinematical simulation of (b) with the specular beams labeled.

($11\bar{2}1$) is $30.9 \pm 0.9°$ on the basis of the Ewald sphere construction of the LEED pattern of planar ($11\bar{2}1$) [11], which is equal to the angle between the specular beam of the facet and the normal direction of ($11\bar{2}1$). Therefore, the tilt angle of the facet with respect to ($11\bar{2}1$) is $15.5 \pm 0.5°$, which, combined with the fact that the facet lies in the $<\bar{1}\bar{1}26>$ zone, suggests that ($13\bar{4}2$) (or symmetrical counterpart ($31\bar{4}2$)) is the facet orientation; the tilt angle between ($13\bar{4}2$) and ($11\bar{2}1$) is $15.4°$. To confirm this facet identification, a kinematical simulation of the faceted LEED pattern is generated based on the 2-D lattice structures of bulk truncated Re($13\bar{4}2$) and ($31\bar{4}2$). The simulated LEED pattern shown

in Fig. 6.5(d) resembles the experimental pattern in Fig. 6.5(b), not only confirming the facet orientations but also indicating that both facets are not reconstructed.

The fully faceted surface can also be revealed in real space by STM. Figure 6.6(a) shows a typical STM image taken after the $Re(11\overline{2}1)$ surface is exposed to 300L NH_3 at 900K. The two facets form ridges longer than 1000 Å with an average width of ~50 Å. A cross-section profile of the ridges is shown Fig. 6.6(b), in which the symmetrical shape of the saw-tooth like features agrees with the LEED observation that the two facets are symmetrical with each other. By measuring the slope of each line segment, the tilt angle of each facet relative to $(11\overline{2}1)$ is $14 \pm 2°$, consistent with the LEED results.

(a)   (b)
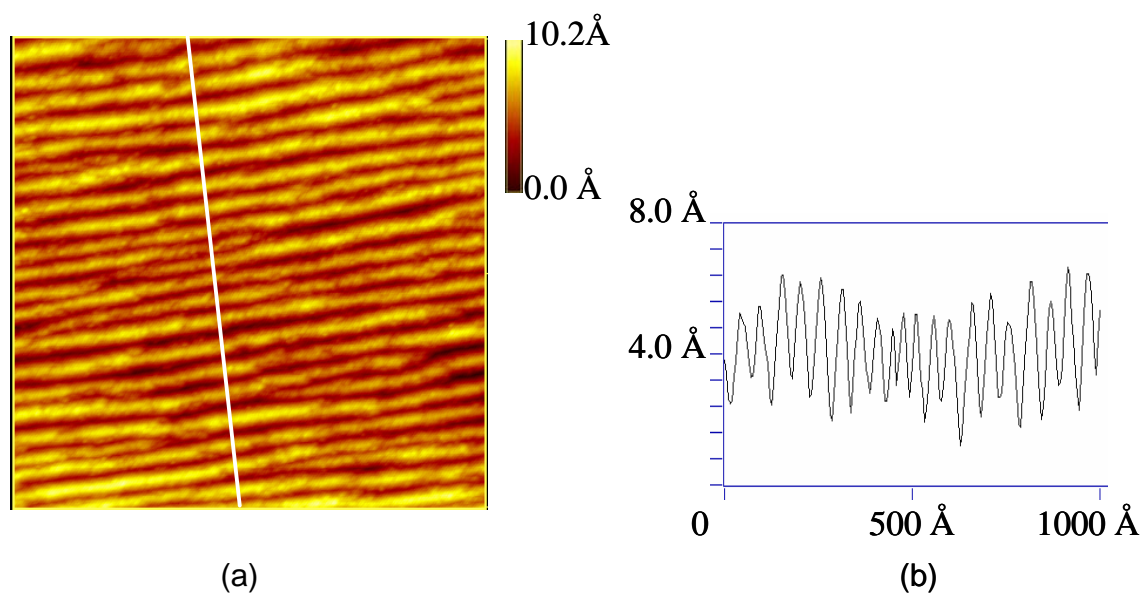
Fig. 6.6. (a) 1000Å× 1000Å STM image of a fully faceted $Re(11\overline{2}1)$ surface prepared by dosing 300L NH_3 at 900K. (b) shows the cross section profile along the line labeled in (a).

6.4 Discussion

The LEED results show that $Re(11\overline{2}1)$ either becomes partially faceted upon adsorption of NH_3 (exposure >0.5L) at 300K followed by annealing at 800-900K or becomes fully faceted after being exposed to NH_3 (>100L) at 800-900K. In this

temperature range for both cases, we know from the TPD results that the surface is only left with N atoms that come from the dissociation of NH_3. Therefore, the faceting observed is actually induced by adsorbed N rather than molecular NH_3. Since a fully faceted surface is achieved only by dosing NH_3(>100L) at 800-900K, one may ask if rhenium nitride forms on the surface and contributes to the facet formation. A previous study shows that rhenium nitride decomposes thermally to the metal above 645K [12], therefore, rhenium nitride is not responsible for the faceting process.

Figure 6.7(a) shows a hard-sphere model of the $(13\bar{4}2)$ surface; it is atomically rough with eight atomic layers exposed while the $(11\bar{2}1)$ surface only exposes four atomic layers. It seems counter-intuitive that $(13\bar{4}2)$ and $(31\bar{4}2)$ appear as facets because they are less close-packed than $(11\bar{2}1)$ and may have higher surface free energy. The answer is probably related to the unique structure of $(13\bar{4}2)$. If we look at $(13\bar{4}2)$ from a

(a)   (b)

Fig. 6.7. Hard sphere model of the $(13\bar{4}2)$ surface shown in (a) top view and side view, and (b) 3-D perspective view.

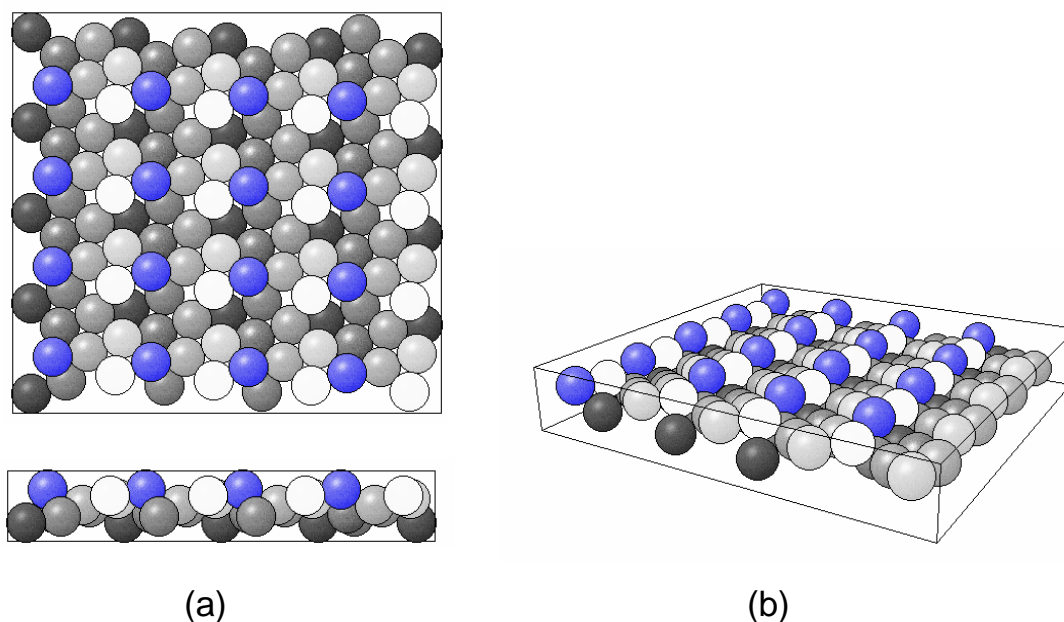certain perspective as shown in Fig. 6.7(b), we realize that $(13\bar{4}2)$ is actually a vicinal

$(01\bar{1}1)$ surface with kinked steps and $(01\bar{1}1)$ terraces that are more close-packed than $(11\bar{2}1)$. With adsorption of N, the surface free energy of the terraces may be reduced to the extent that even the stepped surface is more favorable than $(11\bar{2}1)$.

The above qualitative discussion of the stability of $\{13\bar{4}2\}$ facets is further supported by DFT calculations of the (T, p) phase diagram (Fig. 6.8). In the phase diagram, each line represents the surface free energy of a certain phase as a function of the nitrogen chemical potential that can also be converted into a temperature scale for a given background pressure. All the phases can be divided into three categories based on their surface morphologies: planar $(11\bar{2}1)$, ridges formed by $(13\bar{4}2)$ and $(31\bar{4}2)$ facets, and pyramidal structures formed by $(01\bar{1}0)$, $(10\bar{1}0)$, $(01\bar{1}1)$ and $(10\bar{1}1)$ facets, which are represented by solid, dashed and dot-dashed lines in Fig. 6.8, respectively; phases within each category have different N coverages. For the experimental nitrogen pressure (5×10^{-10} atm), Figure 6.8 shows that a clean planar $(11\bar{2}1)$ surface is the most stable phase when the temperature is greater than 1080K. This agrees with both the TPD result of complete N desorption at 1100K and the LEED result of a planar (1×1) pattern at T>1000K. Once the temperature is below 1080K, the ridges formed by $(13\bar{4}2)$ and $(31\bar{4}2)$ facets become the most stable phase; the lower the temperature is, the higher the N coverage on the ridges. For this whole temperature range, the pyramidal structures formed by $(01\bar{1}0)$, $(10\bar{1}0)$, $(01\bar{1}1)$ and $(10\bar{1}1)$ facets always have higher surface free energy than the ridges, although they are the favored phase observed in O-induce faceting of Re($11\bar{2}1$). The facets observed in N-induced faceting of Re($11\bar{2}1$) are different form those in O-induced faceting of Re($11\bar{2}1$); this demonstrates that even for

the same substrate, different adsorbate-substrate interactions can lead to distinct pathways of how the anisotropy of surface free energy changes as a function of adsorbate coverage.
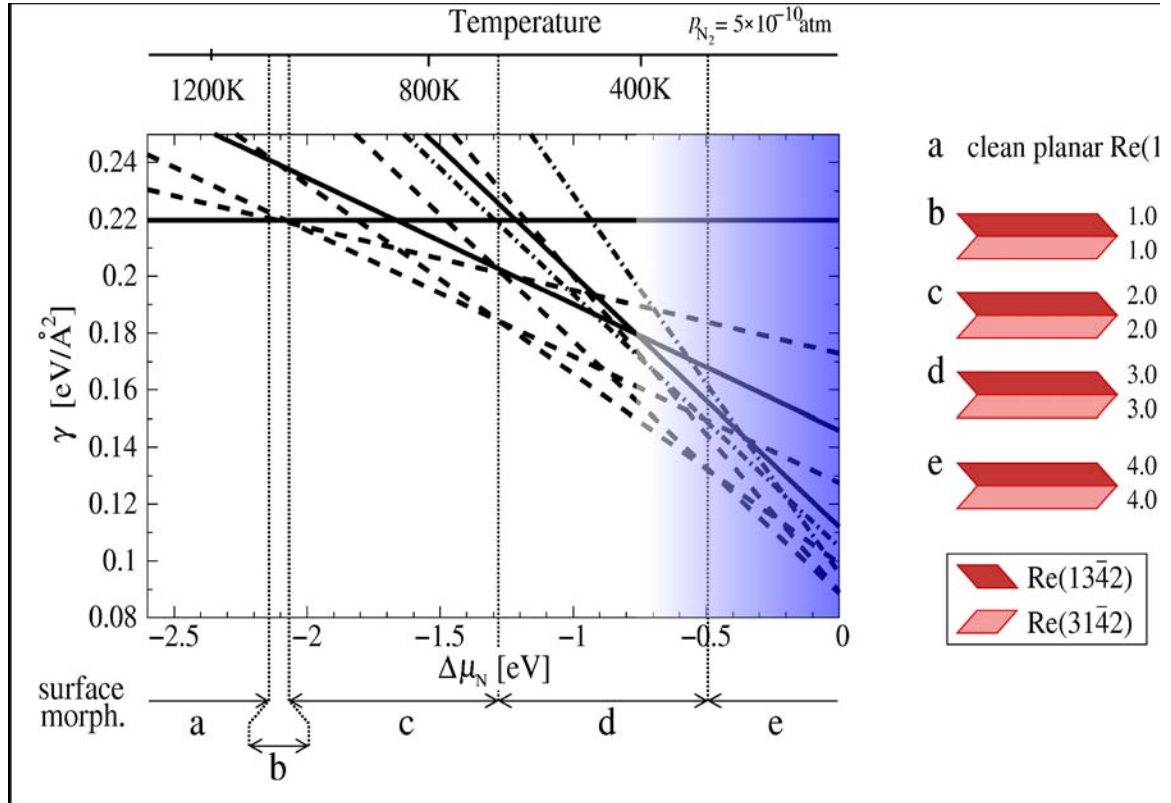
Fig. 6.8. Surface phase diagram for N-induced faceting of planar Re($11\overline{2}1$) showing the surface free energy as a function of the nitrogen chemical potential referenced as $\Delta\mu_N = \mu_N - \frac{1}{2}E_{N_2}^{total}$. The solid, dashed and dot-dashed lines represent substrate, two-sided ridges and four-sided pyramids. From Ref. [7].

The (2×1) LEED pattern of Re($11\overline{2}1$) upon annealing at 600-700K can be due to a reconstruction of either the N overlayer or the Re($11\overline{2}1$) substrate. The half-integral order beams show a weaker intensity than the integral order ones, which may indicate that the (2×1) pattern is related to an overlayer reconstruction. However, since the unit cell of Re($11\overline{2}1$) is so large in comparison with the atomic size of N, one expects the saturation coverage is higher than that of a (2×1) overlayer reconstruction. Moreover, a
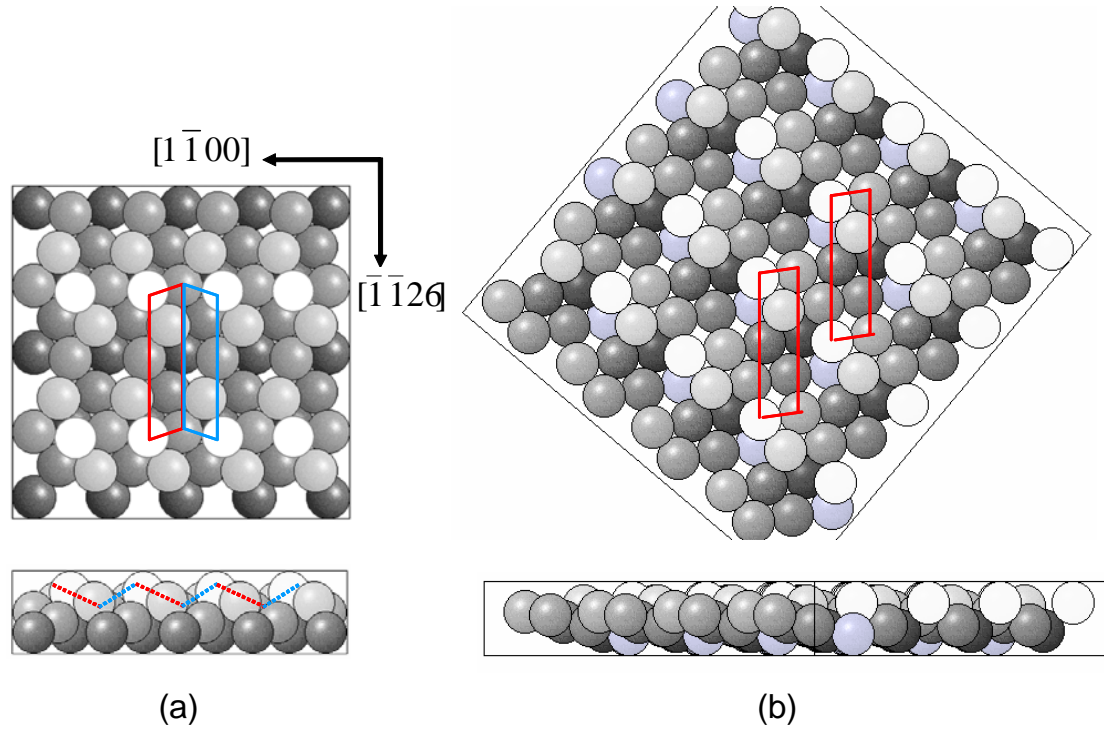
Fig. 6.9. (a) A proposed model for the (2×1) reconstructed (11$\bar{2}$1) surface with every other row of atoms in the top layer along the [1$\bar{1}$00] direction removed. The dash lines in the side view show that this surface is made of two micro-facets; unit cells of the micro-facets are marked in the top view of the model. (b) A certain view of (13$\bar{4}$2) as a stepped surface with terraces made of one of the micro-facets in (a); unit cells of two adjacent terraces are marked.

(2×1) substrate reconstruction is appealing in the sense that it can provide a natural link to the formation of {13$\bar{4}$2} facets. Figure 6.9(a) shows a proposed model of a (2×1) substrate reconstruction of Re(11$\bar{2}$1), in which every other row of atoms in the top layer along the [1$\bar{1}$00] direction are removed. The side view of the model clearly shows that this reconstructed surface is made of two micro-facets whose unit cells are marked in the top view of the model. On the other hand, each {13$\bar{4}$2} facet can be regarded as a stepped surface with the terraces made of either of the same two micro-facets (example of (13$\bar{4}$2) shown in Fig. 6.9(b)). Thus the (2×1) reconstruction can be considered as a precursor state of faceting; the formation of {13$\bar{4}$2} facets may be hindered by kinetic

barriers at 600-700K. Nevertheless, the very nature of the (2×1) reconstruction still needs further investigations.

6.5 Conclusion

Ammonia dissociates completely into N and H upon adsorption on Re(11$\bar{2}$1) at 300K. Hydrogen desorbs completely in the form of H_2 by ~600K, the remaining nitrogen atoms on the surface are responsible for the faceting observed upon annealing at 800-900K. Nitrogen also desorbs completely from the surface in the form of N_2 by ~1100K.

Re(11$\bar{2}$1) becomes partially faceted when it is exposed to ammonia (>0.5L) at 300K followed by annealing at 800-900K. A fully faceted surface can only be obtained by high dose of ammonia (>100L) at 800-900K. The facets are (13$\bar{4}$2) and (31$\bar{4}$2); their stability is supported by DFT calculations of the corresponding surface free energies and may be related to the fact that they are stepped {01$\bar{1}$1} surfaces. A (2×1) reconstructed LEED pattern is observed when the N-covered Re(11$\bar{2}$1) surface is annealed at 600-700K. A model involving reconstruction of the substrate is proposed which suggests this reconstruction may be a precursor state for faceting.

The drastic difference between N-induced and O-induced faceting of Re(11$\bar{2}$1) demonstrates its surface morphology can be tailored by choosing proper adsorbate species. This advantage makes Re(11$\bar{2}$1) a good substrate for studies of structure sensitivity in Re related catalytic reactions; the various faceted surfaces can also be used as templates for nano-structure growth.

6.6 References

[1]   M. Appl, in *Ullmann's Encyclopedia of Industrial Chemistry*, Wiley-VCH, (2006).

[2]   M. Asscher and G. A. Somorjai, Surf. Sci. **143** (1984) L389.

[3]   R. Kojima and K. Aika, Appl. Catal. A-Gen. **209** (2001) 317.

[4]   N. D. Spencer and G. A. Somorjai, J. Phys. Chem. **86** (1982) 3493.

[5]   C. Egawa, S. Naito and K.Tamaru, Surf. Sci. **125** (1983) 605.

[6]   K.-J. Song, J. C. Lin, M. Y. Lai and Y. L. Wang, Surf. Sci. **327** (1995) 17.

[7]   P. Kaghazchi, T. Jacob, H. Wang, W.Chen and T. E. Madey, in preparation.

[8]   J.-W. He and D. W. Goodman, J. Phys. Chem. **94** (1990) 1502.

[9]   D. G. Kelly, J. A. Odriozola and G. A. Somorjai, J. Phys. Chem. **91** (1987) 5695.

[10]   F. Zaera and G. A. Somorjai, Surf. Sci. **154** (1985) 303.

[11]   M.-C. Desjonqueres and D. Spanjaard, *Concepts in surface physics*, Springer-Verlag, (1993).

[12]   P. Clark, B. Dhandapani and S. T. Oyama, Appl. Catal. A-Gen. **184** (1999) L175.

Chapter 7   Conclusions

We have studied adsorbate-induced reconstruction and nanoscale faceting of atomically rough rhenium (Re) surfaces, which is the first systematic investigation of morphological instability of hexagonal close-packed (hcp) metal surfaces. This research is motivated by use of faceted surfaces as model systems to study structure sensitivity and size effects in heterogeneous catalysis as well as templates to grow ordered nanostructures.

We focus on two Re surfaces: Re($12\bar{3}1$) and Re($11\bar{2}1$), and take an approach that combines both experimental surface science techniques and calculations based on density functional theory (DFT). The results reveal a complex morphological evolution in oxygen or nitrogen-induced faceting of Re surfaces depending on adsorbate coverage and species; this is in great contrast with previously studied faceting of metal surfaces with body-centered cubic (bcc) or face-centered cubic (fcc) structures, where simple surface morphologies were often found.

Chapters 2 and 3 are devoted to oxygen-induced faceting of Re($12\bar{3}1$). We have found that the morphology of the surface depends on oxygen coverage. For oxygen coverage $\theta < 0.5$ML (monolayer, defined as the saturation coverage of oxygen on Re($12\bar{3}1$) at 300K), the O/Re($12\bar{3}1$) surface remains planar upon annealing. However, for 0.5ML $\leq \theta < 0.7$ML, the O/Re($12\bar{3}1$) surface becomes partially faceted upon annealing at $\geq$700K. For 0.7ML $\leq \theta < 0.9$ML, the O/Re($12\bar{3}1$) surface becomes completely faceted, forming long sawtooth ridges which are composed of ($01\bar{1}0$) and ($11\bar{2}1$) facets upon annealing at $\geq$700K. The distance between the ridges is quite

uniform and the ridges have atomically sharp edges. For 0.9ML $\leq \theta <$ 1ML, similar annealing treatment leads to the emergence of $(10\overline{1}0)$ facets which truncate the original ridges. With the surface fully covered by oxygen ($\theta = $ 1ML), a fourth facet $(01\overline{1}1)$ becomes prominent. This morphological evolution is accompanied by the reduction of the average ridge length along $[\overline{2}113]$, indicating that the $(11\overline{2}1)$ facet is metastable.

In order to exceed the coverage limit imposed by oxygen adsorption at 300K, we also expose Re($12\overline{3}1$) to a large amount of oxygen (> 120L) at high temperatures (800-1000K). Under this condition, the $(11\overline{2}1)$ facet becomes unstable and is replaced by a new facet $(10\overline{1}1)$. This transition is correlated with the formation of surface oxides ReO and Re_2O_3, as revealed by synchrotron radiation based high resolution soft X-ray photoemission spectroscopy (HRSXPS).

The results also show that the facets grow in size to minimize the edge energy as the annealing temperature or time increases. All the facets completely disappear when the surface is annealed at T > 1300K due to desorption of oxygen.

Chapters 5 describes oxygen-induced faceting of Re($11\overline{2}1$) and the results show that the coverage dependence of surface morphology is a general phenomenon on oxygen-covered Re surfaces. For oxygen adsorption at 300K with a moderate exposure between 3 and 60L, Re($11\overline{2}1$) only becomes partially faceted upon annealing at T>700K; $(01\overline{1}0)$ and $(10\overline{1}0)$ facets are observed forming zigzag chains and coexisting with stepped $(11\overline{2}1)$ terraces. Upon further increasing of the initial oxygen exposure, the $(11\overline{2}1)$ terraces are replaced by $(33\overline{6}4)$ facets and eventually $(01\overline{1}0)$ and $(10\overline{1}0)$ facets also appear. For oxygen adsorption at high temperatures (700-1100K), the surface morphology also evolves as the oxygen exposure increases. First, the $(01\overline{1}0)$ and

$(10\bar{1}0)$ facets appear and coexist with $(11\bar{2}1)$; then a (2×1) reconstructed $(11\bar{2}2)$ facet emerges and the surface becomes completely faceted; eventually, the $(11\bar{2}2)$ facet also disappears and the surface is completely covered by four facets: $(01\bar{1}0)$, $(10\bar{1}0)$, $(01\bar{1}1)$ and $(10\bar{1}1)$. All facets disappear when the surface is annealed at T>1300K due to oxygen desorption and the surface reverts to planar. Structure models for the metastable $(33\bar{6}4)$ and $(11\bar{2}2)$ facets are proposed; we find a natural connection between structures of the metastable facets, $(11\bar{2}1)$ and $\{01\bar{1}1\}$ in the sense that each metastable facet contains micro-features that resemble the next facet phase in the morphological evolution sequence.

In Chapter 6 we discuss reconstruction and faceting of Re$(11\bar{2}1)$ induced by adsorption of ammonia. Ammonia dissociates completely into N and H upon adsorption on Re$(11\bar{2}1)$ at 300K. Hydrogen desorbs completely as H_2 by ~600K, the remaining nitrogen atoms on the surface are responsible for the faceting observed upon annealing at 800-900K. Nitrogen also desorbs completely from the surface as N_2 by ~1100K.

Re$(11\bar{2}1)$ becomes partially faceted when it is exposed to ammonia (>0.5L) at 300K followed by annealing at 800-900K. A fully faceted surface can only be obtained upon high exposure to ammonia (>100L) at 800-900K. The facets are $(13\bar{4}2)$ and $(31\bar{4}2)$; their stability may be related to the fact that they are stepped $\{01\bar{1}1\}$ surfaces. A (2×1) reconstruction is observed in LEED when the N-covered Re$(11\bar{2}1)$ surface is annealed at 600-700K. A model involving reconstruction of the substrate is proposed which suggests this reconstruction may be a precursor state for faceting.

For adsorbate-induced faceting of Re($11\bar{2}1$), we also collaborate with theoreticians to better understand the thermodynamical driving force in this process. The

(T, p) phase diagrams generated from DFT calculations confirm that the anisotropy of surface free energy is the driving force for faceting, and the predicted stable phases under various conditions are consistent with the experimental results.

Our work has implications for Re-based catalysts that operate under oxygen or nitrogen-rich conditions because the structure of the catalysts often affects their performance. The results show great promise of tailoring the surface morphology in the nanoscale regime by choosing appropriate adsorbate-substrate combinations, adsorbate coverage and annealing conditions.

The dissertation work also provides guidance on future studies in the following aspects:

1) How does the transition from one faceted structure to another actually happen in real time and real space? Detailed information on this kinetic process can help us understand the microscopic mechanism of mass transport in faceting. Preliminary attempts of using low energy electron microscopy (LEEM) to study the transition are not successful due to its resolution limits. However, with current technological advances, it has become possible to study the transition in real time and real space with a high-temperature, high- speed scanning tunneling microscope (STM).

2) Since the adsorbates studied in the dissertation are all non-metallic, a natural extension is to search for metal-induced faceting of Re surfaces. Metal-induced faceting has been widely observed in previous studies on W(111) and Mo(111); it will be interesting to investigate whether the same phenomenon can occur on Re

surfaces. Preliminary results in our group have shown that gold is a promising candidate to induce faceting of $Re(12\overline{3}1)$.[1]

3) Another extension to the dissertation work is to study adsorbate-induced faceting of other hcp metal surfaces, such as Ru and Co. Such studies may have potential applications in catalysis and magnetic storage since both Ru and Co are important components of industrial catalysts and Co is also a magnetic metal.

4) In section 1.4.2, we have shown successful growth of ordered Co particle arrays using a faceted $Re(12\overline{3}1)$ surface as a template. It is desirable to apply this approach to growth of other materials of great interest.

---

[1] See Robert Baier, master's thesis, Rutgers University, 2008.

Bibliography

A

M. Appl, in *Ullmann's Encyclopedia of Industrial Chemistry*, Wiley-VCH, (2006).

M. Asscher and G. A. Somorjai, Surf. Sci. **143** (1984) L389.

Y. S. Avraamov, A. G. Govozdev and V. M. Kutsak, Phys. Met. Metallogr. **39** (1975) 84.

B

R. Bachelet, S. Cottrino, G. Nahélou, V. Coudert, A. Boulle, B. Soulestin, F. Rossignol, R. Guinebretière and A. Dauger, Nanotechnology **18** (2007) 015301.

A. R. Bachmann, S. Speller, A. Mugarza and J. E. Ortega, Surf. Sci. **526** (2003) L143.

R. Barnes, I. M. Abdelrehim and T. E. Madey, Top. Catal. **14** (2001) 53.

S. Benedetti, P. Torelli, P. Luches, E. Gualtieri, A. Rotaa and S. Valeri, Surf. Sci. **601** (2007) 2636.

F. Besenbacher, I. Chorkendorff, B. S. Clausen, B. Hammer, A. M. Molenbroek, J. K. Norskov and I. Stensgaard, Science **279** (1998) 1913.

G. Binnig, H. Rohrer, C. Gerber and E. Weibel, Appl. Phys. Lett. **40** (1982) 178.

G. Binnig, H. Rohrer, C. Gerber and E. Weibel, Phys. Rev. Lett. **49** (1982) 57.

G. Binnig, H. Rohrer, C. Gerber and E. Weibel, Physica B+C **109/110B** (1982) 2075.

G. Binnig and D. P. E. Smith, Rev. Sci. Instrumen. **57** (1986) 1688.

H. P. Bonzel and M. Nowicki, Phys. Rev. B **70** (2004) 245430.

C

R. A. Campbell, J. Guan and T. E. Madey, Catal. Lett. **27** (1994) 273.

A. S. Y. Chan, W. Chen, H. Wang, J. E. Rowe and T. E. Madey, J. Phys. Chem. B **108** (2004) 14643.

A. S. Y. Chan, G. K. Wertheim, H. Wang, M. D. Ulrich, J. E. Rowe and T. E. Madey, Phys. Rev. B **72** (2005) 035442.

J. G. Che, C. T. Chan, C. H. Kuo and T. C. Leung, Phys. Rev. Lett. **79** (1997) 4230 .

C. J. Chen, Phys. Rev. Lett. **65** (1990) 448.

Q. Chen and N. V. Richardson, Prog. Surf. Sci. **73** (2003) 59.

S. P. Chen, Surf. Sci. **274** (1992) L619.

W. Chen, I. Ermanoski, Q. Wu, T. E. Madey, H. H. Hwu and J. G. Chen, J. Phys. Chem. B **107** (2003) 5231.

W. Chen, I. Ermanoski and T. E. Madey, J. Am. Chem. Soc. **127** (2005) 5014.

W. Chen, I. Ermanoski, T. Jacob and T. E. Madey, Langmuir **22** (2006) 3166.

P. Clark, B. Dhandapani and S. T. Oyama, Appl. Catal. A-Gen. **184** (1999) L175.

G. K. L. Cranstroun and D. R. Pyke, Surf. Sci. **60** (1976) 157.

D

D. B. Danko, M. Kuchowicz and J. Kolacziewicz, Surf. Sci. **552** (2004) 111.

A. K. Datye and D. J. Smith, Catal. Rev. Sci. Eng. **34** (1992) 129.

A. K. Datye, Top. Catal. **13** (2000) 131.

F. R. deBoer, R. Boom, W. C. M. Mattens, A. R. Miedema and A. K. Niessen, *Cohesion in Metals*, North-Holland, Amsterdam, (1988) pp 758.

M.-C. Desjonqueres and D. Spanjaard, *Concepts in surface physics*, Springer-Verlag, Berlin, (1993).

C.-Z. Dong, S. M. Shivaprasad, K. J. Song and T. E. Madey, J. Chem. Phys. **99** (1993) 9172.

M. Drechsler and A. Müller, J. Crystal Growth **3/4** (1968) 518.

R. Ducros and J. Fusy, J. Electron Spectrosc. Relat. Phenom. **42** (1987) 305.

E

C. Egawa, S. Naito and K.Tamaru, Surf. Sci. **125** (1983) 605.

I. Ermanoski, K. Pelhos, W. Chen, J. S. Quinton and T. E. Madey, Surf. Sci. **549** (2004) 1.

I. Ermanoski, *Ph.D. Thesis*, Rutgers University, (2005).

I. Ermanoski, C. Kim, S. Kelty and T. E. Madey, Surf. Sci. **596** (2005) 89.

I. Ermanoski, W. Swiech and T. E. Madey, Surf. Sci. **592** (2005) L299.

F

M. Fanetti, L. Gavioli and M. Sancrotti, Adv. Mater. **18** (2006) 2863.

R. M. Feenstra, J. A. Stroscio, J. Tersoff and A. P. Fein, Phys. Rev. Lett. **58** (1987) 1192.

G

R. Gabai, A. Ismach and E. Joselevich, Adv. Mater. **19** (2007) 1325.

Z. Gai, H. Ji, Y. He, C. Hu, R. G. Zhao and W. S. Yang, Surf. Sci. **338** (1995) L851.

Z. Gai, R. G. Zhao, B. Gao, H. Ji and W. S. Yang, Surf. Sci. **383** (1997) 1.

Z. Gai, W. S. Yang, R. G. Zhao and T. Sakurai, Phys. Rev. B **59** (1999) 15230.

Z. Gai, R. G. Zhao, W. Li, Y. Fujikawa, T. Sakurai and W. S. Yang, Phys. Rev. B **64** (2001) 125201.

M. Gajdardziska-Josifovska, R. Plass, M. A. Schofield, D. R. Giese and R. Sharma, J. Electron Microsc. **51** (2002) S13.

M. J. Gladys, I. Ermanoski, G. Jackson, J. S. Quinton, J. E. Rowe and T. E. Madey, J. Electron Spectrosc. Relat. Phenom. **135** (2004) 105.

Govind, W. Chen, H. Wang and T. E. Madey, in preparation.

D. E. Gray, *American Institute of Physics Handbook (3rd edition)*, 3rd edition ed., McGraw-Hill, (1972).

J. Gustafson, A. Resta, A. Mikkelsen, R. Westerström, J. N. Andersen, E. Lundgren, J. Weissenrieder, M. Schmid, P. Varga, N. Kasper, X. Torrelles, S. Ferrer, F. Mittendorfer and G. Kresse, Phys. Rev. B **74** (2006) 035401.

H

J.-W. He and D. W. Goodman, J. Phys. Chem. **94** (1990) 1502.

J. R. Heffelfinger and C. B. Carter, Surf. Sci. **389** (1997) 188.

C. R. Henry, Surf. Sci. Rep **31** (1998) 231.

C. Herring, Phys. Rev. **82** (1951) 87.

C. Herring, in *Structure and Properties of Solid Surfaces*, ed. R. Gomer and C. S. Smith., University of Chicago Press, Chicago, (1953).

M. A. Van Hove, W. H. Weinberg and C.-M. Chan, *Low-energy electron diffraction: experiment, theory and surface structure determination*, Springer-Verlag, Berlin; New York, (1986).

M. Huth, K. A. Ritley, J. Oster, H. Dosch and H. Adrian, Adv. Funct. Mater. **12** (2002) 333 .

J

N. S. Jacobson, D. J. Myers, D. Zhu and D. L. Humphrey, Oxid. Met. **55** (2001) 471.

S. J. Jenkins and S. J. Pratt, Surf. Sci. Rep. **62** (2007) 373.

K

P. Kaghazchi, T. Jacob, H. Wang, W.Chen and T. E. Madey, in preparation.

P. Kaghazchi and T. Jacob, Phys. Rev. B **76** (2007) 245425.

P. Kaghazchi, I. Ermanoski, W. Chen, T. E. Madey and T. Jacob, ACS Nano **2** (2008) 1280.

D. G. Kelly, J. A. Odriozola and G. A. Somorjai, J. Phys. Chem. **91** (1987) 5695.

R. E. Kirby, C. S. McKee and M. W. Roberts, Surf. Sci. **55** (1976) 725.

R. E. Kirby, C. S. McKee and L. V. Renny, Surf. Sci. **97** (1980) 457.

S. Kiriukhin, L. Sutcu and E. H. Conrad, Phys. Rev. B **59** (1999) 6736.

P. J. Knight, S. M. Driver and D. P. Woodruff, Surf. Sci. **376** (1997) 374.

M. H. Koch, P. Jacob and D. Menzel, Surf. Sci. **367** (1996) 293.

D. Kolthoff, T. Dullweber and H. Pfnur, Surf. Sci. **447** (2000) 259.

M. Kumar, Govind, V. K. Paliwal, A. G. Vedeshwar and S. M. Shivaprasad, Surf. Sci. **600** (2006) 2745.

R. Kumar and H. E. Grenga, Surf. Sci. **50** (1975) 399.

L

J. H. Larsen and I. Chorkendorff, Surf. Sci. Rep. **35** (1999) 163.

S. S. Lee, H. J. Song and J. W. Chung, Surf. Sci. **531** (2003) L357.

K. Liu, S. C. Fung, T. C. Ho and D. S. Rumschitzki, J. Catal. **206** (2002) 188.

E. Loginova, F. Cosandey and T. E. Madey, Surf. Sci. **601** (2007) L11.

E. Loginova, *Ph.D. Thesis*, Rutgers University, (2008).

M

T. E. Madey, Surf. Sci. **33** (1972) 355.

T. E. Madey, J. Guan, C.-Z. Dong and S. M. Shivaprasad, Surf. Sci. **287/288** (1993) 826.

T. E. Madey, J. Guan, C.-H. Nien, C.-Z. Dong, H.-S. Tao and R. A. Campbell, Surf. Rev. Lett. **3** (1996) 1315.

T. E. Madey, C.-H. Nien, K. Pelhos, J. J. Kolodziej, I. M. Abdelrehim and H.-S. Tao, Surf. Sci. **438** (1999) 191.

T. E. Madey, K. Pelhos, Q. Wu, R. Barnes, I. Ermanoski, W. Chen, J. J. Kolodziej and J. E. Rowe, Proc. Natl. Acad. Sci. U.S.A. **99** (2002) 6503.

T. E. Madey, W.Chen, H. Wang, P. Kaghazchi and T. Jacob, Chem. Soc. Rev. **37** (2008) 2310.

F. K. Men, F. Liu, P. J. Wang, C. H. Chen, D. L. Cheng, J. L. Lin and F. J. Himpsel, Phys. Rev. Lett. **88** (2002) 096105.

H. Minoda, K. Yagi, F. Heringdorf, A. Meier, D. Kahler and M. von Hoegen, Phys. Rev. B **59** (1999) 2363.

H. J. Monkhorst and J. D. Pack, Phys. Rev. B **13** (1976) 5188.

C. Morant, L. Galán and J. M. Sanz, Anal. Chim. Acta **297** (1994) 179.

N

H. Niehus, Surf. Sci. **87** (1979) 561.

C.-H. Nien and T. E. Madey, Surf. Sci. **380** (1996) L527.

C.-H. Nien and T. E. Madey, Surf. Sci. **380** (1997) L527.

C.-H. Nien, *Ph. D. Thesis*, Rutgers University, (1999).

C.-H. Nien and T. E. Madey, Surf. Sci. **433-435** (1999) 254.

O

K. Ohmori, Y. L. Foo, S. Hong, J. G. Wen, J. E. Greene and I. Petrov, Nano Lett. **5** (2005) 369.

T. Ohno, K. Sarukawa and M. Matsumura, New J. Chem. **26** (2002) 1167.

C. Oleksy, Surf. Sci. **549** (2004) 246.

S. H. Overbury, P. A. Bertrand and G. A. Somorjai, Chem. Rev. **75** (1975) 547.

P

R. Pantel and M. Bujor, Surf. Sci. **83** (1979) 228.

K. Pelhos, J. B. Hannon, G. L. Kellogg and T. E. Madey, Surf. Sci. **432** (1999) 115.

J. P. Perdew, K. Burke and M. Ernzerhof, Phys. Rev. Lett. **77** (1996) 3865.

R. Plass, J. Feller and M. Gajdardziska-Josifovska, Surf. Sci. **414** (1998) 26.

F. Pourmir, S. Rousset, S. Gauthier, M. Sotto, J. Klein, J. Lecoeur and J. P. Bellier, Surf. Sci. **324** (1995) L337.

R

M. Ramamoorthy, D. Vanderbilt and R. D. King-Smith, Phys. Rev. B **49** (1994) 16721.

P. A. Redhead, Vacuum **12** (1962) 203.

N. Reinecke and E. Taglauer, Surf. Sci. **454-456** (2000) 94.

S. Reiter and E. Taglauer, Surf. Sci. **367** (1996) 33.

K. Reuter and M. Scheffler, Phys. Rev. B **65** (2001) 35406.

C. Revenant, F. Leroy, G. Renaud, R. Lazzari, A. Létoublon and T. Madey, Surf. Sci. **601** (2007) 3431.

M. Reyhan, H. Wang and T. E. Madey, Catal. Lett. in press.

S

M. Sander, R. Imbihl, R. Schuster, J. V. Barth and G. Ertl, Surf. Sci. **271** (1992) 159.

M. P. Seah and W. A. Dench, Surf. and Interface Anal. **1** (1979) 2.

L. Seehofer, S. Huhs, G. Falkenberg and R. L. Johnson, Surf. Sci. **329** (1995) 157.

M. D. Segall, P. L. D. Lindan, M. J. Probert, C. J. Pickard, P. J. Hasnip, S. J. Clark and M. C. Payne, J. Phys.: Condens. Matter **14** (2002) 2717.

F. Solymosi, P. Tolmacsov and T. S. Zakar, J. Catal. **233** (2005) 51.

G. A. Somorjai, *Introduction to Surface Chemistry and Catalysis*, Wiley, New York, (1994).

G. A. Somorjai and Y. G. Borodko, Catal. Lett. **76** (2001) 1.

K.-J. Song, J. C. Lin, M. Y. Lai and Y. L. Wang, Surf. Sci. **327** (1995) 17.

K.-J. Song, W.-R. Chen, V. Yeh, Y.-W. Liao, P. T. Tsao and M.-T. Lin, Surf. Sci. **478** (2001) 145.

M. J. S. Spence, A. Hung, I. K. Snook and I. Yarovsky, Surf. Sci. **513** (2002) 389.

N. D. Spencer and G. A. Somorjai, J. Phys. Chem. **86** (1982) 3493.

D. R. Strongin and G. A. Somorjai, J. Catal. **118** (1989) 99.

D. R. Stull and H. Prophet, *JANAF thermochemical tables*, 2nd ed., U.S National Bureau of Standards, Washington, DC, (1971).

R. Stumpf, Phys. Rev. Lett. **78** (1997) 4454.

A. Szczepkowicz, A. Ciszewski, R. Bryl, C. Oleksy, C. H. Nien, Q. Wu and T. E. Madey, Surf. Sci. **599** (2005) 55.

R. Szukiewicz and J. Kolaczkiewicz, Surf. Sci. **547** (2003) L837.

T. Suzuki, Y. Temko, M.C. Xu and K. Jacobi, Surf. Sci. **573** (2004) 457.

T

E. Taglauer, S. Reiter, A. Liegl and S. Schömann, Nucl. Instr. Meth. B **118** (1996) 456.

N. J. Taylor, Surf. Sci. **2** (1964) 544.

J. Tersoff and D. R. Hamann, Phys. Rev. Lett. **50** (1983) 1998.

J. Tersoff and D. R. Hamann, Phys. Rev. B **31** (1985) 805.

P. Thiry, P. A. Bennett, S. D. Kevan, W. A. Royer, E. E. Chaban, J. E. Rowe and N. V. Smith, Nucl. Instrum. Methods Phys. Res. Sect. A **222** (1984) 85.

J. C. Tracy and J. M. Blakely, Surf. Sci. **13** (1969) 313.

C. W. Tucker, Acta Metal. **15** (1967) 1465.

W. T. Tysoe, F. Zaera and G. A. Somorjai, Surf. Sci. **200** (1988) 1.

W. R. Tyson and W. A. Miller, Surf. Sci. **62** (1977) 267.

V

D. Vanderbilt, Phys. Rev. B **41** (1990) 7892.

L. Vitos, A. V. Ruban, H. L. Skriver and J. Kollar, Surf. Sci. **411** (1998) 186 and reference therein.

S. Vollmer, A. Birkner, S. Lucas, G. Witte and C. Wöll, Appl. Phys. Lett. **76** (2000) 2686.

W

D. A. Walko and I. K. Robinson, Phys. Rev. B **64** (2001) 045412.

H. Wang, W. Chen and T. E. Madey, Phys. Rev. B **74** (2006) 205426.

H. Wang, A. S. Y. Chan, W. Chen, P. Kaghazchi, T. Jacob and T. E. Madey, ACS Nano **1** (2007) 449.

L. S. Wang, R. Ohnishi and M. Ichikawa, J. Catal. **190** (2000) 276.

A. T. S. Wee, J. S. Foord, R. G. Egdell and J. B. Pethica, Phys. Rev. B **58** (1998) R7548.

S. Weichel and P. J. Moller, Surf. Sci. **399** (1998) 219.

R. Westerström, J. Gustafson, A. Resta, A. Mikkelsen, J. N. Andersen, E. Lundgren, N. Seriani, F. Mittendorfer, M. Schmid, J. Klikovits, P. Varga, M. D. Ackermann, J. W. M. Frenken, N. Kasper and A. Stierle, Phys. Rev. B **76** (2007) 155410.

R. Wiesendanger and H.-J. Güntherodt, *Scanning Tunneling Microscopy I: General Principles and Applications to Clean and Adsorbate-Covered Surfaces*, 2nd ed., Springer-Verlag, Berlin; New York, (1994).

R. Wiesendanger and H.-J. Güntherodt, *Scanning Tunneling Microscopy II : Further Applications and Related Scanning Techniques*, 2nd ed., Springer-Verlag, Berlin; New York, (1995).

R. Wiesendanger and H.-J. Güntherodt, *Scanning Tunneling Microscopy III: Theory of STM and Related Scanning Probe Methods*, Springer-Verlag, Berlin; New York, (1997).

E. D. Williams and N. C. Bartelt, Ultramicroscopy (1989).

E. D. Williams and N. C. Bartelt, Science **251** (1991) 393.

G. A. Wolff and J. G. Gualtieri, Am. Mineral. **47** (1962) 562.

D. P. Woodruff and T. A. Delchar, *Modern Techniques of Surface Science*, 2nd ed., Cambridge University Press, Cambridge, (1994).

Y

K. Yagi, H. Minoda and M. Degawa, Surf. Sci. Rep **43** (2001) 45.

D. Yu and M. Scheffler, Phys. Rev. B **70** (2004) 155417.

Y. Yuan, H. Liu, H. Imoto, T. Shido and Y. Iwasawa, J. Catal. **195** (2000) 51.

Z

F. Zaera and G. A. Somorjai, Surf. Sci. **154** (1985) 303.

D. M. Zehner and H. E. Farnsworth, Surf. Sci. **30** (1971) 335.

C. Zhang, M. A. vanHove and G. A. Somorjai, Surf. Sci. **149** (1985) 326.

X. Y. Zhao, H. Wang, R. G. Zhao and W. S. Yang, Mat. Sci. Eng. C-Bio. S. **16** (2001) 41.

F. Zu Heringdorf, D. Kahler, M. Horn-Von Hoegen, T. Schmidt, E. Bauer, M. Copel and H. Minoda, Surf. Rev. Lett.

Curriculum Vitae

HAO WANG

EDUCATION:

2008   Ph. D. in physics, Rutgers University - New Brunswick
2000   M.S. in physics, Peking University, China
1997   B.S. in physics, Peking University, China

PUBLICATIONS:

1. T. E. Madey, W. H. Chen, H. Wang, P. Kaghazchi and T. Jacob, "Nanoscale surface chemistry over faceted substrates: structure, reactivity and nanotemplates", *Chem. Soc. Rev.*, **37**, 2310 (2008).
2. M. Reyhan, H. Wang and T. E. Madey, "Preferential nucleation of metallic clusters on a nanotemplate: Co on oxygen-faceted $Re(12\bar{3}1)$", *Catal. Lett.*, in press.
3. H. Wang, A. S. Y. Chan, W. H. Chen, P. Kaghazchi, T. Jacob and T. E. Madey, "Facet stability in oxygen-induced faceting of $Re(12\bar{3}1)$", *ACS Nano* **1**, 449-455 (2007).
4. H. Wang, W. H. Chen and T. E. Madey, "Morphological evolution in oxygen-induced faceting of $Re(12\bar{3}1)$", *Phys. Rev. B* **74**, 205426:1-11 (2006).
5. A. S. Y. Chan, G. K. Wertheim, H. Wang, M. D. Ulrich, J. E. Rowe and T. E. Madey, "Surface atom core-level shifts of clean and oxygen-covered $Re(12\bar{3}1)$", *Phys. Rev. B* **72**, 035442 (2005).
6. A. S. Y. Chan, W. H. Chen, H. Wang, J. E. Rowe and T. E. Madey, "Methanol reactions over oxygen-modified re surfaces: Influence of surface structure and oxidation ", *J. Phys. Chem. B* **108**,14643 (2004).
7. X. Y. Zhao, H. Wang, R. G. Zhao and W. S. Yang, "Self-assembly of amino acids on the Cu(001) surface", *Mat. Sci. Eng. C-Bio.* S **16**, 41 (2001).
8. X. Y. Zhao, H. Wang, H. Yan, Z. Gai, R. G. Zhao and W. S. Yang, "Adsorption behavior of amino acids on copper surfaces", *Chinese Phys.* **10**, S84-S95 (2001).
9. H. Wang, X. Y. Zhao, R. G. Zhao and W. S. Yang, "Adsorption of L-phenylalanine on Cu(001)", *Chinese Phys. Lett*. 18, 45 (2001).
10. H. Wang, X. Y. Zhao and W. S. Yang, "Adsorption of aspartic acid on Cu(001) studied by scanning tunneling microscopy ", *Acta Phys. Sin.* **49**, 1316 (2000) (in Chinese).